IMT School for Advanced Studies, Lucca

Lucca, Italy

Applications of Network Science in Neuroimaging

PhD Program in Cognitive, Computational and Social Neurosciences

XXXIII Cycle

By

Adrian I. Onicas

2022

The dissertation of Adrian I. Onicas is approved.

PhD Program Coordinator: Prof. Pietro Pietrini, IMT School for Advanced Studies Lucca

Advisor: Prof. Emiliano Ricciardi, IMT School for Advanced Studies Lucca

Co-Advisor: Dr. Luca Cecchetti, IMT School for Advanced Studies Lucca

Co-Advisor: Dr. Tommaso Gili, IMT School for Advanced Studies Lucca

Visiting Traineeship Advisor: Prof. Keith Yeates, University of Calgary

The dissertation of Adrian I. Onicas has been reviewed by:

Dr. Uri Hasson, University of Trento

Dr. Emily L. Dennis, University of Utah

IMT School for Advanced Studies Lucca

2022

Contents

List of Figures

List of Tables

Acknowledgements

In addition to the outstanding support from my advisor and co-advisors, I would like to address special thanks to people that have supported me in this work:

- Dr. Ashley Ware, Georgia State University, USA
- Dr. Stephanie Deighton, University of Calgary, Canada
- Dr. Catherine Label, University of Calgary, Canada
- Dr. Ashley Harris, University of Calgary, Canada
- Dr. Signe Bray, University of Calgary, Canada
- Dr. Rossana Mastrandrea, IMT School for Advanced Studies Lucca, Italy.

Disclaimer:

The work in Chapter 2 has been previously published:

- **Onicas, A. I.**, Ware, A. L., Harris, A. D., Beauchamp, M. H., Beaulieu, C., Craig, W., ... & Lebel, C. (2022). Multisite Harmonization of Structural DTI Networks in Children: An A-CAP Study. *Frontiers in neurology*, 13.

In addition, Chapter 2 and Chapter 3 contain partial methodological information that was previously described:

- Ware, A. L., Yeates, K. O., Tang, K., Shukla, A., **Onicas, A. I.,** Guo, S., ... & Lebel, C. (2022). Longitudinal white matter microstructural changes in pediatric mild traumatic brain injury: An A-CAP study. *Human Brain Mapping*.

Vita

2015 BA Degree in Psychology
Final mark: 10/10
Babes-Bolyai University, Cluj-Napoca, Romania

2017 MSc Degree in Clinical Psychology
Final mark: 10/10
Babes-Bolyai University, Cluj-Napoca, Romania

2020 Visiting Student
University of Calgary, Calgary, Canada

Publications

1. Onicas, A. I., Ware, A. L., Harris, A. D., Beauchamp, M. H., Beaulieu, C., Craig, W., ... & Lebel, C. (2022). Multisite Harmonization of Structural DTI Networks in Children: An A-CAP Study. *Frontiers in neurology*, 13.
2. Ware, A. L., Yeates, K. O., Tang, K., Shukla, A., Onicas, A. I., Guo, S., ... & Lebel, C. (2022). Longitudinal white matter microstructural changes in pediatric mild traumatic brain injury: An A-CAP study. *Human Brain Mapping*.
3. Ware, A. L., Shukla, A., Guo, S., Onicas, A., Geeraert, B. L., Goodyear, B. G., ... & Lebel, C. (2022). Participant factors that contribute to magnetic resonance imaging motion artifacts in children with mild traumatic brain injury or orthopedic injury. *Brain Imaging and Behavior*, 16(3), 991-1002.
4. Botvinik-Nezer, R., Holzmeister, F., Camerer, C. F., Dreber, A., Huber, J., Johannesson, M., ..., Onicas, A.,... & Rieck, J. R. (2020). Variability in the analysis of a single neuroimaging dataset by many teams. *Nature*, 582(7810), 84-88.

Manuscripts under review

1. Ware, A. L., Onicas, A., Abdeen, N., Beauchamp, M., Beaulieu, C., ..., Yeates, K. O. & Lebel, C. (2022). Altered Longitudinal Structural Connectome in Pediatric Mild Traumatic Brain Injury: An A-CAP Study.
2. Ware, A. L., Lebel, C., Onicas, A., Abdeen, N., Beauchamp, M., ..., & Yeates, K. O. (2022). Longitudinal Gray Matter Trajectories in Pediatric Mild Traumatic Brain Injury: An A-CAP Study.

Presentations

1. Onicas, A. (2020, September 18). From time series to networks in event-related fMRI [Conference presentation]. Network Neuroscience Satellite, Network Science Society Conference (NetSci2020), Rome, Italy.
2. Onicas, A., Gili, T., Cecchetti L., & Ricciardi, E. (2020, June 23 – July 3). Detecting task events in fMRI time series based on Visibility Graphs [Poster presentation]. 26th Annual Meeting of the Organization for Human Brain Mapping (OHBM2020), Montreal, Canada.
3. Onicas, A. (2019, March 15). fMRI time series analysis using Visibility Graphs [Workshop presentation]. New Trends in Statistical Physics, Lucca, Italy.

Preprints

1. Billings, J. C. W., Hu, M., Lerda, G., Medvedev, A. N., Mottes, F., Onicas, A., ... & Petri, G. (2019). Simplex2vec embeddings for community detection in simplicial complexes. *arXiv preprint arXiv:1906.09068*.

Abstract

At the intersection between neuroimaging and network science, network neuroscience has brought remarkable opportunities to advance the understanding of the human brain. At macroscale, the brain can be seen as a complex system relying on communication between its regions. Advanced neuroimaging techniques can map functional and structural brain communication, enabling the study of network-level alterations in neurological disorders during development. To improve reproducibility and provide a robust characterization of neurological disorders, collaborative initiatives involving neuroimaging data collection across multiple sites have started to emerge. However, multisite data acquisition poses significant challenges for managing increasingly larger and more complex datasets, especially for data analysis pipelines required for whole-brain network analysis. To this end, the current work aims to (1) assess different data harmonization techniques and (2) characterize structural and functional network alterations in mild traumatic brain injury. In addition to the typical applications for whole-brain network analysis, network science can be utilized for advanced time series analysis and address challenges for signal processing in functional neuroimaging. Visibility graphs can map time series into networks where nodes represent time points, and have rapidly found applications across areas of science, including resting state functional neuroimaging. However, to validate their use, the current work aims to test if task activity can be identified based on the local network centrality (node degree) in synthetically generated data and event-related task fMRI time series.

The Advancing Concussion in Pediatrics (A-CAP) study is the largest study of mild traumatic brain injury to date, and was used to address

the first two aims of this work. To understand network-level alterations following mild traumatic brain injury in the pediatric population, the current work validates the use of ComBat harmonization for network analysis pipelines and tests for longitudinal alterations in network topology. ComBat harmonization had improved performance in removing site effects when applied on network parameters instead of edge-wise connectivity weights, and demonstrated excellent within-site consistency with the network parameters before harmonization for structural and functional networks. Network parameters based on structural and functional connectivity show no effects of injury before or after harmonization in the post-acute phase following mild TBI. However, further longitudinal analysis of global and nodal abnormalities in the functional connectome indicates that variability in time post-injury, post-concussive symptoms, biological sex, and age moderate the effect of injury in local and global functional network topology.

To address the third aim of the current work, two datasets were used. First, synthetic data was generated to resemble well-controlled event-related task fMRI signals, by adding varying levels of noise. An accuracy score was defined to compare the identifiability of task events based on visibility graph transformation versus the raw fMRI time series across noise levels. The results were replicated using a slow, event-related picture presentation dataset, with extensive scanning of four participants. When applied to time series analysis, visibility graphs can accurately identify task events and are robust to gaussian noise in synthetic time series and to participant motion in real task fMRI data. The current work addresses substantial contributions in mapping the human brain using neuroimaging and network science.

Chapter 1

Introduction

The development of functional magnetic resonance imaging (fMRI) in the early 1990s has generated abundant research, with applications for cognitive and clinical neuroscience (Glover, 2011). Neuroimaging, however, was not the only field to undergo outstanding developments during the '90s. The understanding of the physics of complex systems and network science has undergone extensive developments almost in parallel (Vespignani, 2018; Louridas, 2018; Iñiguez, Battiston, and Karsai, 2020; Bullmore and Sporns, 2009). At the intersection between neuroimaging and complex systems, network neuroscience has recently emerged as a tool for quantifying brain communication across different scales (Bassett and Sporns, 2017).

At macroscale, network neuroscience is most often used to map and describe the brain in terms of interactions between regions (Bullmore and Sporns, 2009). In this perspective, each brain region can be seen as a node, and the relationship between brain regions is represented as links (edges). Network science-based tools can, however, map virtually any system into a mathematical form, that is the adjacency matrix. This flexibility provides other possible applications for neuroimaging. More recently developed algorithms can transform temporal sequences in networks.

These techniques are promising for functional neuroimaging because they can achieve more flexible ways of analyzing brain data, allowing researchers to extract complex features derived from signal changes across time.

The work addresses applications of network science in neuroimaging with significant clinical and methodological implications, including managing network analyses for multi-site data collection, approaching how functional brain networks and their interaction with structural connectome can be impacted by traumatic brain injuries in children, and testing new applications of temporal networks in functional neuroimaging time-series analysis based on visibility graphs.

1.1 Brain networks based on structural and functional neuroimaging

One of the most interesting topics in cognitive neuroscience addresses the question of whether mental operations rely on the localized activity at the level of brain regions, or are represented as distributed, network-level phenomena (McIntosh, 2000). Functional localization emphasizes that areas of the brain act as highly segregated modules responsible for specific functions. Until relatively recently, most of the fMRI literature has focused on localizing brain activity when participants perform certain operations during a scanning session. An ingredient contributing to the development of network neuroscience is the hypothesis that the physiological basis for information processing and mental representations relies on dynamic interactions between segregated brain regions (Bressler, 1995; McIntosh, 2000; Friston, 2002).

Using non-invasive neuroimaging techniques, connections among brain regions can be mapped at both, structural and functional levels. Mapping white matter connectivity between brain regions using diffusion magnetic resonance imaging (DTI) and whole-brain tractography is a common technique to characterize macroscale structural communica-

tion non-invasively (Sporns, Tononi, and Kötter, 2005; Bullmore and Sporns, 2009; C. Stam, 2014). Networks constructed with DTI have a direct anatomical interpretation because they emphasize properties of white matter bundles connecting voxels corresponding to different brain areas (Gong, He, Concha, Lebel, Donald W. Gross, et al., 2009b). For example, fractional anisotropy (FA) assesses the degree to which water molecules can diffuse within a voxel (Alexander et al., 2007). When water diffusion occurs along one axis, FA values are higher, indicative of denser axonal packing, larger axonal diameter, or high myelination. Free water diffusion in all directions reflects lower FA values, which may be interpreted in terms of axonal degeneration and demyelination (Alexander et al., 2007). Using a brain parcellation, FA values can represent weights connecting pairs of brain regions (see **Figure 1.1**).

At the functional level, the interaction between brain regions can be measured using resting-state fMRI. This technique was widely adopted in the study of the functional connectome, providing simple means for data collection, because it does not require the performance of a specific task by study participants. At rest, fMRI is thought to capture intrinsic brain activity originating in spontaneous BOLD oscillation at different locations in the brain (Stephen M. Smith et al., 2013). The mapping of functional connectivity using this approach relies on establishing statistical dependencies between localized time series originating in BOLD signal changes (Avena-Koenigsberger, Misic, and Sporns, 2018). Specifically, functional networks can be constructed following the extraction of average time courses from regions across the brain using a parcellation (see **Figure 1.1, A**). An edge is defined for each pair of brain regions, by calculating the similarity between the time series, usually by means of Pearson correlation, reflecting connectivity strength. In functional connectivity matrices, higher values are indicative of enhanced synchrony among pairs of regions. In a typical network analysis workflow, structural and functional connectivity matrices are constructed at the participant level (**Figure 1.1, B**).

After obtaining connectivity weights, a threshold is typically applied in

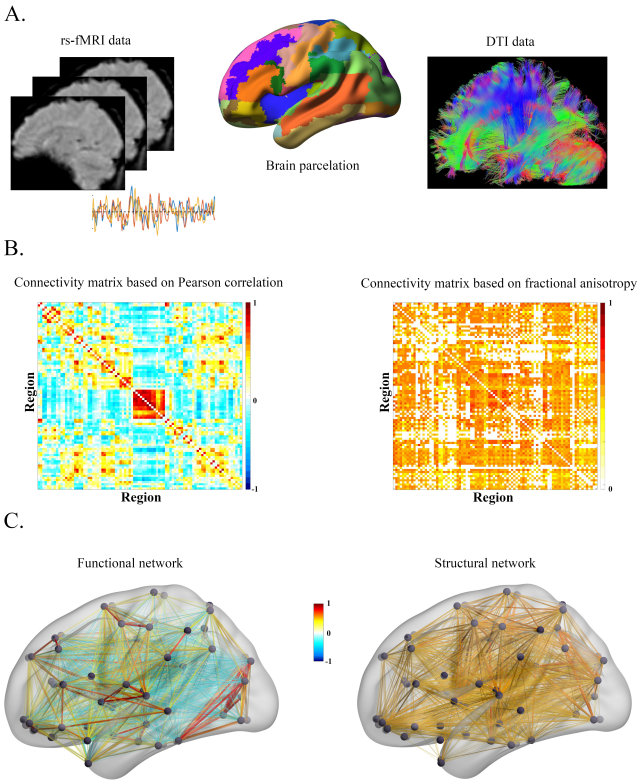

Figure 1.1: Overview of functional and structural connectivity matrix construction. **A.** A parcellation (middle) can be used to define regions of interest for both, rs-fMRI (left) and tractography data (right). **B**. In both cases, connectivity weights are mapped into a region-by-region matrix. In this case, both matrices are symmetric and weighted. For functional data, Pearson correlation between pairs of regions is commonly used for the definition of connectivity weights, which implies the existence of negative connections (left). **C.** A visualization of the connectivity matrices corresponding to the functional (Pearson correlation values – left) and the structural (fractional anisotropy values – right) connectomes for the same participant.

order to remove the weakest connections. Following the application of a threshold to the connectivity matrices, either a weighted (as depicted

in **Figure 1.1, B**) or binary adjacency matrix can be constructed. Matrix thresholding has generated significant controversy in the literature because the choice of an appropriate threshold can influence the topology of the participant-level networks. A threshold is commonly defined using either an absolute or a proportional value. Although there is no standard for the decision of a specific value for absolute or proportional thresholding, an aspect that is often ignored in the literature is the preservation of fully-connected networks (Bordier, Nicolini, and Bifone, 2017; Nicolini et al., 2020). In fully connected networks, nodes are linked in a manner that prevents the breakage of the network into components. Components arise when one or more nodes are separated by the main network (see **Figure 1.2**). Different thresholding techniques may be appropriate for different neuroimaging modalities. Unlike DTI-based connectivity matrices where links reflect direct anatomical connections between regions of the brain, functional brain networks based on fMRI are usually constructed by calculating statistical dependencies between time series, which provides a more indirect method to characterize brain communication. It has been proposed that proportional thresholds may provide more appropriate control for overall differences in network density (i.e. the ratio between existing connections to the total number of possible connections; Achard and Ed Bullmore, 2007;Wijk, C. J. Stam, and Daffertshofer, 2010). Differences in network density can lead to spurious between-group effects because other metrics, such as efficiency and clustering coefficient, can be influenced by overall network density (Achard and Ed Bullmore, 2007; Wijk, C. J. Stam, and Daffertshofer, 2010).

1.2 Common properties of structural and functional brain networks

Once neuroimaging data is mapped into an adjacency matrix, network science tools can summarize the architecture of complex interactions between brain regions. Graph theory describes how the information flows across a network and its applicability to neuroimaging data brings an

elegant way of condensing the considerable amount of data by quantifying brain architecture into meaningful numbers. When using graph theory, it is common to describe the topological brain architecture based on the segregation-integration dichotomy, which can be approached at a systemic (global or whole-brain) or local level (e.g., at the level of brain regions). Measures of integration rely on the idea that optimal information flow takes place via shorter path lengths (see **Figure 1.2**). For instance, information would need to travel through a lower number of regions (thus shorter path length) to arrive from the source to its destination (Ed Bullmore and Sporns, 2012; Rubinov et al., 2015). Global efficiency is calculated as the inverse of the path length that is required, on average, to transmit information between brain regions (Latora and Marchiori, 2001).

Brain *segregation* emphasizes the concept that denser information communication takes place between subsets of nodes, also named cliques (for a smaller number of regions) or modules (for a bigger number of regions). *clustering coefficient* (Watts and Strogatz, 1998) quantifies the number of triangles (or closed connections) that surround each node. These can be considered cliques rather than modules because the presence of a "triangle" implies the existence of mutual connections across only three nodes. At the global level, the clustering coefficient can be calculated as the average across all nodes of the network. Thus, a higher global clustering coefficient suggests higher local segregation in a network.

The tendency of nodes to form connections in small groups (i.e., cliques) does not necessarily imply a separation of the network into bigger groups of nodes, or modules. In addition to the clustering coefficient, *modularity* is typically used to capture the natural segregation of a network (Fornito, Zalesky, and Edward Bullmore, 2016, p. 271) and can be measured by partitioning a network into non-overlapping modules (Newman, 2004), although optimization algorithms for overlapping modules exist (e.g. (Palla et al., 2005). *Small world topology* reflects the balance between integration and segregation, characterizing networks with high clustering but short path length, allowing inter-modular information transmission to take place despite higher segregation.

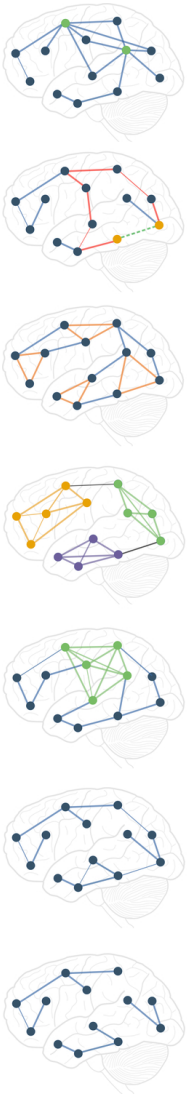

Figure 1.2: A summary of common network properties.

The way information travels into the brain can also be influenced by external damage. Under perturbation, networks can be affected to different

extents depending on their configuration. A robust topology implies that a network is more resilient to perturbation, such as the random removal of some of its links. Brain networks are thought to be organized in a way that protects them from injury, and this organization might be particularly relevant in TBI. *Core-periphery organization* (Borgatti and Everett, 2000; Rombach et al., 2014) has been proposed as a property of complex networks to support the integration of information. Core-periphery organization describes a system in terms of two groups of nodes: a core, which is composed of highly connected nodes that occupy a topologically central position in the network, and a periphery, formed by nodes that are weakly connected with each other and moderately connected to the core (Fornito, Zalesky, and Edward Bullmore, 2016, p. 179). This type of organization is thought to reflect the robustness of the network by increasing the resilience to random node failures (Peixoto and Bornholdt, 2012), and emerges in networks that are susceptible to resource limitations (that is, networks with scarce resources and where forming connections is costly (Csermely et al., 2013; Fornito, Zalesky, and Edward Bullmore, 2016).

1.3 Network analysis of mild Traumatic Brain Injury using multisite neuroimaging

A promising application of network neuroscience is the characterization of brain mechanisms involved in impairments of neurological function. Traumatic Brain Injury (TBI) affects 30–40 million people each year worldwide (Maas et al., 2017a), with about half of the population sustaining a TBI during their lifetime in the United States (Whiteneck et al., 2016). TBI occurs when a sudden external force causes damage to the brain and can result in significant functional impairment, including loss of consciousness and posttraumatic amnesia (David K. Menon et al., 2010). Up to 90% of the cases of TBI are mild in severity (i,e., concussion; Thurman,2016; Babl et al., 2017), with no or only a brief loss of consciousness (less than 30 minutes), posttraumatic amnesia for less than 24 hours, and Glasgow Coma Scale score between 13 and 15.

Mild TBI could potentially cause brain network-level perturbations because psychical head injuries can result in alterations of white-matter bundles across the brain (Blennow et al., 2016; Langlois, Rutland-Brown, and Wald, 2006). This effect can be visible using conventional structural imaging across severe forms of TBI, however, cases with mild severity are typically not associated with visible structural damage (Shin et al., 2017; Palacios et al., 2017). Structural alteration can however be statistically identified based on advanced neuroimaging across mild TBI. In a recent report, we showed that some alterations occur across white matter tracks, although they are moderated by other variables, including time post-injury, age, gender, or the presence of persistent symptoms (Ashley L Ware, Keith Owen Yeates, et al., 2022). The problem of considering potential significant moderators to account for the heterogeneity of mild injuries has been raised, but the study of moderating variables requires higher statistical power, therefore this issue is typically not properly addressed in the current literature. This potentially results in mixed findings across studies. For example, reports testing for an overall effect of injury across adults with mild TBI showed mixed results for functional connectome abnormalities in terms of connectivity strength (Morelli et al., 2021) and global network topology (Kim et al., 2022; Yan et al., 2017; Horn et al., 2017; Yan et al., 2017; Caeyenberghs et al., 2017; Churchill et al., 2021; Pandit et al., 2013; Y. Zhou, 2017), highlighting that mild TBI might demonstrate significant heterogeneity across age groups and imaging modalities.

The diversity and heterogeneity of pathophysiological mechanisms underlying mild TBI pose significant challenges to its study using neuroimaging. On one hand, methodological differences in study design can have a significant influence on the conclusions drawn from mild TBI neuroimaging research, for example, the choice of an appropriate comparison group (Ware, Shukla, et al., 2022; Ware, Yeates, et al., 2021; Wilde et al., 2019). A recent study has demonstrated that structural connectome across mild TBI children does not show an overall difference in the post-acute phase when compared with children that suffered orthopedic injuries, however, both mild TBI and orthopedic injury groups differ in global topology

relative to typical development (Ware, Yeates, et al., 2021). Whereas most of the TBI literature uses a comparison group comprising individuals unaffected by any type of injury (Imms et al., 2019), children with orthopedic injuries may be more similar in terms of motion artifact, which is a major factor to take into consideration in neuroimaging studies. In a previous analysis (Ware, Shukla, et al., 2022), we showed that the amount of DTI volumes demonstrating gross motion artifact differs between typically developing children and those that had either mild TBI or OI (see **Figure 1.3**). Procedures for data curation to prevent the impact of motion artifacts exist (Power, Mitra, et al., 2014), but systematic between-group differences due to motion artifacts can be more challenging to account for (Dziemian, Barańczuk-Turska, and Langer, 2022). Taken together, the results mentioned above suggest that orthopedic injury may represent a more conservative comparison group for mild TBI, but it may provide appropriate control systematic group differences in motion artifact.

The prognostic utility of neuroimaging in pediatric mild TBI is limited by the scarcity of studies with appropriate statistical power required to capture mild TBI heterogeneity and retain the risk of statistical errors under control. However, the high cost of neuroimaging data acquisition (Mumford and Thomas E. Nichols, 2008) can substantially constrain the ability of a single research center to collect large amounts of scans. Researchers increasingly address the issue of poor reproducibility following the recruitment of small samples in the published literature (Button et al., 2013; Turner et al., 2018; Grady et al., 2021). In addition, the research questions addressed in the field oftentimes relate to small effect sizes and may require larger samples for reliable inference (Stephen M Smith and Thomas E Nichols, 2018; Noble, Scheinost, and Constable, 2020). Collaborative approaches can address this problem by collectively acquiring neuroimaging data using similar study protocols across multiple centers. In pediatric mild TBI, the Advancing Concussion Assessment in Pediatrics study (A-CAP; Keith Owen Yeates et al.; 2017) is the largest dataset currently available, which recruited longitudinal multimodal neuroimaging data at 5 hospitals across Canada.

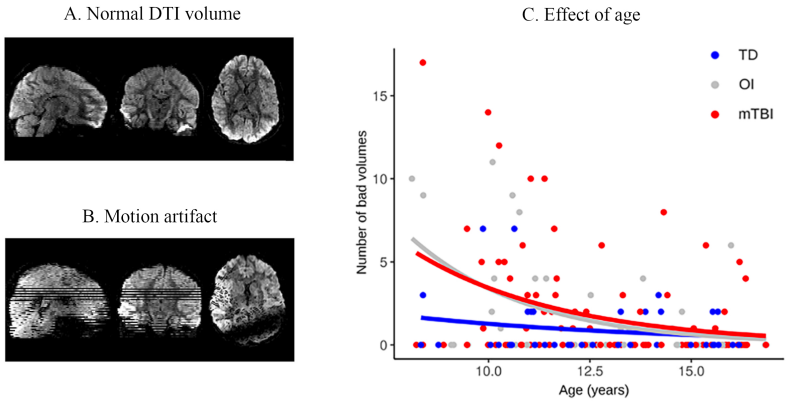

Figure 1.3: Differences in motion between typical development, orthopedic injury, and mild TBI children based on DTI scans. Compared to a normal DTI volume (A), motion artifact produces visible image distortions (B) on DTI images. Children with post-acute orthopedic injury (OI) and mild traumatic brain injury (TBI) show a stronger relationship between age and motion artifact compared to typically developing children (TD) based on the number of DTI volumes with visible motion artifact (Ware, Shukla, et al., 2022)

With the increased availability of multisite neuroimaging datasets, a topic that started to gain significant attention in the neuroscience community is multisite harmonization (Pinto et al., 2020; Fortin, Parker, et al., 2017; Fortin, Cullen, et al., 2018; Pomponio et al., 2020; Adrian I. Onicas et al., 2022). Significant progress has been made with respect to analyzing data using multiple scanners, but the current literature lacks a comprehensive evaluation of multisite harmonization in the context of network analyses. The need for such an evaluation is motivated by the data analysis pipeline required for a graph-theory study. In a typical connectome study, multi-site harmonization is performed at the level of the connectivity weights (Kurokawa et al., 2021; Yu, Linn, et al., 2018), which represent pairwise connection strength among brain regions (e.g., average fractional anisotropy for structural or Pearson correlation between pairs of brain regions for functional connectivity). The harmonized connectivity values

can then be used for the group-level analysis. However, graph theory analysis takes place after connections have been mapped in a network. This implies at least two possibilities for data harmonization: similar to a typical connectivity study, data harmonization can be performed prior to the calculation of network parameters (i.e., matrix harmonization, at the level of connectivity weights) or after network parameters are calculated (i.e., parameter harmonization).

Currently, no study has assessed whether one method performs better than the other. A typical connectivity study may perform univariate group analysis, by applying a statistical test over connectivity weights from a set of brain regions (or average weights across multiple pairs of regions). However, the algorithmic operations for calculating global network parameters take as input all the connection weights simultaneously. Unlike univariate statistics based on individual connection weights, global network parameters measure interactions across regions across the whole brain, generating new features for the group-level statistical model. Data harmonization performed at the level of connection weights does not guarantee the reduction of site effects across the network as a whole. It is unclear how multisite harmonization affects the distribution of the final data. Specifically, global network parameters are computed based on participant-level adjacency matrices and data harmonization involves the application of a group-level statistical model that includes site as a covariate. Participant-level matrices could contain new variability that is unrelated to the original topology, which may influence the accurate estimation of network parameters.

An efficient multisite harmonization method may reduce site effects but preserve the within-site (original) variability. Currently, assessments of multisite harmonization techniques rely on testing the efficiency of removing site effects without careful consideration of how within-site variability changes (Pinto et al., 2020; Fortin, Parker, et al., 2017; Fortin, Cullen, et al., 2018; Pomponio et al., 2020). In addition, the validity of the data is justified by quantifying the relationship between age and neuroimaging data before and after harmonization. However, a significant or higher age

correlation does not necessarily imply an improvement in data accuracy, especially in the absence of ground truth (such as a large single-site study for a reference value). Significant age correlation can exist in the absence of accurate data preparation. For example, motion artifact is a well-known source of bias that can increase age correlations across neuroimaging modalities (Barkovich et al., 2019). In psychometrics, the reliability of a given instrument is typically measured using the intraclass correlation coefficient (Koo and M. Y. Li, 2016). This methodology calculates the correlation between different evaluations using the same psychological instrument, and it is different from the typical Pearson or Spearman correlation in that it accounts for data dependency when multiple methods are applied to the same numbers. Intraclass correlation may represent a more appropriate approach to understanding whether multisite harmonization techniques alter data variability. Its applications have also been extended to neuroimaging, for example by measuring the consistency of structural and functional network metrics across repeated evaluations of the same participants (Telesford et al., 2010; Tsai, 2018). This methodology could be used to test if common data harmonization procedures demonstrate efficiency in preserving within-site variability, a topic that is discussed in detail in Chapter 2.

1.4 Mapping fMRI time series into networks

The approaches discussed above summarized typical pipelines for connectome mapping and network analysis during resting state, but the observation that fMRI signal oscillations over time arise as a consequence of brain activity has been initially and extensively studied using task fMRI. Task fMRI relies on identifying localized functional brain responses elicited following an activity carried out during the scan (Song et al., 2002; Lee et al., 2010; Bowman, 2014). In its most simple forms, task fMRI may imply a finger-tapping activity, or simply visualizing different categories of images separated in time (Drobyshevsky, Baumann, and Schneider, 2006). More complex task designs can involve activities characterized by

increased cognitive demands, such as adaptations of cognitive tasks targeting memory or attention processes that are widely used in behavioral studies of cognition (Diamond, 2013). Early studies observed that distinct regions respond to specific sensory, motor, cognitive or emotional events, which led to the hypothesis that regions that repond to similar events may show synchronized hemodynamic activity during task performance or at rest.

Similar to the functional connectome mapping, linear methods represent a gold standard to quantifying changes in BOLD signal intensity in task fMRI. This typically involves identifying brain regions that become active in response to the onset of events. A statistically significant response localized in the brain can be identified with mass univariate analysis. The word *univariate* describes the fact that each of the time series (i.e., from each voxel) is separately modeled, independent from those extracted from other voxels, thus resulting in massive testing of the same hypothesis across multiple locations in the brain (e.g., voxels). General Linear Modeling (GLM) is commonly used to assess brain activation, and it relies on fitting a predefined model (based on a basis function) to the time series extracted from each voxel (Karl Friston et al., 1994; K. J. Friston, Holmes, et al., 1995). GLM-based mass univariate analysis is relatively straightforward to implement using neuroimaging software, but it may not fully capture the variability of the fMRI signal due to the assumption that the shape of response changes occur uniformly following task events (e.g., the presentation of an image), whereas significant variability has been reported (Cignetti et al., 2016; Duann et al., 2002; Handwerker, Ollinger, and D'Esposito, 2004; Pedregosa et al., 2015; Steffener et al., 2010; Lin et al., 2018). The features extracted based on the GLM are statistical quantities (e.g. beta values) that can be submitted to the group analysis.

Macroscale networks in neuroscience usually map interactions between pairs of brain regions (E. T. Bullmore and Bassett, 2011). However, specific algorithms can construct networks at the level of individual time series. Visibility graphs (Lacasa, Luque, et al., 2008; Lacasa, Nicosia, and Latora, 2015) are a promising tool that can be used for such transformations,

where nodes represent time points instead of brain regions. Studies using visibility graph transformation for functional neuroimaging have started to emerge, for example on signals derived from electroencephalography (EEG) and fMRI. Several reports using EEG highlighted the utility of visibility graphs for mapping large-scale functional connectivity (Ahmadlou, Ahmadi, et al., 2013; Yu, Hillebrand, et al., 2017), machine learning-based detection of epileptic seizures (L. Wang et al., 2017; Mohammadpoory, Nasrolahzadeh, and Haddadnia, 2017) or classification of sleep stages (G. Zhu, Y. Li, and Wen, 2014). One fMRI study assessed the modular structure of the visibility graphs in time series extracted from regions of the limbic system, demonstrating differences between patients suffering from psychiatric disorders and healthy controls (Sannino et al., 2017). These reports used visibility graph transformation during resting state. However, it is not currently understood whether visibility graph topology can uncover information relevant to signal changes originating from brain activity. The hypothesis that temporal networks derived using visibility graphs capture information about brain activity can be tested by means of task fMRI.

Task fMRI may be appropriate for testing whether the topology of temporal graphs derived with visibility transformation contains information about brain activity, because fMRI signal changes evoked during the task have well-controlled onsets and durations, that can be identified in the temporal network topology. An implication of mapping functional neuroimaging data to networks is the possibility of using network science-based tools for characterizing signal oscillations in the brain. This field has the potential to substantially contribute to the analysis of fMRI time series because temporal networks constructed using algorithms such as visibility graphs can be used to extract features that may be able to capture more complex, non-linear properties (Zou et al., 2019) specific to BOLD oscillations (K. J. Friston, Josephs, et al., 1998). However, there is currently no study to test if visibility graphs encode task information in the resulting temporal networks. This limits the application of visibility graph mapping for functional neuroimaging and an important aim of the

current work is to address the gap between dynamic changes in brain signals and the derived temporal networks. Task paradigms that elicit functional responses in sensory cortices such as the primary visual cortex may provide an appropriate means to reliably assess the efficiency of visibility graphs because sensory cortices reliably respond to experimentally designed task events (Buracas, Fine, and Boynton, 2005). Tasks performed during an fMRI scan typically fall into two categories: block or event-related designs (Carrig, Kolden, and Strauman, 2009). The two designs differ in how task events (e.g., the presentation of an image on the screen) are temporally distributed. During a block design, participants may be required to perform an action for slightly longer periods of time, in task blocks that are separated by periods of rest. In event-related designs, task events are shorter in duration (e.g., 1 second) and can be either evenly distanced in time or presented at variable intervals. The usage of an event-related instead of block design allows testing whether the timing to signal peak observed on raw time series corresponds to local visibility graph topology. In Chapter 4, we answer whether visibility graphs can identify task events in synthetic and real event-related fMRI time series during a picture presentation task.

Chapter 2

Multisite harmonization of structural DTI networks in children: An A-CAP Study

The analysis of large, multisite neuroimaging datasets provides a promising means for robust characterization of brain networks that can reduce false positives and improve reproducibility. However, the use of different MRI scanners introduces variability to the data. Managing those sources of variability is increasingly important for the generation of accurate group-level inferences. ComBat is one of the most promising tools for multisite (multiscanner) harmonization of structural neuroimaging data, but no study has examined its application to graph theory metrics derived from the structural brain connectome. The present work evaluates the use of ComBat for multisite harmonization in the context of structural network analysis of diffusion-weighted scans from the Advancing Concussion Assessment in Pediatrics (A-CAP) study. Scans were acquired on 6 different scanners from 484 children aged 8.00-16.99 years [Mean = 12.37 +/- 2.34 years; 289 (59.7 %) Male] approximately 10 days following mild traumatic brain injury (n = 313) or orthopedic injury (n = 171).

Whole brain deterministic diffusion tensor tractography was conducted and used to construct a 90x90 weighted (average fractional anisotropy) adjacency matrix for each scan. ComBat harmonization was applied separately at one of two different stages during data processing, either on the (i) weighted adjacency matrices (matrix harmonization) or (ii) global network metrics derived using unharmonized weighted adjacency matrices (parameter harmonization). Global network metrics based on unharmonized adjacency matrices and each harmonization approach were derived. Robust scanner effects were found for unharmonized metrics. Some scanner effects remained significant for matrix harmonized metrics, but effect sizes were less robust. Parameter harmonized metrics did not differ by scanner. Intraclass correlations (ICC) indicated good to excellent within-scanner consistency between metrics calculated before and after both harmonization approaches. Age correlated with unharmonized network metrics, but was more strongly correlated with network metrics based on both harmonization approaches. Parameter harmonization successfully controlled for scanner variability while preserving network topology and connectivity weights, indicating that harmonization of global network parameters based on unharmonized adjacency matrices may provide optimal results. The current work supports the use of ComBat for removing multiscanner effects on global network topology.

2.1 Introduction

Network neuroscience has become a popular approach to characterize brain structure in vivo in healthy and clinical populations (Bassett and Sporns, 2017; Bullmore and Sporns, 2009; C. Stam, 2014). The structural connectome can be mapped using diffusion-weighted MRI (Bullmore and Sporns, 2009; Gong, He, Concha, Lebel, Donald W Gross, et al., 2009a; Iturria-Medina, Canales-Rodrıéguez, et al., 2007; Iturria-Medina, Sotero, et al., 2008), a non-invasive technique that is sensitive to white matter microstructure (Lerch et al., 2017).

Pediatric mild traumatic brain injury (mTBI) is a prevalent global public health concern (Cassidy et al., 2004; Thurman, 2016; Centers for Disease Control and Prevention [CDC], 2015; Keith Owen Yeates, 2010) that is characterized by subtle and diffuse alterations in brain tissue (reviewed in Mayer, Kaushal, et al., 2018; Lindsey et al., 2021). The neurobiology of pediatric mTBI remains poorly understood (see Mayer, Kaushal, et al., 2018). White matter microstructural alterations can occur after pediatric mTBI, and multiple studies have examined specific white matter tracts using diffusion tensor imaging (DTI; Schmidt et al., 2018; Lindsey et al., 2021; Ashley L Ware, Ayushi Shukla, et al., 2020). Emerging evidence indicates that pediatric mTBI can alter global and regional brain networks (Imms et al., 2019; Sharp, Scott, and Leech, 2014; Ware, Yeates, et al., 2021; Watson, DeMaster, and Ewing-Cobbs, 2019). Thus, network neuroscience may be a potentially promising tool that could provide a robust characterization of network mechanisms involved in this important and highly prevalent neurological disorder.

Large, multisite neuroimaging studies of pediatric mTBI have become increasingly common to reduce false positive results from small samples, increase statistical power, and enhance reproducibility and generalizability of results (Poldrack et al., 2017; Maas et al., 2017b). For instance, the Advancing Concussion Assessment in Pediatrics (A-CAP) study (Keith Owen Yeates et al., 2017) is the largest neuroimaging study of pediatric mTBI to date, with recruitment occurring at 5 children's hospitals across

Canada including longitudinal MRI assessment using 6 different scanners. The A-CAP study has the potential to increase scientific and clinical knowledge about neurobiological outcomes in pediatric mTBI. However, using multiple MRI scanners introduces non-biological data variability due to different scanner systems, models, and sequence protocols, among other factors (Pinto et al., 2020; T. Zhu et al., 2011; A. H. Zhu et al., 2019; Fortin, Parker, et al., 2017). Managing these non-biological sources of variability in multisite studies is increasingly important to generate accurate group-level inferences and enable detection of underlying biological phenomena (Pinto et al., 2020).

ComBat is a widely used method for multisite (multiscanner) harmonization that originated from techniques used for genomics data (W. E. Johnson, C. Li, and Rabinovic, 2007). It is one of the most well-validated tools for multiscanner harmonization of structural neuroimaging data that makes no assumptions about the origin of scanner variation (Fortin, Parker, et al., 2017). ComBat implements a multivariate linear mixed effects regression with terms for biological variables and site to model the features of interest; the model parameters are estimated using an empirical Bayes approach. For diffusion tractography, ComBat has already demonstrated higher performance for multiscanner harmonization than other methods such as removal of artificial voxel effect by linear regression (RAVEL) and functional normalization of metrics (Fortin, Parker, et al., 2017).

Unlike a general linear model approach that includes site or scanner as a fixed effect covariate, ComBat demonstrates better outlier robustness to account for small within-scanner sample sizes by borrowing information across features to shrink estimates towards a common mean (Beer et al., 2020; W. E. Johnson, C. Li, and Rabinovic, 2007). The multiplicative scanner effects are also corrected by removing heteroscedasticity of model errors across scanners (Fortin, Cullen, et al., 2018). Furthermore, ComBat preserves the variability contributed by true biological effects (e.g., sex and age; Fortin, Parker, et al., 2017). However, no study has yet examined whether ComBat is suitable for graph theory metrics derived from the

structural connectome based on DTI.

Unlike tractography, which yields a final value for each white matter tract, connectome analyses use weighted adjacency matrices to calculate network parameters. In tractography or region-of-interest analyses, multisite harmonization is performed on final metrics (e.g., average fractional anisotropy measures; Fortin, Parker, et al., 2017; Kurokawa et al., 2021; Zavaliangos-Petropulu et al., 2019). However, graph theory analysis takes place after connections in a network have been mapped, mathematically represented as an adjacency matrix, and summarized by the computation of network parameters (E. T. Bullmore and Bassett, 2011). Two distinct approaches to data harmonization are therefore possible in network analysis: (1) before the calculation of network parameters (i.e., matrix harmonization; harmonization at the level of connectivity weights), or (2) after the calculation of network parameters (i.e., parameter harmonization). Identifying the optimal timing of data harmonization during data processing and analysis may influence the harmonization of multisite data, and hence has important implications for the accuracy of conclusions drawn from multisite connectivity studies.

To our knowledge, the performance of ComBat for multiscanner harmonization in studies of network topology and neurological disorders has not been evaluated. Therefore, the present study examined the application of two approaches to data harmonization across sites in a sample of DTI scans from children with mTBI or mild orthopedic injury (OI).

2.2 Methods

2.2.1 Study design and procedure

Data were drawn from the Advancing Concussion Assessment in Pediatrics (A-CAP) study (Keith Owen Yeates et al., 2017), a multisite prospective, cohort study with longitudinal follow-up in children [Mean age (range) = 12.37 +/- 2.34 years (8.00-16.99 years); 289 (59.7 %) Male] with pediatric mTBI (n = 313) or mild orthopedic injury (OI; n = 171). Briefly, children were recruited within 48 hours of injury from 5 children's hospitals across Canada, all of which were members of Pediatric Emergency Research Canada (PERC; Bialy et al., 2018), and returned for 3 post-injury follow-up assessments: post-acute (targeted for 10 days post-injury), 3 months, and 6 months. Injuries and acute signs and symptoms were assessed during an initial emergency department visit that took place within 48 hours post-injury.

The study was conducted with the approval of the research ethics board at each study site. All participants provided written informed assent and parents/guardians provided written informed consent (Keith Owen Yeates et al., 2017). This study examined data from the MRI scans collected during the post-acute visit, as previously described (Ayushi Shukla et al., 2021).

2.2.2 Diffusion MRI

Eligible participants completed a 3T MRI scan without sedation at the post-acute visit (see Ayushi Shukla et al., 2021 for details). In brief, thirty diffusion-weighted images with different diffusion gradient encoding directions were acquired at b=900 s/mm^2, along with 5 images at b=0 s/mm^2, with 2.2 mm isotropic resolution at all sites (General Electric: TR/TE=6, 12 s/70, 90 ms; Siemens: 6.3, 7.8 s/55, 90 ms; Keith Owen Yeates et al., 2017). Data collected in Montreal was acquired using 2 different scanners, coded as Montreal 1 and Montreal 2, for a total of

6 scanners ("sites"): Calgary (General Electric), Edmonton (Siemens), Montreal 1 (General Electric), Montreal 2 (Siemens), Ottawa (Siemens) and Vancouver (General Electric).

2.2.2.1 Quality assurance

Visual quality checks of all raw images were conducted to identify and exclude scans with structural abnormalities/incidental findings, scanner artifacts (e.g., warping), incomplete acquisition, or not collected using the standardized scan parameters. Data that passed the initial quality assessment were subsequently rated for motion by two trained analysts. Discrepancies were resolved through a third reviewer blind to initial ratings. Diffusion-weighted volumes with severe motion artifact were removed, and any scans with >7 volumes with severe motion artifact were excluded from subsequent analysis (Ware, Shukla, et al., 2022).

2.2.2.2 Structural connectome

Detailed image processing methodology has been previously described (Ware, Yeates, et al., 2021). Briefly, ExploreDTI (AJBSJJDK Leemans et al., 2009) was used to preprocess diffusion images, calculate the diffusion tensor, conduct whole brain fiber tractography, and compute an adjacency matrix for each participant. Preprocessing included correction for signal drift (Vos et al., 2017), eddy currents, subject motion with rotation of the B-matrix (Alexander Leemans and Jones, 2009), and susceptibility distortions (Veraart et al., 2013). A deterministic streamline approach was used for whole brain fiber tractography (randomized seed points; seed and tractography FA threshold = 0.10; step size = 0.50 mm; angle threshold = 30°; step size = 0.5 mm; streamline length 50-500 mm). The resulting whole brain fiber tractography was extracted and used to compute an adjacency matrix for each participant.

The automated anatomical labeling (AAL-90, Tzourio-Mazoyer et al., 2002) template was used to define 90 nodes in native (diffusion) space

using functions from open-source software packages in MATLAB R2019a (see Ware, Yeates, et al., 2021). Fully connected 90 x 90 adjacency matrices were constructed using the average FA of passing fibers among nodes in ExploreDTI for each participant and an absolute threshold of 0.1.

2.2.3 Global Network Metrics and Multisite Harmonization

The following global network parameters were calculated in MATLAB using the GRETNA software toolbox (http://www.nitrc.org/projects/gretna; J. Wang et al.,2015): global efficiency, global clustering coefficient, small worldness, modularity, and density. Network parameters were normalized against 1,000 randomly generated matrices.

Global network parameters were evaluated before harmonization and after two different harmonization approaches: matrix harmonization and parameter harmonization. The steps used for each approach are summarized in **Figure 2.1**. For both harmonization approaches, ComBat v1.0.5 (https://github.com/Jfortin1/ComBatHarmonization/tree/master/R) was conducted in R v3.6.3 (R Core Team, 2020; https://www.R-project.org/) to harmonize the data for scanner differences. A covariate matrix with group (mTBI/OI), age at injury, and biological sex was included to preserve this variance:

$$mod <- model.matrix(\sim injury + age + gender)$$

2.2.3.1 Matrix harmonization

For matrix harmonization, weighted connectivity matrices were harmonized for multiple scanners and global network parameters were calculated using the harmonized connectivity matrix for each participant (see **Figure 2.1**). First, the lower diagonal values of each connectivity matrix were extracted to construct a dataframe of 4,005 columns corresponding

to node connection pairs among the 90 defined brain regions (nodes), excluding self-connections [i.e., principal diagonal; (n(n-1))/2]. This was done because undirected adjacency matrices are diagonally symmetrical. ComBat was then used to harmonize those extracted values:

$$neuroCombat(dat = LowerDiagonal, batch = Site, mod = mod)$$

After the harmonization of the extracted connectivity weights, the adjusted square and symmetric weighted matrices were reconstructed for each participant and subsequently used to calculate global network parameters. During matrix harmonization, many of the connection weights that were 0 before harmonization (i.e., indicating that no connection existed between two nodes) were transformed to negative values. To correct for this transformation, an additional masking step was applied to reassign negative weights to 0 prior to graph analysis. Specifically, the masking step multiplied the binary connectivity matrix derived before harmonization with the harmonized weighted connectivity matrix for each participant (see **Figure 2.1**).

2.2.3.2 Parameter harmonization

For parameter harmonization, the raw global network metrics (i.e., calculated before harmonization) were harmonized for multiple scanners using ComBat. Each parameter was harmonized in separate models because the distribution of each parameter is not necessarily related to the distribution of other parameters. The empirical bias estimation option was not applied (i.e., eb=FALSE) during parameter harmonization because each global network parameter was harmonized separately (i.e., number of features $<$ n). For each global network metric, the following model was used to harmonize the data:

$$neuroCombat(dat = Parameter, batch = Site, mod = mod, eb = FALSE)$$

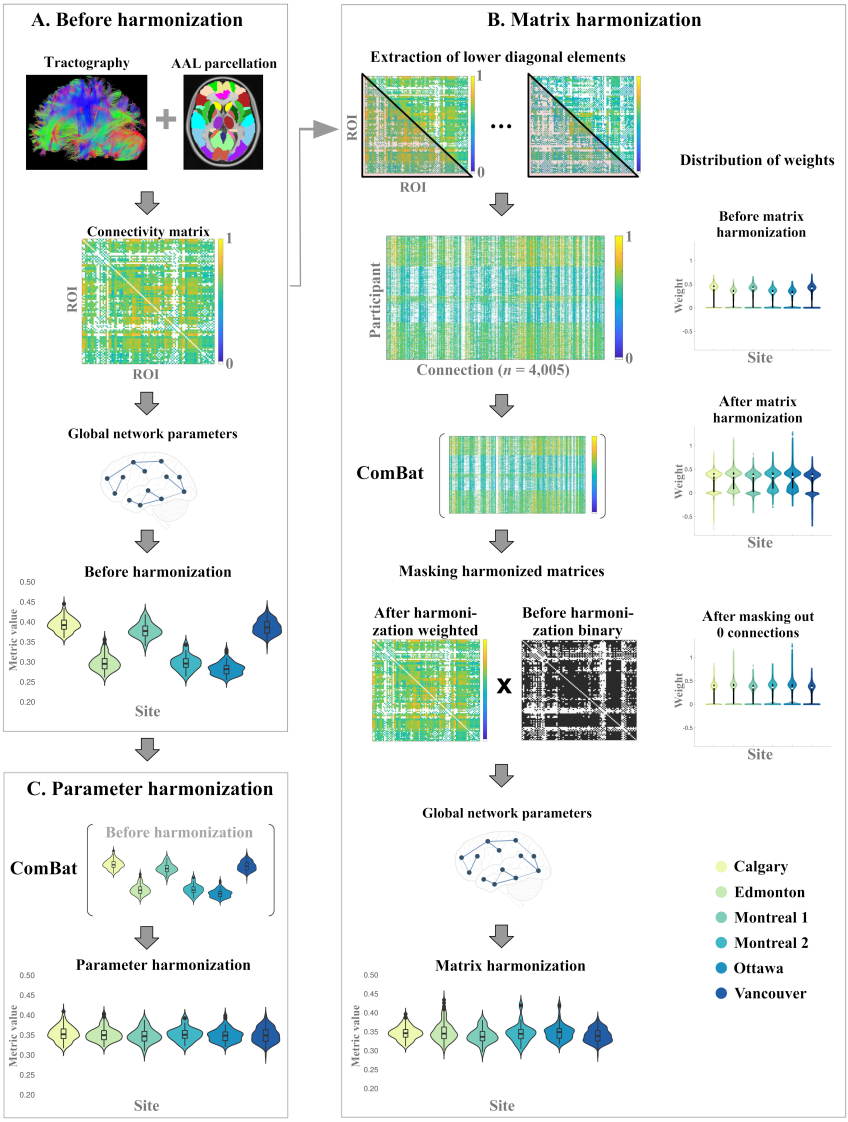

Figure 2.1: Overall study procedure illustrating the data processing steps for the generation global network parameters (A) before harmonization, and the implementation of (B) matrix harmonization and (C) parameter harmonization.

2.2.4 Statistical analysis

2.2.4.1 Harmonization performance assessment

Statistical analyses were conducted using R v3.6.3. To evaluate the performance of each harmonization approach (i.e., adjacency matrix or network parameters), the effect of site was examined using separate one-way ANOVA models for each global network parameter. Non-significant scanner effects ($p > 0.05$) were interpreted as a successful removal of variability due to different scanners.

The proportion of significant ($p < 0.05$) post-hoc pairwise between-site comparisons was evaluated by calculating the number of significant uncorrected pairwise comparisons across scanners, divided by the total number of possible pairwise comparisons (i.e., $n = 15$). Correction for multiple comparisons was not applied for post-hoc t-tests followup analysis, providing a more conservative evaluation of scanner effects.

2.2.4.2 Within-scanner consistency following data harmonization

The within-scanner consistency of the global network metrics before (unharmonized) and after each harmonization approach (matrix harmonization, parameter harmonization) was examined by calculating the Intraclass Correlation Coefficient (ICC), with ICC <0.50, $0.50 \leq$ ICC $<$ 0.75, $0.75 \leq$ ICC < 0.90, and ICC ≥ 0.9 indicative of poor, moderate, good, and excellent consistently, respectively (Koo and M. Y. Li, 2016). Successful harmonization would reduce the effect of site while preserving the within-scanner variability for each parameter observed before harmonization.

2.2.4.3 Biological variability

To evaluate whether ComBat harmonization preserves biological variability, analysis of covariance (ANCOVA) was used to examine the effect of

site, age at injury, sex, and group (mTBI, OI) on each network parameter. Significant effects involving age at injury were further examined using Pearson correlations, which were compared using a back-transformed average Fisher's Z procedure for dependent and overlapping correlations (Hittner, May, and Silver, 2003), as implemented using the cocor package (Diedenhofen and Musch, 2015). Overlapping correlations were used to conduct the following pairwise comparisons of age correlations: (1) matrix harmonization vs unharmonized data, (2) parameter harmonization vs unharmonized data, and (3) parameter harmonization vs matrix harmonization.

Within-scanner age correlations on the unharmonized data were calculated to provide a reference value for the expected age correlation for each network parameter following harmonization. The reference value was calculated based on the means of within-site age correlations, weighted by the corresponding sample size of each scanner. Weighted means were calculated because sites with a greater number of participants may influence the correlation values to a greater extent than sites with smaller cohorts. Successful preservation of age-related biological variability across all scanners following harmonization would approximate the weighted mean of within-scanner age-correlations. Group differences between mTBI and OI were calculated using *t*-test.

2.3 Results

2.3.1 Presence of site/scanner effects before harmonization

Before harmonization, all global network metrics differed by site (see **Table 2.2**; **Figure 2.2**, A; **Figure 2.3**, A). The largest site effect was observed for global efficiency [$F(5) = 651.08$, $p < .001$], with 14 of 15 (93%) significant between-site comparisons, followed by modularity [$F(5) = 309.87$, $p < .001$; 13 (86%) significant between-site comparisons], density [$F(5) = 286.23$, $p < .001$; 13 (86%) significant between-site comparisons], small worldness [$F(5) = 182.93$, $p < .001$; 12 (80%) significant between-site comparisons] and clustering coefficient [$F(5) = 86.38$, $p < .001$; 12 (80%) significant between-site comparisons].

2.3.2 Matrix harmonization

Main effects of site remained significant for global network metrics after matrix harmonization (**Table 2.2**; **Figure 2.2**, B; **Figure 2.3**, B). However, pairwise site differences were less pervasive after harmonization for global efficiency [$F(5) = 3.88$, $p < .001$; 4 (26%) significant between-site comparisons] and small worldness [$F(5) = 170.69$, $p < .001$; 11 (73%) significant between-site comparisons], but not for modularity [$F(5) = 158.06$, $p < .001$; 13 (86%) significant between-site comparisons], density [$F(5) = 286$, $p < .001$; 13 (86%) significant between-site comparisons] or clustering coefficient [$F(5) = 295.44$, $p < .001$; 15 (100%) significant between-site comparisons].

Within-site consistency of unharmonized and matrix harmonized metrics ranged from poor to excellent (**Figure 2.3**, B). The highest consistency was observed for density [ICC = 1.00], which is the only parameter that measures the presence of connections but ignores their weights. Global efficiency and modularity also had excellent ICCs [Mean (range) = 0.96 (0.91, 0.99) for both], whereas consistency was good for small worldness [Mean (range) = 0.85 (0.57, 0.95)] and poor for clustering coefficient [Mean

(range) = 0.21 (0, 0.62)].

2.3.3 Network parameter harmonization

Site was not significantly associated with global network metrics after parameter harmonization (**Table 2.2**; **Figure 2.2**, C; **Figure 2.3**, C). The within-site pre-post harmonization ICCs (**Figure 2.3**, C) were consistently excellent for global efficiency [Mean (range) = 0.99 (0.99, 1)] and density [Mean (range) = 0.98 (0.97, 1)], and good to excellent for clustering coefficient [Mean (range) = 0.97 (0.86, 1)] and modularity [Mean (range) = 0.91 [0.85, 0.99)] and moderate to excellent for small worldness [Mean (range) = 0.86 (0.73, 0.99)].

2.3.4 Relationships between network topology and age before and after harmonization

Age significantly correlated with the following unharmonized network parameters (**Figure 2.4**, A): global efficiency (R = 0.16, p <.001), clustering coefficient (R = 0.13, p <.003) and density (R = 0.12, p <.006). After matrix harmonization (**Figure 2.4**, B), the correlation between age and global efficiency (R = 0.38, p <.001) was larger than before harmonization (z = 3.63, p <.001). After parameter harmonization, age-correlations increased (**Figure 2.4**, C) for efficiency (R = 0.44, p <.001), clustering coefficient (R = 0.21, p <.001) and density (R = 0.27, p <.001), although only age correlations for efficiency (z = 4.71, p <.001) and density (z = 2.40, p <.016) were significantly larger compared to the unharmonized data.

No significant correlations with age were observed for modularity and small worldness before harmonization, but modularity significantly correlated with age following matrix harmonization (R = -0.11, p =.018), and both parameters showed significant age relationships following parameter harmonization (modularity: R = -0.15, p <.001; small worldness: R = -0.13, p <.003), although the coefficients were not significantly higher compared to the unharmonized data (p >.05). Clustering coefficient (z =

0.26, $p < .008$) and density ($z = 2.40$, $p < .016$) were significantly stronger following parameter as compared to matrix harmonization. Within-group age correlations are reported in **Table 2.4**. No significant effects of sex or group were observed for any of the network parameters (see **Table 2.4**).

Table 2.1: Demographic information for the participants at each site.

Site	Participants *n* (%)	Sex *n* (%) male	Age* M (SD) years	Group* *n* (%) mTBI	DPI* M (SD)
Calgary	120 (24.7%)	71 (59.1%)	12.9 (2.2)	83 (69.1%)	8.8 (3.3)
Edmonton	114 (23.5%)	67 (58.7%)	12.5 (2.3)	75 (65.7%)	9.3 (5.1)
Montreal 1	28 (5.7%)	18 (64.2%)	11.4 (2.0)	25 (89.2%)	10.3 (4.2)
Montreal 2	20 (4.1%)	10 (50%)	12.5 (2.2)	15 (75%)	12.4 (4.8)
Ottawa	57 (11.7%)	30 (52.6%)	11.9 (2.2)	39 (68.4%)	15.8 (4.7)
Vancouver	145 (29.9%)	93 (64.1%)	12.0 (2.4)	76 (52.4%)	11.7 (5.1)
Total	484	289 (59.7%)	12.3 (2.3)	313 (64.4%)	10.9 (5.1)

Note. * Significant effect of site on age ($F = 3.73$, $p < .01$), group($\chi^2 = 18.3$, $p < .001$) and DPI ($F = 21.5$, $p < .001$); DPI - days post injury, M - mean, SD - standard deviation.

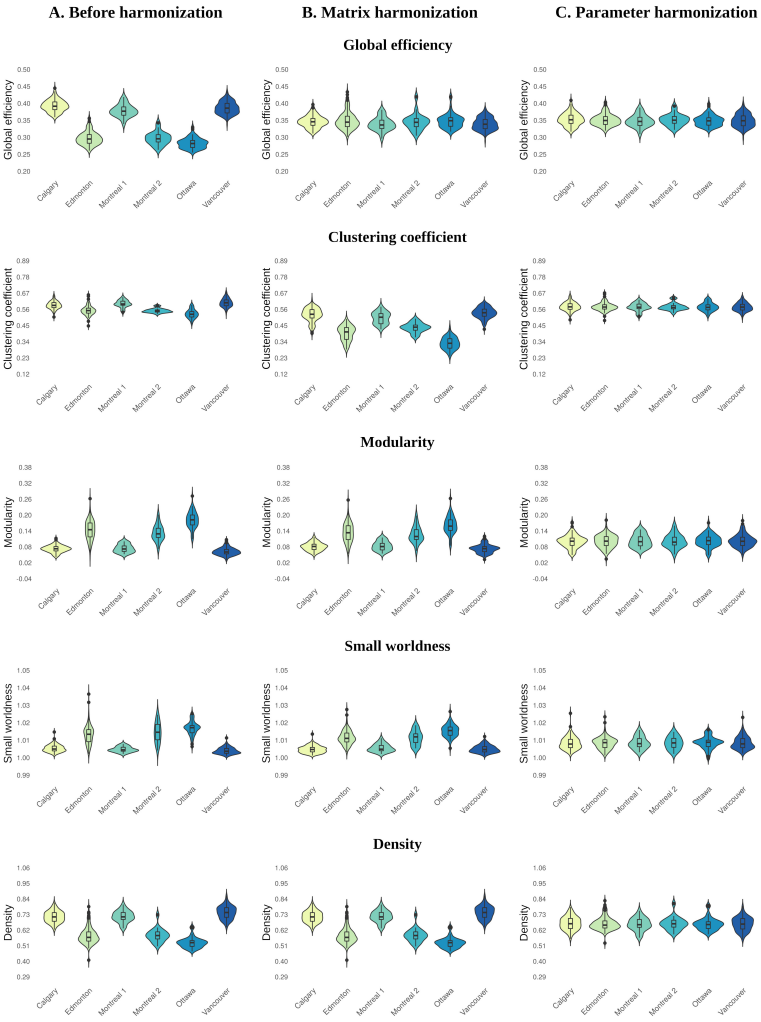

Figure 2.2: Violin plots illustrating the distribution of values across sites for global network parameters calculated (A) before harmonization, after (B) matrix and (C) parameter harmonization.

Table 2.2: Results summarizing the overall effect of site on global metrics before harmonization, after matrix harmonization and after parameter harmonization.

Parameter	Before harmonization			Matrix harmonization			Parameter harmonization		
	Overall effect of site		# pairwise between site differences	Overall effect of site		# pairwise between site differences	Overall effect of site		# pairwise between site differences
	F	η^2	p < 0.05 (%)	F	η^2	p < 0.05 (%)	F	η^2	p < 0.05 (%)
Global efficiency	651***	0.87	14 (93%)	3.88**	0.04	4 (26 %)	0.68	<0.01	0
Clustering coefficient	86.3***	0.47	12 (80%)	295***	0.76	15 (100 %)	0.19	<0.01	0
Modularity	309***	0.76	13 (86%)	158***	0.62	13 (86 %)	0.09	<0.01	0
Small worldness	182***	0.66	12 (80%)	170***	0.64	11 (73 %)	0.02	<0.01	0
Density	286***	0.75	13 (86%)	286***	0.75	13 (86 %)	0.25	<0.01	0

Note. ** $p < .001$; *** $p < .0001$.

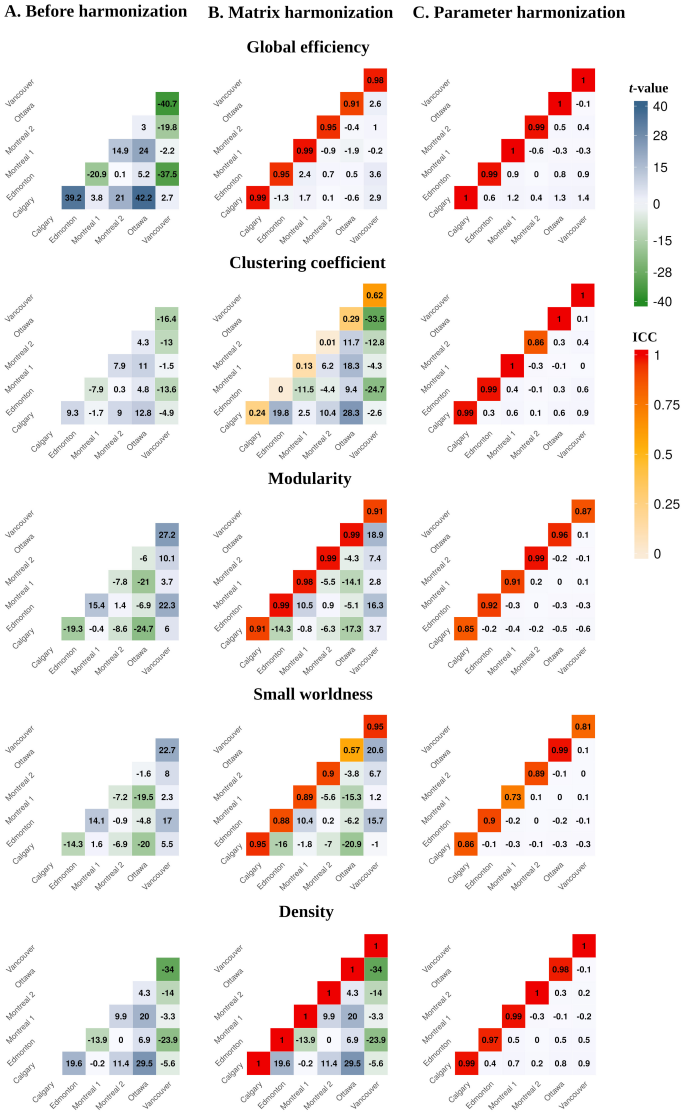

Figure 2.3: Heatmaps illustrating pairwise between-site differences and *t*-values (lower diagonal) and within-site ICCs (principal diagonal) for the global network parameters calculated (A) before harmonization and after (B) matrix and (C) parameter harmonization.

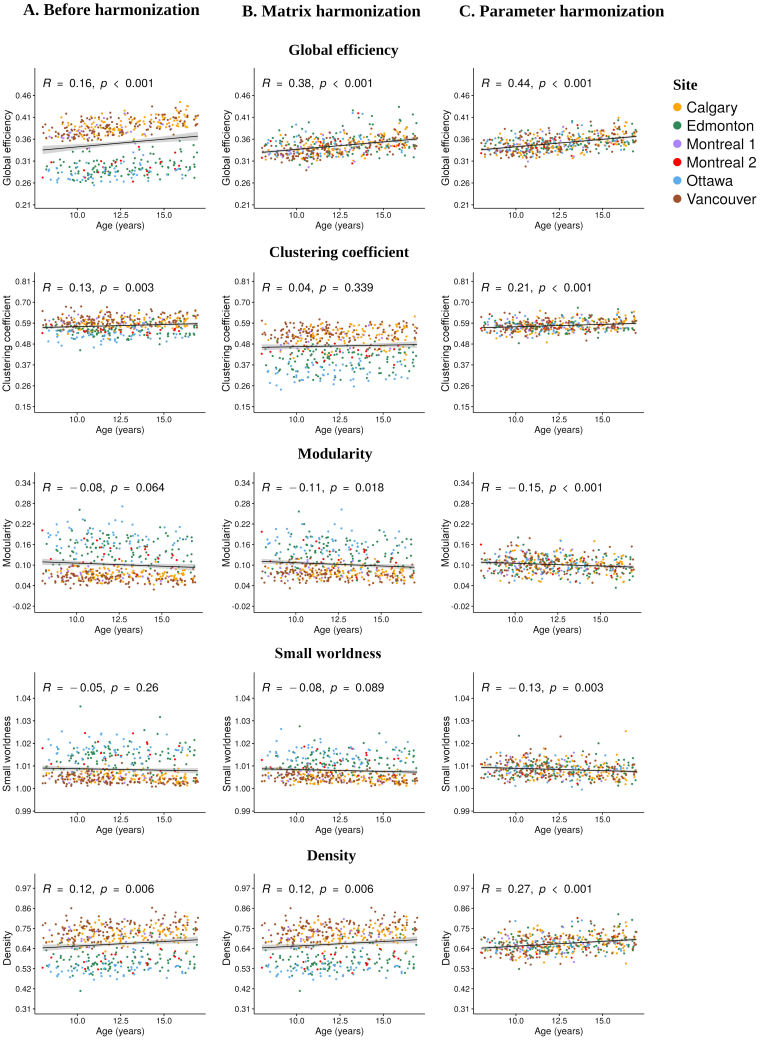

Figure 2.4: Scatter plots illustrating the Pearson correlations between age at injury and each global network parameter calculated (A) before harmonization and after (B) matrix and (C) parameter harmonization.

Table 2.3: Pearson correlation coefficients between age and each global parameter within site (scanner) before harmonization.

Site (scanner)	Efficiency	Clustering coefficient	Modularity	Small worldness	Density
Calgary	0.52***	0.39***	-0.29*	-0.26*	0.29*
Edmonton	0.27*	0.10	-0.14	0.03	0.19*
Montreal 1	0.42*	0.12	-0.12	-0.20	0.17
Montreal 2	0.29	-0.14	-0.44	-0.10	0.33
Ottawa	0.24	0.15	-0.05	-0.06	0.13
Vancouver	0.56***	0.22*	-0.22*	-0.30***	0.36***
Weighted mean	0.43	0.21	-0.20	-0.17	0.26

Note. * p <0.05; ** p <.001; *** p <.0001.

Table 2.4: Results summarizing the effect of age at injury, sex and group before harmonization, after matrix harmonization and after parameter harmonization (*F* values).

Parameter	Before harmonization			Matrix harmonization			Parameter harmonization		
	Age	Sex	Group	Age	Sex	Group	Age	Sex	Group
Global efficiency	104.90***	1.09	0.79	76.21***	0.34	1.10	110.80***	1.45	0.62
Clustering coefficient	20.86***	0.26	1.56	1.65	0.14	0.70	21.31***	0.09	1.21
Modularity	12.98***	1.52	0.25	13.59***	2.31	0.01	11.06***	1.42	0.02
Small worldness	3.98*	0.89	0.01	4.40*	0.55	0.04	8.65**	1.06	0.05
Density	34.72***	1.69	0.32	34.72***	1.69	0.32	34.93***	2.29	0.10

Note. * $p < 0.05$; ** $p < 0.001$; *** $p < 0.0001$.

2.4 Discussion

The popularity of large, representative datasets from collaborative, multisite research initiatives and structural connectomics has increased in recent years. Previous studies demonstrated that ComBat can control for site (scanner) differences while preserving biological variability (e.g., due to group, age, sex) for several MRI modalities (Pomponio et al., 2020; Fortin, Cullen, et al., 2018; Fortin, Parker, et al., 2017; Yu, Linn, et al., 2018). This is the first study to validate the use of ComBat for the structural connectome. Here, ComBat was successfully used to harmonize structural connectivity data based on diffusion-weighted MRI across multiple scanners ("sites"). Parameter harmonization reduced the variability associated with different scanners to a greater extent than matrix harmonization, although both approaches reduced site differences in global network metrics. As expected, both harmonization approaches also preserved biological effects of age on network parameters. Moreover, expected age-related associations with global network parameters were stronger after applying parameter as opposed to matrix harmonization. Overall, the results extend the validity of using ComBat harmonization to network parameters derived using diffusion-weighted MRI.

Parameter harmonization showed superior performance for removing scanner effects compared to matrix harmonization. Furthermore, parameter harmonization is more computationally efficient. Matrix harmonization requires a series of steps that involve value translation. Specifically, connectivity weights were deconstructed from the matrices by extracting the lower (or upper) diagonal elements, organized in a high dimensional data frame for harmonization, and reconstructed back in square matrices following harmonization. In some instances, this approach transformed connection weights that were initially 0 (i.e., no connection exists between two nodes in unharmonized data) to negative values, requiring an additional step reassigning these values to zero before graph analysis. Thus, matrix harmonization preserved the location, but not the strength of connections among node pairs. In contrast, parameter harmonization

requires only one step. This appears beneficial in preserving the true global properties of the network, as illustrated by the reduced variability of the within-site consistency between the parameter harmonized and unharmonized global network metrics (see **Figure 2.3**).

Before harmonization, global efficiency exhibited more robust site effects than other measures, such as the clustering coefficient. Matrix harmonization reduced (e.g. global efficiency), introduced (e.g., clustering coefficient) or maintained (e.g., density) site effects compared to the unharmonized data. The variable performance of matrix harmonization across different metrics may indicate that properties of the network other than the pairwise connection strengths are affected by scanner. Except for density, global parameters included in the present analysis encode information about the topology (i.e., location) as well as the weights of connections among distinct brain regions. Density, which reflects the number of connections regardless of their strengths, did not demonstrate differences in the magnitude of site effects following matrix harmonization (see **Figure 2.2** and **Figure 2.3**), indicating that site differences are present in topological properties of the network beyond the strengths of pairwise connections (e.g., the number or location of connections).

In addition, clustering coefficient quantifies segregation across brain regions (i.e., nodes) by counting the occurrence of existing connections between groups of three nodes. Since matrix harmonization does not alter the location of connections, groups of connected nodes maintain their configuration before and after harmonization. Furthermore, the magnitude of scanner effects might differ slightly among connections, and matrix harmonization might differently impact the reciprocal connection strengths across groups of nodes (i.e., it targets pairs of nodes), potentially explaining the variable performance for removing site effects in the case of clustering coefficient (see **Figure 2.3**, A and B). These topological properties may be better controlled by parameter harmonization, because global parameters already encode this information.

Correlations between age and network parameters were generally larger

following both harmonization approaches, but were slightly more robust following parameter harmonization. One exception was the relationship between age and clustering coefficient, which weakened following matrix harmonization. This is in line with the other results, suggesting that matrix harmonization may be problematic for clustering coefficient.

The detection of significant age effects following parameter harmonization, even in the absence of significant correlations for the unharmonized data, raises the question of whether additional variability was added to the data during harmonization that might have artificially boosted the relationship between age and network topology. Further analyses suggest this is not the case, because the age correlation following parameter harmonization were closer to the weighted means of within-scanner correlations before harmonization (see **Table 2.3**).

In addition, previous studies show relationships between age and global network topology in typical development (Z. Chen et al., 2013; Koenis et al., 2015; Lim et al., 2015) and children with TBI (Watson, DeMaster, and Ewing-Cobbs, 2019). This indicates that parameter harmonization may better preserve age-related biological variability compared to matrix harmonization and to the unharmonized data, although differences between the two harmonization approaches were small.

The children with mTBI and OI did not differ in any global network metrics before or after each harmonization approach. This was expected given that DTI and NODDI indices of white matter microstructure did not differ between groups previously in this sample (Ayushi Shukla et al., 2021; Ware, Yeates, et al., 2021) and other pediatric samples at similar time points (Wilde et al., 2019). Another study compared a subset of this sample (children recruited at the Calgary site) to typically developing children and also did not find global or regional (nodal) network differences between mTBI and mild OI groups post-acutely, but did find an effect of injury more generally relative to typical development (Ware, Yeates, et al., 2021).

In the present analysis, matrix harmonization introduced negative values

in the connectivity matrices. Interestingly, the negative weights correspond to unharmonized 0 values, indicating that in some cases, missing connections between pairs of regions can receive negative values following ComBat harmonization. Across the A-CAP sample, the insertion of negative values has occurred across 13.4% of the total connections, however, these values were generally very small, with a mean of -0.036 (see **Figure A.1**). To address this issue, the negative values were set back to 0, which preserves the original topology of participant-level adjacency matrices, by preventing the insertion of new connections following the harmonization of connectivity weights. Data scaling procedures may provide an alternative to handle the occurrence of negative values, however, scalar transformations can impact the participant-level topology by the addition of positive weights to the values that were 0 both, before and after harmonization. In this scenario, the 0-connections remaining in the matrices following re-scaling would be represented by the minimum negative values, resulting in the insertion of positive weights across true 0 connections, impacting the original topology at participant level. Future analyses might address how different strategies for the scaling of connectivity weights could be applied to reduce site effects while preventing the participant-specific network topology, which also implies (at least partially) the preservation of within-site variability. This limitation of the current work, however, emphasizes that matrix harmonization provides a more challenging method for managing between-site variability, and underlines the efficiency of parameter harmonization for the specific application of graph analysis.

The current study did not address the effect of data harmonization applied prior to the generation of adjacency matrices, which is an additional possibility to account for the variability across different scanners (e.g., using methods described by Fortin, Sweeney, et al., 2016; Leek et al., 2012; Fortin, Parker, et al., 2017). It has been suggested that connectome generation can be stable across scanners based on the derived network parameters (Bonilha et al., 2015). While future studies may consider this, data harmonization prior to connectome construction is increased in com-

plexity, involving additional processing steps. These include warping the data into a common space and deconstructing brain images to build a voxel by participant data frame, which does not allow for the construction of adjacency matrices in native diffusion space. Following voxelwise harmonization, data would need to be reconstructed into subject-specific brain images (i.e., harmonized FA maps), which may impose substantial feasibility challenges due to the high computational complexity and number of additional transformations involved in this process.

There are some limitations to the current work. Weighted connectivity matrices were analyzed in this study; future multisite studies might examine whether differences in binary matrices relate differently to the effects of site. We did not assess the influence of different thresholds on harmonization. In addition, the current study used only one parcellation for the construction of adjacency matrices, and future studies might focus on whether other parcellations are similarly affected by site effects particularly when running matrix harmonization. While most methods use similar preprocessing steps, slight variations in these steps and how they are applied can impact calculated diffusion metrics, and thus may be important to explore in future studies. Data acquisition in the current study included single shell diffusion-weighted data. Multishell acquisition protocols may be differently affected by site effects, which might be addressed in future studies. Lastly, the current study used deterministic tractography, and future analyses might consider testing the effect of harmonization on networks derived using probabilistic tractography, as the two approaches have been shown to differ in terms of within- and between-scanner consistency (Bonilha et al., 2015).

2.4.1 Conclusions

The present paper validates the utility of ComBat harmonization in the context of graph theoretical analysis for structural connectivity derived from DTI. The harmonization of global parameters derived from unharmonized adjacency matrices provided superior performance as compared with the harmonization of connectivity weights for removing between-site differences, preserving the within-site variability and preserving age-related biological variability in the data.

Chapter 3

Functional network alterations in mild traumatic brain injury

Mild traumatic brain injury (TBI) is the most common form of TBI across the pediatric population, but its effects on global functional brain network topology are not well understood. The post-acute and longitudinal impact of mild TBI on global network topology was assessed in a multi-site resting-state study. Functional magnetic resonance imaging (fMRI) was recorded post-acutely (n = 502, mean age = 12,5 +/- 2,3 years, 59,7% males), at 3 months (n = 197, mean age =12,3 +/- 2,4 years, 56,8% males) and 6 months post-injury (n = 219, mean age = 12,5 +/- 2,4 years, 62,1% males) from children (N = 671) with mild TBI (n = 386, mean age = 12.34 +/- 2.41 years, 62.2% males) and orthopedic injury (OI; n = 199, mean age = 12.50 +/- 2.17 years, 55.8% males). Global and local graph theory metrics were derived using proportionally thresholded weighted adjacency matrices based on Pearson correlation between pairs of regions defined using the 90 ROI AAL atlas. Following ComBat harmonization, multiple linear mixed-effects models were used to investigate the rela-

tions of group (mild TBI, OI), time post-injury, age at injury, sex, and three-way interactions of group by time by age and group by time by sex and their lower order interactions controlling for the random effect of participant. This approach was repeated to compare graph metrics among symptom groups, by classifying mild TBI with and without persistent symptoms based on pre-injury and 1-month post-injury symptom ratings. The false discovery rate (FDR) was used to correct for multiple comparisons. Functional abnormalities at both global and local network levels were demonstrated in children following mild TBI relative to OI, and those differences were moderated by time post-injury, age, and sex. Alterations in degree centrality, nodal efficiency, and clustering coefficient amplify 3 months post-injury and appear more distributed across parietal, temporal, and occipital cortices. These abnormalities occur more frequently in females, and tend to reduce at 6 months post-injury, localizing across occipital areas. Global metrics differed at 3 months post-injury, indicating a lower clustering coefficient in older mild TBI children and in females with persistent symptoms relative to OI, probably reflecting a more distributed pattern of local alterations present at 3 months after the injury. Network topology differentiated mild TBI with from those without persistent symptoms or OI longitudinally, however with limited prognostic utility based on the post-acute between-group differences.

3.1 Introduction

The median annual incidence of Traumatic Brain Injury (TBI) across children and youths has been estimated at 691 per 100,000 population treated in emergency departments and 74 per 100,000 treated in hospital (Thurman, 2016), although the real incidence might be underestimated because many individuals do not seek medical attention (Setnik and Bazarian, 2007). The most common causes of TBI include falls (especially among children between 5 and 14 years) and motor vehicle injuries (particularly among youths aged 15 and older), and the majority of injuries are classified as mild in severity (Cassidy et al., 2004; Thurman, 2016). Mild TBI can lead to post-concussive symptoms manifested as psychical, cognitive, emotional, and somatic changes, including dizziness, confusion, irritability, and fatigue (Zemek, M. H. Osmond, and Barrowman, 2013), and persistent symptoms can occur and last for 6 months or more (Grabowski et al., 2017). Clinical management of mild TBI is affected by the scarcity of sensitive and specific diagnostic tools that account for its heterogeneous pathophysiology (Martinez and Stabenfeldt, 2019).

Mild TBI is associated with axonal damage (Blennow et al., 2016; Langlois, Rutland-Brown, and Wald, 2006), which may lead to changes in brain function, for example by altering the information flow establishing communication between brain regions (Y. Zhou and Lui, 2013). Structural damage at microscopic and molecular levels associated with mild TBI is not detectable by conventional imaging (Shin et al., 2017). The analysis of temporal correlations based on spontaneous blood-oxygenation-level- dependent (BOLD) oscillation using resting-state functional MRI (rsfMRI) can be used to map brain functional communication noninvasively (Stephen M. Smith et al., 2013; Avena-Koenigsberger, Misic, and Sporns, 2018). Functional neuroimaging based on rs-fMRI is promising for the study of mild TBI, because patients with no structural abnormalities following conventional structural imaging (e.g., CT/MRI) can demonstrate alterations in functional connectivity (Palacios et al., 2017; Shin et al., 2017)

Network neuroscience uses mathematical tools such as graph theory to characterize the overall brain topology (Bassett and Sporns, 2017). Brain injuries can change information flow between regions, and may alter local and global level communication (Alstott et al., 2009; Aerts et al., 2016). The description of the functional brain architecture based on graph theory can help better understand mild TBI pathophysiology by characterizing disruptions that affect overall brain communication (C. Stam, 2014). Combined with functional neuroimaging, graph theory could overcome the heterogeneity (e.g., in terms of location) of the injuries observed in the pediatric population with mild TBI (Dennis et al., 2017).

Currently, it is not understood how functional brain topology is affected following mild TBI in children. In the adult population, contrasting findings were reported, including increased, reduced, or no differences in global efficiency (Kim et al., 2022; Yan et al., 2017; Horn et al., 2017; Yan et al., 2017; Caeyenberghs et al., 2017; Churchill et al., 2021; Pandit et al., 2013), clustering coefficient (Kim et al., 2022; Horn et al., 2017; Yan et al., 2017; Y. Zhou, 2017; Pandit et al., 2013), modularity (Han et al., 2014; Messé et al., 2013), small-world topology (reviewed in Caeyenberghs et al.,2017 and overall functional connectivity (reviewed in Morelli et al.,2021). This inconsistency may mimic the heterogeneity of mild TBI, because the presence of functional alterations may vary depending on moderating variables which are not properly accounted for, including the presence of postconcussive symptoms (Si et al., 2018; Mortaheb et al., 2021; Madhavan et al., 2019; Lange et al., 2015; Shumskaya et al., 2012), time post-injury (Belanger et al., 2005; Ashley L Ware, Keith Owen Yeates, et al., 2022), or differences in age (Bittencourt-Villalpando et al., 2021; Imms et al., 2019) and gender (Si et al., 2018; T. M. Yeates et al., 2022).

The analysis of the functional brain architecture based on graph theory could help advance knowledge about neural markers that are specific and sensitive to pediatric mild TBI and occur in global and local network functioning (C. Stam, 2014). Despite this, little is known about the functional connectome in pediatric mild TBI. Two underpowered studies have examined the functional connectome in children with moderate and

severe injuries (i.e., complicated mild, moderate, and severe TBI) and found atypical global network organization, including lower modularity, higher small worldness, and lower assortativity; (Botchway et al., 2022), and altered rich-club organization (Verhelst et al., 2018). Studies addressing structural connectome alterations have found evidence indicative of increased segregation and reduced efficiency of information flow, which can occur after mild TBI in children and suggest that the functional connectome could also be disrupted, at global and local network levels (Ware, Yeates, et al., 2021; Imms et al., 2019).

To address significant knowledge gaps, this prospective, longitudinal study investigated whether the functional topology of the brain and its trajectory across time post-injury is altered following pediatric mild TBI, and whether alterations are related to symptom persistence at 1-month post-injury. Specifically, changes between the post-acute (e.g., 2-33 days post-injury) and chronic (i.e., 3- or 6-months post-injury via random assignment) functional connectome of children with mild TBI or mild orthopedic injury (OI) were compared.

3.2 Methods

3.2.1 Study Design and Procedure

Data were drawn from the Advancing Concussion Assessment in Pediatrics (A-CAP) study (Keith Owen Yeates et al., 2017). This multisite study used a prospective, concurrent cohort design to study outcomes longitudinally in pediatric mild TBI versus orthopedic injury. We recruited children between 8-16.99 years of age who presented within 48 hours of sustaining a mild TBI or orthopedic injury to the emergency department of five children's hospitals across Canada, of which all are members of the Pediatric Emergency Research Canada (PERC) network Bialy et al.; Keith Owen Yeates et al.: Alberta Children's Hospital (Calgary), Children's Hospital of Eastern Ontario (Ottawa), Centre Hospitalier Universitaire Sainte-Justine (Montreal), Stollery Children's Hospital (Edmonton), and British Columbia Children's Hospital (Vancouver).

Information about the acute clinical presentation and mechanism of injury, and a demographic questionnaire were collected at the post-acute follow-up (Keith Owen Yeates et al., 2017). Enrolled participants at each site returned for three additional follow-up assessments: a post-acute assessment (i.e., targeted for 10 days post-injury; range 2-33 days) and two chronic assessments, at 3 and 6 months post-injury. Overall study attrition rates were 15%, 25%, and 28% for the post-acute, 3-month, and 6-month assessments, respectively, similar to other studies of pediatric mild TBI (Keith Owen Yeates et al., 2017). All eligible participants (i.e., without MRI contraindication; see details below) completed 3T MRI at the post-acute assessment and were randomly assigned to complete a second MRI scan at 3 or 6 months post-injury.

The study was conducted with the approval of the research ethics board at each study site. All participants provided written informed assent and parents/guardians provided written informed consent.

3.2.2 Participants

3.2.2.1 Mild Traumatic Brain Injury

Children included in the mild TBI group sustained a blunt head trauma resulting in at least one of the following three criteria, consistent with the World Health Organization definition of mild TBI: i) observed loss of consciousness, ii) Glasgow Coma Scale score of 13-14, or iii) at least one acute sign or symptom of concussion as noted by emergency department medical personnel on a standard case report form, including post-traumatic amnesia, focal neurological deficits, vomiting, headache, dizziness, or other mental status changes (MTBI, 2004). Children were excluded if they demonstrated delayed neurological deterioration (e.g., Glasgow Coma Scale score < 13), required neurosurgical intervention, or had loss of consciousness > 30minutes or post-traumatic amnesia $>$ 24hours (Keith Owen Yeates et al., 2017).

3.2.2.2 Mild Orthopedic Injury

Children with mild orthopedic injury sustained an upper or lower extremity fracture, sprain, or strain due to blunt force trauma, associated with Abbreviated Injury Scale score ≤ 4 (i.e., "mild" severity; Committee on Injury Scaling, 1998) Children were excluded from the orthopedic injury group if they had head trauma, symptoms of concussion, or any injury requiring surgical intervention or procedural sedation (Keith Owen Yeates et al., 2017).

3.2.2.3 Exclusion Criteria

Both injury groups were subject to the following exclusion criteria: any other severe injury as defined by an Abbreviated Injury Scale score > 4; hypoxia, hypotension, or shock during or following the injury; previous concussion within 3 months prior or any prior TBI requiring hospital-

ization; premorbid neurological disorder or severe neurodevelopmental disability; injury resulting from non-accidental trauma; severe psychiatric disorder requiring hospitalization within the past year; or contraindications to MRI (e.g., metallic implants, orthodontia).

3.2.2.4 Symptoms

The Health and Behavior Inventory was used to assess cognitive and somatic symptoms. This measure has good internal consistency and test-retest reliability and has been adopted as a core measure in the Common Data Elements for Pediatric TBI (Adelson et al., 2012; McCauley et al., 2012; O'Brien et al., 2021). Total premorbid (pre-injury) symptoms were rated by parents during the post-acute visit, and total post-injury symptoms were rated by both parents and children weekly and also at each follow-up assessment (Ayr et al., 2009). A reliable change index (z-score) score comparing total 1-month post-injury symptom scores to premorbid scores was calculated using the following formulas based on regression analyses using data from the OI group for child ratings (O'Brien et al., 2021):

$$z = (post - injuryscore(3.44 + (0.50 * premorbidscore)))/6.89$$

and parent ratings:

$$z = (post - injuryscore(2.32 + (0.52 * premorbidscore)))/6.683$$

Results were used to classify children with mild TBI into two groups using a critical z-score >1.65 (one-tailed p <.05): (i) children with mild TBI and persistent symptoms (significant increase at 1-month post-injury relative to premorbid) and (ii) without persistent symptoms (no significant increase at 1-month post-injury relative to premorbid; Ledoux et al.,2019; Mayer, D. D. Stephenson, et al., 2020)

3.2.3 Magnetic Resonance Imaging

Eligible participants completed at least one 3T MRI scan without sedation that included T1-weighted and resting state functional MRI (rs-fMRI) sequences (Keith Owen Yeates et al., 2017). T1-weighted images were acquired with 0.8 mm isotropic resolution at all sites using FSPGR BRAVO sequences (General Electric: TR/TE/TI = 7.9, 8.25/3.6/600 ms, 4:47 min; Siemens: MPRAGE with TR/TE/TI = 1880, 2200/2.5, 2.9/948 ms, 5:28 min). Functional images were acquired using a single shot gradient echo planar imaging (EPI) sequence with a scan duration of 8 minutes and 10 seconds (TR = 2000ms, TE = 30ms, field of (FOV) = 23 cm, 36 slices, voxel dimensions = 3.6mm3). At all sites, children were asked to keep their eyes open, not think of anything in particular, and look at a cross presented on the screen. Foam padding was used to minimize head motion and headphones were used to minimize noise.

3.2.3.1 Quality Assurance

T1-weighted and resting state fMRI (rs-fMRI) DICOM data were converted into NIfTI format using the dcm2niix tool in MRIcron (https://github.com/rordenlab/dcm2niix).

Initial visual quality assurance of raw images was conducted for both image types to identify and exclude scans that demonstrated structural abnormalities at the time of the scan, scanner artifacts such as aliasing or warping, incomplete acquisition, reduced FOV (i.e., cropped), or were not collected using the default scan parameters.

3.2.3.2 Image Processing

Images were processed using a Nipype implementation of commands from the Advanced Normalization Tools (ANTs) v2.2.0, FMRIB's Software Library (FSL) v5.0.9, and Analysis of Functional Neuroimages (AFNI) v20160207. (Avants et al., 2008)(Tustison et al., 2010)]

3.2.3.2.1 T1-Weighted Images

The T1-weighted (T1w) images were corrected for intensity non-uniformity with N4BiasFieldCorrection (Nicholas J. Tustison et al., 2010), distributed with ANTs 2.2.0 (Avants et al., 2008), and used as T1w-reference. The T1w-reference was then skull-stripped with a Nipype implementation of the antsBrainExtraction.sh workflow (ANTs), using OASIS30ANTs as the target template. Volume-based spatial normalization to standard space was performed through nonlinear registration with antsRegistration (ANTs 2.2.0), using brain-extracted versions of both T1w reference and the T1w template. The MNI's unbiased standard MRI template for pediatric data (4.5 to 18.5 years age range; Fonov et al., 2011), was used for spatial normalization (TemplateFlow ID: MNIPediatricAsym: cohort-5).

3.2.3.2.2 Functional image preprocessing

To correct for susceptibility distortions, a deformation field that was estimated based on the fMRIprep fieldmap-less approach was used (Esteban et al., 2019) This approach applies a deformation field that was calculated during co-registration [implemented using ANTs (antsRegistration.sh) using constrained nonzero deformation along the phase encoding direction with modulation of the average fieldmap template (Treiber et al., 2016)] of each functional image to the reference T1-weighted image for each scan (Wang et al., 2017) Each functional image was co-registered to the T1-weighted image using FSL FLIRT (Jenkinson & Smith, 2001) with the boundary-based registration cost-function (Greve & Fischl, 2009). Nine degrees of freedom were used to configure the co-registration to account for any remaining distortions in the functional image. Functional images were then slice-time corrected using AFNI 3dTshift (Cox & Hyde, 1997).

Transformation matrices (i.e., six corresponding rotation and translation parameters associated with in-scanner head motion) were estimated for each functional image before spatiotemporal filtering using FSL MCFLIRT (Jenkinson et al., 2002). Framewise displacement was calculated in FSL

motion outliers (Theodore D. Satterthwaite et al., 2013; Jenkinson et al., 2002). Functional images were slice-time corrected using AFNI 3dTshift (Cox and Hyde, 1997). To minimize the smoothing effects of other kernels, each function image was warped in template space with a single interpolation step by composing all of the transformation parameters (i.e., transform matrices, susceptibility distortion correction, co-registrations to T1-weighted template space), using the Lanczos interpolation configuration (Lanczos, 1964) in ANTs antsApplyTransforms.

3.2.3.2.3 Denoising

Each functional run was denoised using AFNI's 3dTproject, accounting for the following regressors (see Ciric et al., 2017: (1) 6 motion parameters (3 rotations and translations in x y and z directions), (2) global, white matter and cerebrospinal fluid signal, (4) derivatives, squares and squared derivatives of each noise regressor, (5) framewise displacement motion spikes (see below), and (6) linear and polynomial trends. All regressors were detrended, by regressing out linear and polynomial trends. A whole-brain mask was generated and used to extract global signal. Next, to ensure that signals pertained to gray matter, white matter and cerebrospinal fluid signals were extracted from eroded segmentation masks (Power, Plitt, et al., 2017).

Head motion was estimated using the framewise displacement (FD) relative root mean squared (RMS; Jenkinson et al., 2002), which was calculated during time-series realignment using FSL MCFLIRT (Theodore D. Satterthwaite et al., 2013). Motion spikes were defined by as FD threshold $\geq$ 0.25 mm (Satterthwaite et al., 2013) and were included in the model as dummy variables (i.e., spike regression, as defined in Ciric et al., 2017). High-pass filtering at a threshold $\geq$ 0.01 Hz was applied in the same model to account for low frequencies. To preserve connectivity information at higher frequencies, no high-frequency threshold was applied for temporal filtering (Boubela et al., 2013; Chen Glover, 2015; Gohel Biswal, 2015; Lin et al., 2015; Niazy et al., 2011). This can improve the stability of

pairwise connections and maintain similar effects to bandpass filtering for motion mitigation (Graff et al., 2022). Scans were excluded for gross motion if they had an average FD RMS $\geq$ 0.20 mm or $\geq$ 60 (25%) volumes with FD RMS $\geq$ 0.25 mm (see Ciric et al., 2017).

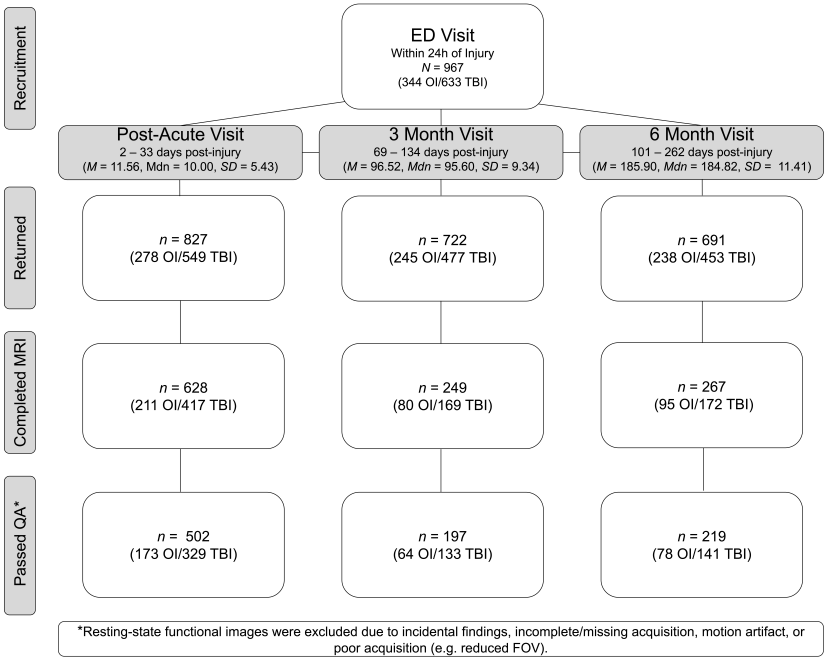

Figure 3.1: Summary data for the overall A-CAP study sample and the derivation of the current sample.

3.2.4 Network Construction

The 90 supratentorial region Automated Anatomical Label atlas (AAL-90; Tzourio-Mazoyer et al.,2002) was used to identify 90 nodes (brain regions). First, the AAL-90 atlas was co-registered to the pediatric template (antsregistration.sh, with multilabel interpolation). The labeled template was then

used to identify and extract the corresponding time series for each node from the denoised functional images. Significant signal dropout (>50% of the voxels) was demonstrated in the bilateral gyrus rectus (n scans = 154) and was therefore excluded from further analysis. Across the remaining 88 regions, significant signal dropout (> 50%) was demonstrated for 15 scans, which were excluded from subsequent analyses. The resulting 88 time series were then used to construct 88 x 88 weighted connectivity matrices using Pearson correlation.

To factor out the variability in network density across scans (Achard and Ed Bullmore, 2007; Wijk, C. J. Stam, and Daffertshofer, 2010) and improve the stability of graph theoretical measures (Garrison et al., 2015), a proportional threshold was applied to the weighted matrices. Percolation analysis was used to identify the threshold that removes the weakest connections while ensuring matrices are fully connected (Bordier, Nicolini, and Bifone, 2017; Nicolini et al., 2020). For this approach, multiple proportional thresholds (i.e., values that range between 0.01 and 1 at a step = 0.01) were applied recursively to identify the value at which the matrices become fragmented. Percolation analysis was used due to the lack of consensus in the literature for threshold definition, and to avoid network fragmentation across scans (Bordier, Nicolini, and Bifone, 2017). A proportional threshold of 0.25 preserved fully connected matrices in more than 98% of the scans. Scans from fragmented (not fully connected) adjacency matrices were excluded from the current analysis (n = 19).

3.2.4.1 Network Metrics

Graph theoretical metrics based on the absolute weighted connectivity matrix of each scan and 1,000 randomly generated networks were calculated in MATLAB using the GRaph thEoreTical Network Analysis (GRETNA) toolbox v.2.0 (J. Wang et al., 2015) and Brain Connectivity Toolbox (BCT; https://sites.google.com/site/bctnet/; Mikail Rubinov and Sporns, 2010). Global metrics included clustering coefficient, small-worldness, global efficiency, coreness (i.e., core-periphery organization), and modularity.

Nodal network metrics included clustering coefficient, local efficiency, betweenness centrality, and degree centrality (Rubinov & Sporns, 2010; J. Wang et al., 2015).

3.2.5 Multi-Scanner Harmonization

Prior to the final analysis, network metrics were harmonized for site (scanner) differences using ComBAT in RStudio v1.1.383 (R v4·0.3) (Fortin et al., 2017; R Core Team, 2017; RStudio Team, 2020). Group, time (days) post-injury, age at injury, and sex were included in the covariate matrix during harmonization, and model fitting was conducted with participant as a random effect. This approach is validated for network analysis (Onicas et al., 2022).

3.2.6 Statistical Analyses

Demographic data were analyzed using t-tests for continuous variables and 2 techniques for categorical variables.

The statistical approach is similar to that used to examine the diffusion MRI data for the A-CAP study (Ware et al., 2022). Multiple linear mixed-effects models were computed in RStudio (R Core Team, 2017; RStudio Team, 2020) using the lmerTest package to investigate the relations of group (TBI, OI), the linear and quadratic effects of time (days) post-injury, age at injury, sex, and group by time by age, group by time by sex, and their lower-order interactions on each harmonized network metric, controlling for the random effect of participant (Bates et al., 2015; Kuznetsova et al., 2017; Ware et al., 2022) Hemisphere did not moderate group differences in preliminary analyses. Therefore, only the main effect of hemisphere was included in each model. This approach was repeated to compare functional network metrics among symptom status groups (i.e., TBI with persistent symptoms, TBI without persistent symptoms) and OI. The final model is given by the following formulas for global and nodal metrics, respectively:

Global metric *Group * (T + T2) * (Age + Sex) + (1|P)*

or

Local metric *Group * (T + T2) * (Age + Sex) + Hemisphere + (1 | P)*

Where *T* is time and *P* is participant. To correct for multiple comparisons, the false discovery rate (FDR) was used at corrected P-thresholds $< .05$ for local (regional) metrics to account for 44 regions bilaterally (Benjamini Hochberg, 1995).

For follow-up analyses for all significant (i.e., survived correction for multiple comparisons) group effects or group-interaction terms, standardized effect size (i.e., Cohen's d) was assessed for group differences within the context of the final model for each network metric, with small, medium, and large effect size indicated by $|0.20| \leq$ d $< |0.50|$, $|0.50| \leq$ d $< |0.80|$, and d geq $|0.80|$ (Cohen, 1988).

Group differences within the respective context of the average days post-injury at each assessment for interactions with time post-injury, in male and female children for interactions with sex, and in younger (i.e., 10th percentile age at injury) and older (90th percentile age at injury) for interactions with age at injury (see supplemental Fig. 1). Only the effects with a d 95% confidence interval range that excluded 0 were considered to be robust and are described below. The BrainNet Viewer toolbox in MATLAB R2019a was used to display nodal level results (Xia et al., 2013).

3.3 Results

3.3.1 Sample

Information about the overall A-CAP study sample and the derivation of the current sample has been published (Ware et al., 2022) and is summarized in **Table 3.1**. Overall, of 3,075 eligible children, 967 consented to participate, and 846 returned for at least one assessment. The A-CAP study attrition rates were similar to other pediatric mild TBI studies (post-acute: 15%; 3 months: 25%; 6 months: 28%). A total of 671 children completed at least one MRI, for a total of 1144 completed scans. Orthodontia and scheduling difficulties were the most common reasons that MRI was not completed. Children who completed an MRI were slightly younger (M=12·23, SD=2·38 years; t=5.29, $p<.001$) and more often male (402 male/266 female; 2=6.22, p=.013), but were similar in terms of race and parental education relative to children who did not complete an MRI (M=13·29, SD=2·37 years; 88 male/90 female).

A total of 661 children completed rs-fMRI at least once, for a total of 1,130 scans. Of those, 261 (23%; 179 mild TBI/82 OI) scans were excluded after quality checks; 104 (9.2%; 72 mild TBI/32 OI) for gross motion; 46 (3.0%; 35 mild TBI/11 OI) for incomplete or wrong acquisition, 4 (0.3%; 1 mild TBI/3 OI) for structural abnormalities, 35 (3.0%; 23 mild TBI/12 OI) for scanner artifacts, 35 (3.0%; 23 mild TBI/12 OI) for poor registration, and 15 for signal dropout (1.3%, 10 mild TBI/5 OI). However, 13 scans were excluded for signal dropout in regions other than the gyrus rectus (1%; 9 TBI/4 OI) and 20 (2%; 12 mild TBI/8 OI) were excluded because the network topology was fragmented following thresholding. Thus, the final sample included 918 scans: 502 post-acute (n = 329 mild TBI), 197 longitudinal scans at 3 months (n = 133 mild TBI), and 219 (n = 141 TBI) at 6 months post-injury.

3.3.2 Sociodemographic and Injury Characteristics

The final sample of children with mild TBI did not differ from mild OI in terms of age at the time of injury, sex, parental education, race, average framewise displacement (i.e., motion), or whether the injury occurred during sport/recreation, but did differ in terms of injury mechanism (see **Table 3.1**). Detailed information on the efficiency of data harmonization is presented in **Figures B1–B5**. Children who returned at follow-ups did not differ significantly from those who did not return in terms of age, sex, race, or parental education, except that at 6 months, when the children who returned had higher parental education than those who did not return.

3.3.3 Global network metrics

Global network measures with injury and symptom group effects that survived correction for multiple comparisons are illustrated in **Figure 3.2** and statistical results are presented in **Tables 3.2 and 3.3**.

3.3.3.1 Injury groups

Differences in global clustering coefficient (Cp) between the injury groups were moderated by age at injury and time post-injury, whereby it was lower after mild TBI relative to OI 3 months post-injury in older children (**Figure 3.2, A** and **Table 3.2**).

3.3.3.2 Symptom groups

Time post-injury and sex moderated differences in global clustering coefficient among persistent symptom groups based on parent report (**Figure 3.2 B** and **Table 3.3**). In females, the clustering coefficient was lower in mild TBI with persistent symptoms at 3 months post-injury relative to OI. Global metrics did not differ among persistent symptom groups based on child report.

Table 3.1: Overall sample demographic and injury characteristics

Variable	**mild TBI** n = 386	**OI** n = 199	p *value*
Age [mean (SD)]	12.34 (2.41)	12.50 (2.17)	0.448
Site_MRI (%)			0.002
Calgary-GE	90 (23.3)	40 (20.1)	
Edmonton-Prisma	80 (20.7)	41 (20.6)	
Montreal-GE	23 (6.0)	5 (2.5)	
Montreal-Prisma	14 (3.6)	7 (3.5)	
Ottawa-Skyra	95 (24.6)	33 (16.6)	
Vancouver-GE	84 (21.8)	73 (36.7)	
Gender = Male (%)	240 (62.2)	111 (55.8)	0.159
Maternal education (%)			0.953
No certificate, diploma or degree	10 (2.8)	3 (1.6)	
High school diploma or equivalent	48 (13.3)	25 (13.7)	
Trades certificate or diploma	32 (8.9)	16 (8.8)	
2-year college diploma	70 (19.4)	39 (21.4)	
4-year bachelors degree	139 (38.6)	63 (34.6)	
Masters degree	43 (11.9)	26 (14.3)	
Doctoral degree (PhD or similar)	12 (3.3)	6 (3.3)	
Medical degree	6 (1.7)	4 (2.2)	
Race (%)			0.427
White	268 (69.4)	138 (69.3)	
Asian	30 (7.8)	12 (6.0)	
Black	16 (4.1)	6 (3.0)	
Latinx	8 (2.1)	7 (3.5)	
Indigenous	7 (1.8)	2 (1.0)	
Other/Mixed	51 (13.2)	26 (13.1)	
Unknown	6 (1.6)	8 (4.0)	
Mechanism of injury (%)			<.001
Fall	127 (43.9)	80 (48.5)	
Bicycle related	6 (2.1)	9 (5.5)	
Motor vehicle collision	3 (1.0)	0 (0.0)	
Struck object	85 (29.4)	33 (20.0)	
Struck person	58 (20.1)	20 (12.1)	
Other	4 (1.4)	12 (7.3)	
Unknown	6 (2.1)	11 (6.7)	
Sport-related injury (%)	248 (85.8)	136 (82.9)	0.493
FD [mean (SD)]	0.08 (0.04)	0.08 (0.04)	0.064

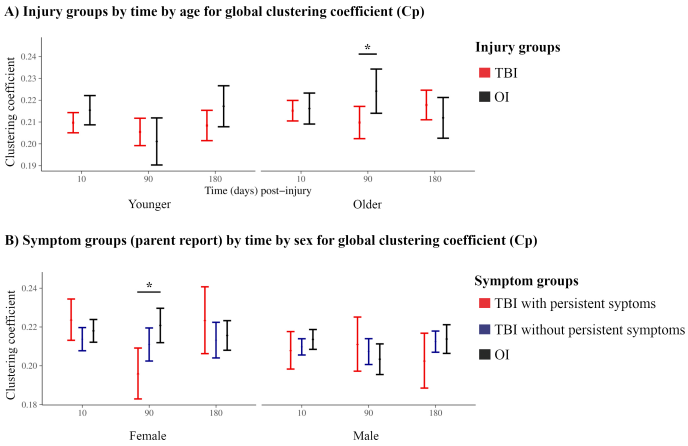

Figure 3.2: Differences in global network metrics between groups were moderated by time post-injury age at injury, and sex. Graphs illustrate the moderating effects of (A) time post-injury and age for global clustering coefficient between children with mild TBI and OI, and (B) time post-injury and biological sex for differences in global clustering coefficient among the symptom groups based on parent-reported symptoms at 1-month post-injury. Robust group differences (i.e., Cohen's d 95% confidence interval excluded 0) indicated with *.

3.3.4 Local network metrics

Local network results are reported in **Figures 3.3–3.6** (for statistical results see **Table 3.2** and **Table 3.3**).

3.3.4.1 Injury groups

Regional (nodal) network metrics with injury group effects that survived correction for multiple comparisons are illustrated in **Figure 3.3** (for statistical results see **Table 3.2**). Time post-injury moderated differences in degree centrality (Dc) of the superior occipital gyrus, nodal efficiency (Ne) of the superior parietal gyrus, and clustering coefficient (NCp) of the fusiform gyrus (**Figure 3.4, A**). These nodal metrics showed lower values among mild TBI participants compared to OI post-acutely (Dc of

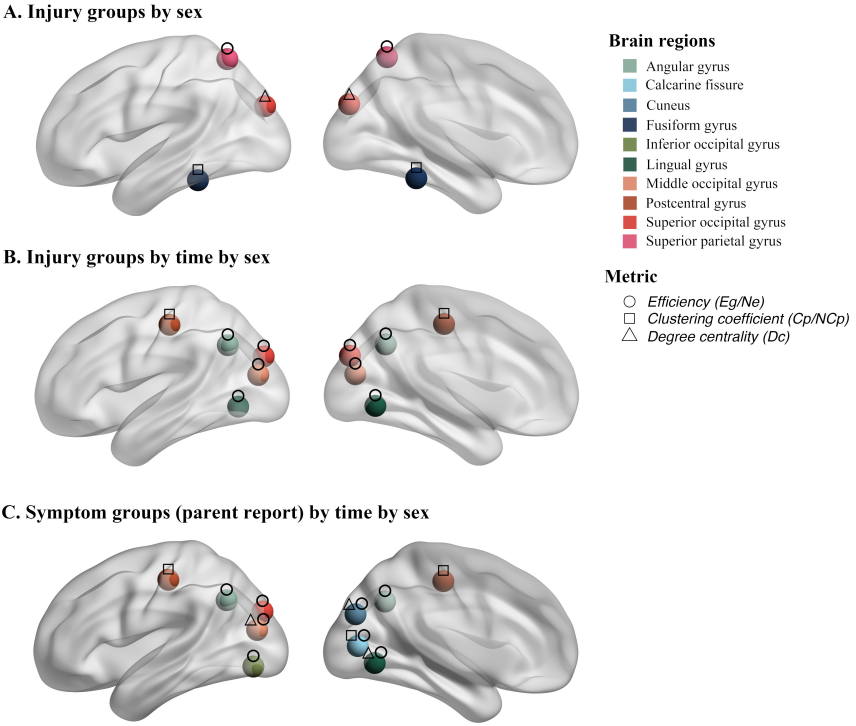

Figure 3.3: Differences in local network metrics between injury groups by sex (A), by time post-injury by sex (B), and between symptom groups (parent report) by time post-injury by sex (C).

the superior occipital gyrus), at 3 months post-injury (the NCp of the fusiform gyrus and nodal efficiency of the superior parietal gyrus).

Biological sex moderated group differences in nodal efficiency and clustering coefficient across time (**Figure 3.4, B**). In females, Ne of the superior occipital gyrus was lower after mild TBI relative to OI post-acutely, and the superior occipital, lingual, and angular gyri had lower efficiency at 3 months post-injury. Similarly, there was reduced clustering coefficient after mild TBI as compared with OI for the postcentral gyrus at 3 months post-injury. However, there was higher efficiency for the middle occipital gyrus at 6 months after mild TBI compared to OI. Among males, efficiency

was reduced for the lingual gyrus 6 months after mild TBI compared to OI.

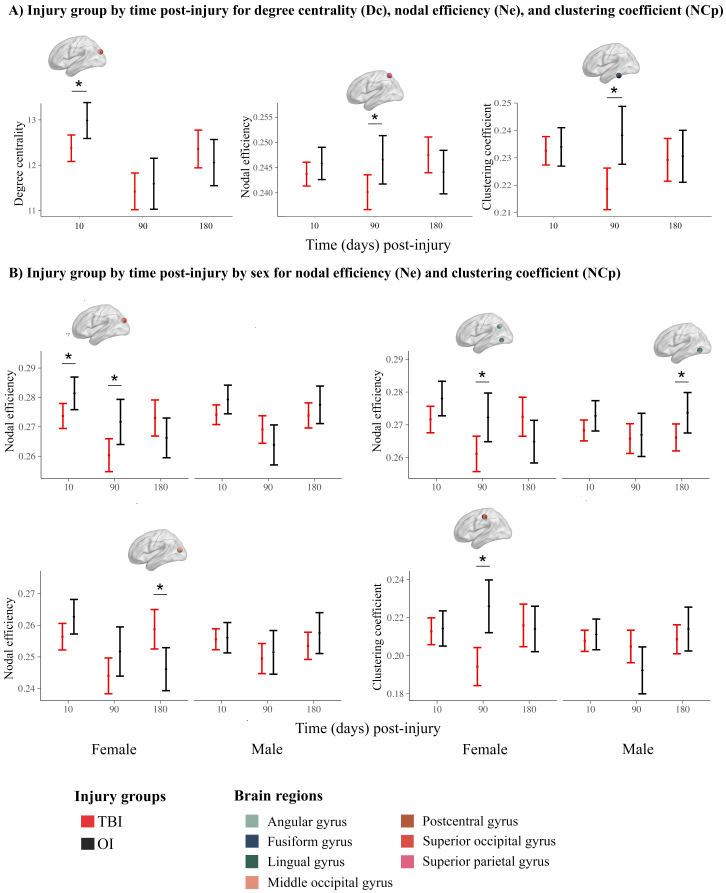

Figure 3.4: Differences in regional (nodal) graph metrics between the injury groups were moderated by time post-injury and biological sex. Graphs illustrate the moderating effects of (A) time post-injury for degree centrality (Dc), nodal efficiency (Ne), and clustering coefficient (NCp), and (B) time post-injury by sex for nodal efficiency (Ne) and clustering coefficient (NCp). Robust differences between the groups (i.e., Cohen's d 95% confidence interval excluded 0) are denoted by *.

Table 3.2: Follow-up pairwise comparisons for significant differences (FDR corrected $p < .05$) in global and regional (nodal) network metrics among injury groups.

Metric	*Region (node)*	*Time (dpi)*	*Age*	*Sex*	*Estimated Marginal Mean (95% CI)*		TBI - OI		
					TBI	*OI*	*Cohen's d*	*df*	*SE*
Clustering coefficient (NCp)									
	Whole brain (global)								
		10	Younger	–	0.210 (0.205, 0.214)	0.215 (0.209, 0.222)	-0.25 (-0.61, 0.11)	894,52	0,18
			Older	–	0.215 (0.210, 0.220)	0.216 (0.209, 0.223)	-0.04 (-0.42, 0.33)	888,81	0,19
		90	Younger	–	0.205 (0.199, 0.212)	0.201 (0.190, 0.212)	0.19 (-0.36, 0.74)	896,38	0,28
			Older	–	0.210 (0.202, 0.217)	0.224 (0.214, 0.234)	**-0.64 (-1.19, -0.08)***	899,14	0,28
		180	Younger	–	0.208 (0.201, 0.215)	0.217 (0.208, 0.227)	-0.39 (-0.91, 0.13)	894,67	0,26
			Older	–	0.218 (0.211, 0.225)	0.212 (0.203, 0.221)	0.26 (-0.25, 0.77)	893,1	0,26
	Fusiform gyrus								
		10	–	–	0.233 (0.227, 0.238)	0.234 (0.227, 0.241)	-0.03 (-0.19, 0.13)	1082,6	0,08
		90	–	–	0.219 (0.211, 0.226)	0.238 (0.228, 0.249)	**-0.36 (-0.60, -0.12)***	1373,57	0,12
		180	–	–	0.229 (0.221, 0.237)	0.231 (0.221, 0.240)	-0.02 (-0.25, 0.20)	1376,4	0,11
	Postcentral gyrus								
		10	–	Female	0.213 (0.206, 0.220)	0.214 (0.205, 0.224)	-0.03 (-0.28, 0.22)	1093,24	0,13
			–	Male	0.208 (0.202, 0.213)	0.211 (0.203, 0.219)	-0.07 (-0.28, 0.14)	1067,13	0,11
		90	–	**Female**	0.194 (0.184, 0.204)	0.226 (0.212, 0.240)	**-0.67 (-1.03, -0.31)***	1351,52	0,18
			–	Male	0.205 (0.196, 0.213)	0.192 (0.180, 0.205)	0.27 (-0.05, 0.58)	1385,99	0,16
		180	–	Female	0.216 (0.205, 0.227)	0.214 (0.202, 0.226)	0.04 (-0.31, 0.39)	1364,73	0,18
			–	Male	0.209 (0.201, 0.216)	0.214 (0.203, 0.226)	-0.11 (-0.41, 0.18)	1384,21	0,15
Degree centrality (Dc)									
	Superior occipital gyrus								
		10	–	–	12.379 (12.087, 12.672)	12.985 (12.589, 13.381)	**-0.25 (-0.45, -0.05)***	890,04	0,1
		90	–	–	11.424 (11.019, 11.830)	11.591 (11.028, 12.154)	-0.07 (-0.35, 0.22)	1433,74	0,14
		180	–	–	12.357 (11.941, 12.773)	12.057 (11.548, 12.566)	0.12 (-0.15, 0.39)	1373,8	0,14
Efficiency (Ne)									
	Superior parietal gyrus								
		10	–	–	0.244 (0.241, 0.246)	0.246 (0.243, 0.249)	-0.09 (-0.25, 0.08)	1058	0,08
		90	–	–	0.240 (0.237, 0.244)	0.247 (0.242, 0.251)	**-0.26 (-0.51, -0.02)***	1386,77	0,12
		180	–	–	0.248 (0.244, 0.251)	0.244 (0.240, 0.248)	0.14 (-0.09, 0.37)	1381,12	0,12
	Angular gyrus								
		10		Female	0.249 (0.245, 0.252)	0.248 (0.243, 0.252)	0.04 (-0.20, 0.29)	1075,77	0,13
				Male	0.240 (0.237, 0.243)	0.244 (0.240, 0.248)	-0.17 (-0.38, 0.04)	1050,21	0,11
		90		**Female**	0.244 (0.239, 0.249)	0.257 (0.250, 0.265)	**-0.57 (-0.93, -0.20)***	1359,93	0,19
				Male	0.242 (0.238, 0.247)	0.238 (0.231, 0.244)	0.18 (-0.14, 0.50)	1397,29	0,16

Table 3.2 continued from previous page

Metric	*Region (node)*	*Time (dpi)*	*Age*	*Sex*	*Estimated Marginal Mean (95% CI)*		*TBI - OI*		
					TBI	*OI*	*Cohen's d*	*df*	*SE*
		180		Female	0.252 (0.246, 0.258)	0.251 (0.245, 0.257)	0.05 (-0.30, 0.40)	1368,09	0,18
				Male	0.242 (0.238, 0.246)	0.239 (0.233, 0.245)	0.10 (-0.20, 0.39)	1387,63	0,15
	Lingual gyrus								
		10		Female	0.272 (0.268, 0.276)	0.278 (0.273, 0.283)	-0.31 (-0.63, 0.01)	879,52	0,16
				Male	0.268 (0.265, 0.271)	0.273 (0.268, 0.277)	-0.21 (-0.48, 0.06)	861,68	0,14
		90		**Female**	0.261 (0.256, 0.267)	0.272 (0.265, 0.280)	**-0.53 (-0.97, -0.09)***	1404,53	0,22
				Male	0.266 (0.261, 0.270)	0.267 (0.260, 0.274)	-0.05 (-0.44, 0.33)	1462,28	0,2
		180		Female	0.272 (0.267, 0.278)	0.265 (0.258, 0.271)	0.36 (-0.06, 0.79)	1359	0,22
				Male	0.266 (0.262, 0.270)	0.274 (0.268, 0.280)	**-0.36 (-0.72, -0.01)***	1369,18	0,18
	Middle occipital gyrus								
		10		Female	0.256 (0.252, 0.261)	0.263 (0.257, 0.268)	-0.28 (-0.59, 0.03)	900,73	0,16
				Male	0.256 (0.252, 0.259)	0.256 (0.251, 0.261)	-0.02 (-0.28, 0.24)	881,94	0,13
		90		Female	0.244 (0.238, 0.250)	0.252 (0.244, 0.259)	-0.34 (-0.77, 0.09)	1407,1	0,22
				Male	0.249 (0.245, 0.254)	0.251 (0.245, 0.258)	-0.09 (-0.46, 0.29)	1463,93	0,19
		180		**Female**	0.259 (0.252, 0.265)	0.246 (0.239, 0.253)	**0.56 (0.15, 0.98)***	1366,9	0,21
				Male	0.253 (0.249, 0.258)	0.258 (0.251, 0.264)	-0.18 (-0.53, 0.17)	1379,26	0,18
	Superior occipital gyrus								
		10		**Female**	0.274 (0.269, 0.278)	0.281 (0.276, 0.287)	**-0.37 (-0.71, -0.03)***	845,35	0,17
				Male	0.274 (0.271, 0.277)	0.279 (0.274, 0.284)	-0.25 (-0.54, 0.04)	829,1	0,15
		90		**Female**	0.260 (0.255, 0.266)	0.272 (0.264, 0.279)	**-0.55 (-1.00, -0.09)***	1393,71	0,23
				Male	0.269 (0.264, 0.274)	0.264 (0.257, 0.271)	0.25 (-0.15, 0.65)	1452,14	0,2
		180		Female	0.273 (0.267, 0.279)	0.266 (0.259, 0.273)	0.33 (-0.11, 0.77)	1340,04	0,22
				Male	0.274 (0.270, 0.278)	0.277 (0.271, 0.284)	-0.17 (-0.55, 0.20)	1346,03	0,19

3.3.4.2 Symptom groups

Regional metrics differed among symptom groups based on parent report over time (see **Figure 3.5** and **Figure 3.6**); statistical results are summarized in **Table 3.3**). No differences survived FDR correction based on the child report.

Time post-injury and biological sex moderated differences between symptom groups in Dc, NCp (**Figure 3.5**) and Ne (**Figure 3.6**). In females, Ne of the calcarine fissure, cuneus, lingual, and superior occipital gyri were lower in mild TBI without persistent symptoms relative to OI post-acutely (**Figure 3.6**). At 3 months post-injury, females with persistent symptoms following mild TBI showed lower Dc of the lingual gyrus (**Figure 3.5**), NCp of the postcentral gyrus and the calcarine fissure (**Figure 3.5**) and Ne of the angular gyrus, calcarine fissure, cuneus, inferior occipital gyrus, lingual gyrus, middle and superior occipital gyrus (**Figure 3.6**) relative to OI. Relative to mild TBI without persistent symptoms, those with persistent symptoms showed lower Dc of the cuneus and middle occipital gyrus (**Figure 3.5**), and Ne of the cuneus, lingual, middle, and inferior occipital gyrus (**Figure 3.6**) at 3 months post-injury. However, at 6 months post-injury, Dc of the lingual (**Figure 3.5**) and NCp and Ne of the calcarine fissure (**Figure 3.6**) were higher in mild TBI with persistent symptoms relative to OI .

Females without persistent symptoms also differed from OI, demonstrating lower NCp of the postcentral gyrus (**Figure 3.5**) and Ne of the angular gyrus (**Figure 3.6**) at 3 months post-injury. In contrast, they showed higher Dc (**Figure 3.5**) and Ne (**Figure 3.6**) of the middle occipital gyrus at 6 months post-injury. In males with persistent symptoms, Ne of the inferior occipital gyrus was higher at 3 months post-injury, but Ne of the cuneus and calcarine fissure was lower at 6 months post-injury, relative to OI (**Figure 3.6**). The Dc of the cuneus was also lower across males with persistent symptoms relative to OI and to those without persistent symptoms at 6 months post-injury (**Figure 3.5**).

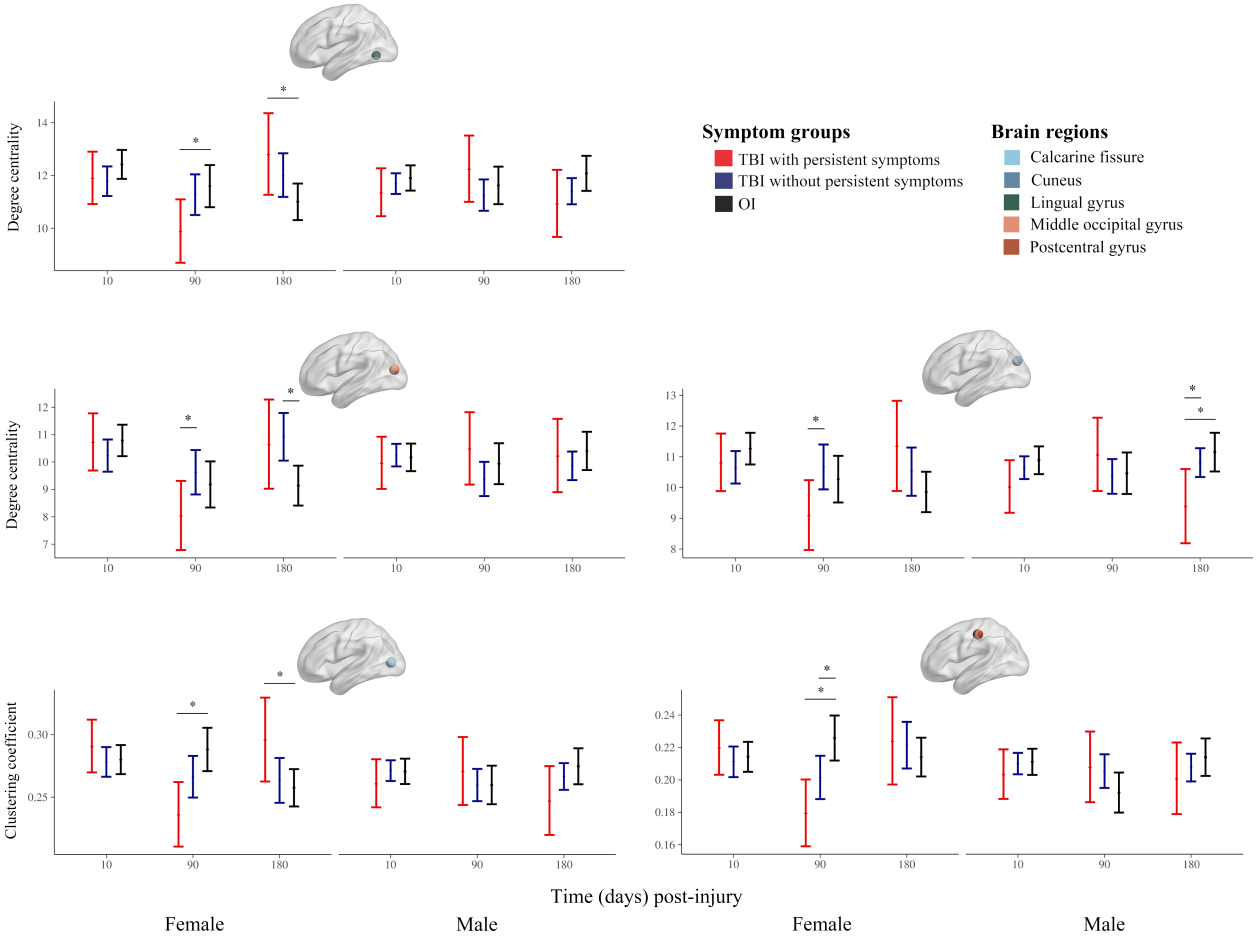

Figure 3.5: Differences in degree centrality and clustering coefficient among symptom groups based on parent report were moderated by time post-injury. Robust differences between the groups (i.e., Cohen's d 95% confidence interval excluded 0) are denoted by *.

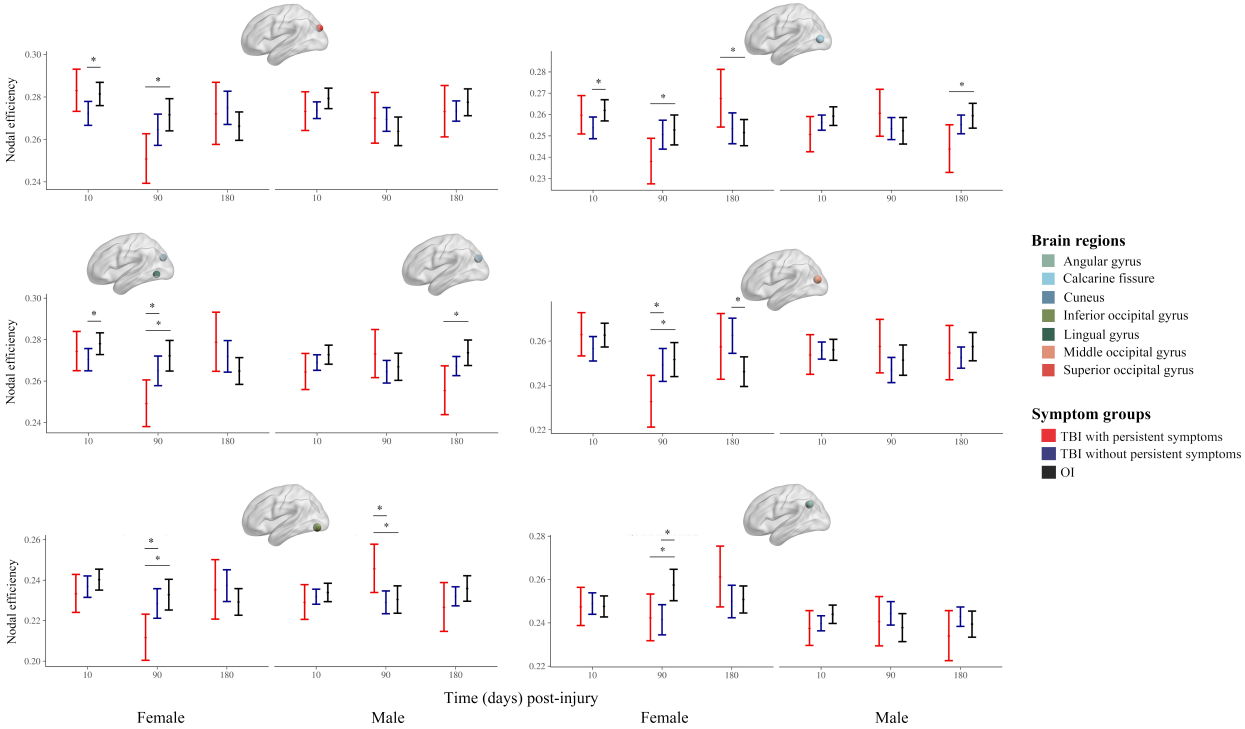

Figure 3.6: Differences in nodal efficiency among symptom groups based on parent report were moderated by time post-injury. Robust differences between the groups (i.e., Cohen's d 95% confidence interval excluded 0) are denoted by *.

Table 3.3: Follow-up pairwise comparisons for significant differences (FDR corrected $p < .05$) in global and regional (nodal) network metrics among injury groups.

Region (node)	*Time (dpi)*	*Sex*	*Estimated Marginal Mean (95% CI)*			*TBI with persistent symptoms minus TBI without persistent symptoms*			*TBI with persistent symptoms minus OI*			*TBI without persistent symptoms minus OI*		
			TBI with persistent symptoms	*TBI without persistent symptoms*	*OI*	*Cohen's d*	*df*	*SE*	*Cohen's d*	*df*	*SE*	*Cohen's d*	*df*	*SE*
Clustering coefficient (NCp)														
Whole brain (global)														
	10	Female	0.224 (0.213, 0.234)	0.214 (0.208, 0.220)	0.218 (0.212, 0.224)	0.44 (-0.09, 0.98)	779,46	0,27	0.26 (-0.28, 0.79)	780,26	0,27	-0.19 (-0.56, 0.18)	779,47	0,19
		Male	0.208 (0.198, 0.218)	0.210 (0.206, 0.214)	0.214 (0.208, 0.219)	-0.08 (-0.54, 0.39)	775,36	0,24	-0.25 (-0.73, 0.24)	774,96	0,25	-0.17 (-0.46, 0.12)	777,45	0,15
	90	**Female**	0.196 (0.183, 0.209)	0.211 (0.202, 0.220)	0.221 (0.212, 0.230)	-0.66 (-1.35, 0.03)	784,99	0,35	**-1.09 (-1.79, -0.39)***	785	0,36	-0.43 (-0.98, 0.11)	783,08	0,28
		Male	0.211 (0.197, 0.225)	0.207 (0.201, 0.214)	0.203 (0.196, 0.211)	0.17 (-0.51, 0.85)	781,71	0,35	0.34 (-0.36, 1.05)	783,12	0,36	0.17 (-0.28, 0.63)	781,38	0,23
	180	Female	0.223 (0.206, 0.241)	0.213 (0.204, 0.222)	0.216 (0.208, 0.223)	0.45 (-0.41, 1.32)	780,08	0,44	0.35 (-0.49, 1.18)	780,93	0,42	-0.11 (-0.63, 0.42)	781,29	0,27
		Male	0.203 (0.189, 0.217)	0.212 (0.207, 0.218)	0.214 (0.206, 0.221)	-0.43 (-1.10, 0.24)	780,55	0,34	-0.49 (-1.20, 0.21)	779,65	0,36	-0.06 (-0.46, 0.35)	780,55	0,21
Calcarine fissure														
	10	Female	0.291 (0.270, 0.312)	0.278 (0.266, 0.290)	0.280 (0.268, 0.292)	0.22 (-0.20, 0.64)	920,04	0,22	0.19 (-0.23, 0.61)	927,92	0,21	-0.03 (-0.32, 0.26)	906,11	0,15
		Male	0.261 (0.242, 0.280)	0.271 (0.263, 0.280)	0.271 (0.261, 0.281)	-0.18 (-0.54, 0.19)	889,28	0,19	-0.17 (-0.55, 0.21)	885,46	0,19	0.01 (-0.22, 0.24)	897,47	0,12
	90	**Female**	0.236 (0.211, 0.262)	0.266 (0.250, 0.283)	0.288 (0.271, 0.305)	-0.52 (-1.06, 0.01)	1106,13	0,27	**-0.91 (-1.45, -0.36)***	1115,59	0,28	-0.38 (-0.80, 0.04)	1201,51	0,21
		Male	0.271 (0.244, 0.298)	0.260 (0.247, 0.273)	0.260 (0.244, 0.275)	0.20 (-0.33, 0.72)	1226,71	0,27	0.19 (-0.35, 0.74)	1213,11	0,28	0.00 (-0.35, 0.35)	1244,92	0,18
	180	**Female**	0.296 (0.263, 0.330)	0.263 (0.246, 0.281)	0.258 (0.243, 0.272)	0.57 (-0.09, 1.23)	1236,57	0,34	**0.67 (0.03, 1.31)***	1221,3	0,33	0.10 (-0.30, 0.51)	1197,96	0,21
		Male	0.247 (0.220, 0.275)	0.267 (0.256, 0.277)	0.275 (0.260, 0.289)	-0.34 (-0.85, 0.18)	1214,17	0,26	-0.48 (-1.02, 0.06)	1225,22	0,28	-0.14 (-0.46, 0.17)	1200,73	0,16
Postcentral gyrus														
	10	Female	0.220 (0.203, 0.237)	0.211 (0.202, 0.221)	0.214 (0.205, 0.224)	0.18 (-0.22, 0.59)	954,44	0,21	0.12 (-0.28, 0.52)	961,92	0,21	-0.06 (-0.34, 0.21)	945,2	0,14
		Male	0.204 (0.188, 0.219)	0.210 (0.203, 0.217)	0.211 (0.203, 0.219)	-0.14 (-0.49, 0.21)	924,23	0,18	-0.16 (-0.52, 0.20)	920,84	0,19	-0.02 (-0.24, 0.20)	934,31	0,11
	90	**Female**	0.180 (0.159, 0.200)	0.202 (0.188, 0.215)	0.226 (0.212, 0.240)	-0.46 (-0.98, 0.06)	1105,38	0,26	**-0.97 (-1.50, -0.45)***	1111,92	0,27	**-0.51 (-0.92, -0.11)***	1186,97	0,21
		Male	0.208 (0.186, 0.230)	0.205 (0.195, 0.216)	0.192 (0.180, 0.205)	0.06 (-0.45, 0.56)	1209,99	0,26	0.33 (-0.19, 0.86)	1194,84	0,27	0.28 (-0.06, 0.62)	1222,22	0,17
	180	Female	0.224 (0.197, 0.251)	0.221 (0.207, 0.236)	0.214 (0.202, 0.226)	0.06 (-0.59, 0.70)	1220,4	0,33	0.21 (-0.41, 0.83)	1207,76	0,32	0.15 (-0.24, 0.55)	1192,4	0,2
		Male	0.201 (0.179, 0.223)	0.208 (0.199, 0.216)	0.214 (0.202, 0.226)	-0.14 (-0.64, 0.36)	1205,82	0,25	-0.27 (-0.80, 0.25)	1215,82	0,27	-0.13 (-0.44, 0.17)	1197,29	0,15
Degree centrality (Dc)														
Cuneus														
	10	Female	10.820 (9.884, 11.757)	10.659 (10.131, 11.187)	11.265 (10.749, 11.781)	0.07 (-0.38, 0.52)	873,52	0,23	-0.19 (-0.63, 0.26)	881,76	0,23	-0.25 (-0.56, 0.06)	854,45	0,16
		Male	10.034 (9.178, 10.890)	10.647 (10.278, 11.016)	10.888 (10.437, 11.340)	-0.26 (-0.65, 0.13)	842,79	0,2	-0.36 (-0.76, 0.05)	838,57	0,21	-0.10 (-0.34, 0.14)	848,55	0,12
	90	**Female**	9.105 (7.968, 10.241)	10.670 (9.939, 11.400)	10.272 (9.514, 11.031)	**-0.65 (-1.22, -0.09)***	1102,34	0,29	-0.49 (-1.06, 0.08)	1116,03	0,29	0.17 (-0.27, 0.61)	1216,02	0,22
		Male	11.080 (9.889, 12.272)	10.363 (9.798, 10.928)	10.466 (9.791, 11.141)	0.30 (-0.25, 0.85)	1242,17	0,28	0.26 (-0.32, 0.83)	1230,69	0,29	-0.04 (-0.41, 0.33)	1269,74	0,19
		Female	11.355 (9.886, 12.823)	10.515 (9.731, 11.299)	9.856 (9.200, 10.513)	0.35 (-0.34, 1.05)	1255,61	0,35	0.63 (-0.05, 1.30)	1236,89	0,34	0.28 (-0.15, 0.70)	1201,25	0,22
	180	**Male**	9.397 (8.190, 10.604)	10.811 (10.342, 11.281)	11.152 (10.521, 11.782)	**-0.59 (-1.13, -0.05)***	1220,01	0,28	**-0.73 (-1.30, -0.16)***	1232,43	0,29	-0.14 (-0.47, 0.19)	1200,12	0,17
Lingual gyrus														
		Female	11.910 (10.917, 12.904)	11.783 (11.222, 12.343)	12.420 (11.873, 12.967)	0.05 (-0.41, 0.51)	854,28	0,24	-0.21 (-0.67, 0.25)	862,6	0,23	-0.26 (-0.58, 0.06)	833,55	0,16

Table 3.3 continued from previous page

Region (node)	Time (dpi)	Sex	Estimated Marginal Mean (95% CI)			TBI with persistent symptoms minus TBI without persistent symptoms			TBI with persistent symptoms minus OI			TBI without persistent symptoms minus OI		
			TBI with persistent symptoms	TBI without persistent symptoms	OI	Cohen's d	df	SE	Cohen's d	df	SE	Cohen's d	df	SE
	10	Male	11.366 (10.457, 12.275)	11.691 (11.299, 12.083)	11.905 (11.426, 12.385)	-0.13 (-0.53, 0.27)	823,84	0,2	-0.22 (-0.63, 0.20)	819,53	0,21	-0.09 (-0.34, 0.16)	828,67	0,13
	90	**Female**	9.892 (8.690, 11.095)	11.271 (10.500, 12.042)	11.596 (10.797, 12.396)	-0.56 (-1.14, 0.02)	1098,74	0,29	**-0.69 (-1.27, -0.11)***	1114,25	0,3	-0.13 (-0.58, 0.32)	1219,72	0,23
		Male	12.257 (11.000, 13.513)	11.256 (10.662, 11.851)	11.625 (10.913, 12.336)	0.41 (-0.16, 0.97)	1245,52	0,29	0.26 (-0.33, 0.84)	1234,91	0,3	-0.15 (-0.52, 0.23)	1277,44	0,19
	180	**Female**	12.815 (11.268, 14.363)	12.014 (11.188, 12.840)	11.001 (10.307, 11.694)	0.32 (-0.39, 1.03)	1262,1	0,36	**0.73 (0.05, 1.42)***	1242,01	0,35	0.41 (-0.03, 0.85)	1200,68	0,22
		Male	10.942 (9.669, 12.215)	11.405 (10.910, 11.901)	12.082 (11.417, 12.746)	-0.19 (-0.74, 0.37)	1220,04	0,28	-0.46 (-1.04, 0.12)	1232,99	0,3	-0.27 (-0.61, 0.06)	1197,55	0,17
Middle occipital gyrus														
	10	Female	10.735 (9.692, 11.778)	10.234 (9.646, 10.822)	10.789 (10.214, 11.363)	0.19 (-0.27, 0.65)	860,51	0,23	-0.02 (-0.48, 0.43)	868,81	0,23	-0.21 (-0.53, 0.10)	840,29	0,16
		Male	9.970 (9.016, 10.924)	10.252 (9.841, 10.663)	10.170 (9.667, 10.674)	-0.11 (-0.50, 0.29)	829,96	0,2	-0.08 (-0.49, 0.34)	825,67	0,21	0.03 (-0.22, 0.28)	835,09	0,13
	90	**Female**	8.049 (6.786, 9.313)	9.627 (8.816, 10.437)	9.181 (8.340, 10.023)	**-0.60 (-1.18, -0.03)***	1100,06	0,29	-0.43 (-1.01, 0.15)	1114,97	0,3	0.17 (-0.28, 0.62)	1218,69	0,23
		Male	10.499 (9.178, 11.821)	9.381 (8.755, 10.007)	9.939 (9.191, 10.688)	0.43 (-0.13, 0.99)	1244,66	0,28	0.21 (-0.37, 0.79)	1233,76	0,3	-0.21 (-0.59, 0.16)	1275,13	0,19
	180	**Female**	10.653 (9.024, 12.281)	10.921 (10.052, 11.790)	9.140 (8.411, 9.869)	-0.10 (-0.81, 0.60)	1260,1	0,36	0.58 (-0.10, 1.26)	1240,45	0,35	**0.68 (0.25, 1.11)***	1201,01	0,22
		Male	10.237 (8.898, 11.576)	9.862 (9.341, 10.384)	10.406 (9.707, 11.105)	0.14 (-0.41, 0.69)	1220,2	0,28	-0.06 (-0.64, 0.51)	1232,99	0,29	-0.21 (-0.54, 0.13)	1198,56	0,17
Nodal efficiency (Ne)														
Angular gyrus														
	10	Female	0.248 (0.239, 0.256)	0.249 (0.244, 0.254)	0.248 (0.243, 0.252)	-0.05 (-0.47, 0.36)	928,18	0,21	0.00 (-0.42, 0.42)	935,97	0,21	0.05 (-0.23, 0.34)	915,29	0,15
		Male	0.238 (0.230, 0.246)	0.240 (0.236, 0.243)	0.244 (0.240, 0.248)	-0.09 (-0.45, 0.27)	897,51	0,18	-0.26 (-0.64, 0.11)	893,77	0,19	-0.17 (-0.40, 0.05)	906,13	0,12
	90	**Female**	0.243 (0.232, 0.253)	0.241 (0.234, 0.248)	0.257 (0.250, 0.265)	0.05 (-0.49, 0.58)	1106,19	0,27	**-0.62 (-1.16, -0.08)***	1114,94	0,27	**-0.66 (-1.08, -0.25)***	1198,32	0,21
		Male	0.241 (0.229, 0.252)	0.244 (0.239, 0.250)	0.238 (0.231, 0.244)	-0.15 (-0.67, 0.37)	1223,11	0,27	0.12 (-0.42, 0.66)	1209,13	0,28	0.27 (-0.08, 0.62)	1239,84	0,18
	180	Female	0.261 (0.247, 0.275)	0.250 (0.242, 0.257)	0.251 (0.245, 0.257)	0.48 (-0.18, 1.14)	1232,88	0,34	0.44 (-0.20, 1.08)	1218,21	0,32	-0.04 (-0.44, 0.37)	1196,84	0,21
		Male	0.234 (0.223, 0.246)	0.243 (0.238, 0.247)	0.239 (0.233, 0.245)	-0.36 (-0.87, 0.15)	1212,46	0,26	-0.22 (-0.76, 0.32)	1223,26	0,27	0.14 (-0.17, 0.45)	1200,17	0,16
Calcarine fissure														
	10	**Female**	0.260 (0.251, 0.269)	0.254 (0.249, 0.259)	0.262 (0.257, 0.267)	0.31 (-0.21, 0.84)	777,72	0,27	-0.11 (-0.63, 0.42)	785,92	0,27	**-0.42 (-0.78, -0.06)***	753,41	0,18
		Male	0.251 (0.243, 0.259)	0.256 (0.253, 0.260)	0.259 (0.255, 0.264)	-0.27 (-0.73, 0.18)	750,1	0,23	-0.43 (-0.90, 0.05)	745,8	0,24	-0.15 (-0.44, 0.13)	751,72	0,15
	90	**Female**	0.238 (0.227, 0.249)	0.251 (0.244, 0.257)	0.253 (0.246, 0.260)	-0.63 (-1.27, 0.01)	1068,3	0,33	**-0.74 (-1.39, -0.09)***	1091,14	0,33	-0.11 (-0.60, 0.38)	1215,17	0,25
		Male	0.261 (0.250, 0.272)	0.253 (0.248, 0.259)	0.252 (0.246, 0.259)	0.37 (-0.24, 0.99)	1235,02	0,31	0.43 (-0.21, 1.07)	1227,63	0,33	0.05 (-0.36, 0.46)	1286,93	0,21
	180	**Female**	0.268 (0.254, 0.281)	0.254 (0.246, 0.261)	0.252 (0.245, 0.258)	0.72 (-0.06, 1.49)	1275,17	0,4	**0.82 (0.07, 1.57)***	1249,95	0,38	0.10 (-0.38, 0.58)	1181,6	0,24
		Male	0.244 (0.233, 0.255)	0.255 (0.251, 0.260)	0.259 (0.254, 0.265)	-0.57 (-1.18, 0.03)	1200,52	0,31	**-0.78 (-1.42, -0.14)***	1215,24	0,33	-0.21 (-0.58, 0.16)	1168,06	0,19
Cuneus														
	10	**Female**	0.266 (0.257, 0.275)	0.262 (0.256, 0.267)	0.270 (0.265, 0.275)	0.21 (-0.30, 0.72)	794,17	0,26	-0.22 (-0.72, 0.29)	802,46	0,26	**-0.43 (-0.78, -0.08)***	770,21	0,18
		Male	0.256 (0.248, 0.265)	0.262 (0.259, 0.266)	0.266 (0.261, 0.270)	-0.29 (-0.73, 0.15)	765,72	0,23	-0.46 (-0.92, 0.00)	761,37	0,23	-0.17 (-0.44, 0.11)	767,96	0,14
	90	**Female**	0.243 (0.232, 0.254)	0.260 (0.253, 0.267)	0.263 (0.255, 0.270)	**-0.85 (-1.47, -0.22)***	1077,38	0,32	**-0.95 (-1.59, -0.32)***	1098,68	0,32	-0.11 (-0.59, 0.37)	1219,31	0,25
		Male	0.264 (0.253, 0.275)	0.258 (0.253, 0.263)	0.258 (0.252, 0.264)	0.29 (-0.31, 0.90)	1241,06	0,31	0.31 (-0.32, 0.94)	1233,01	0,32	0.02 (-0.39, 0.42)	1288,31	0,2
	180	Female	0.270 (0.256, 0.284)	0.262 (0.254, 0.269)	0.257 (0.251, 0.263)	0.40 (-0.36, 1.16)	1274,54	0,39	0.64 (-0.09, 1.38)	1250,38	0,38	0.24 (-0.23, 0.71)	1188,49	0,24
		Male	0.253 (0.241, 0.264)	0.264 (0.259, 0.268)	0.268 (0.262, 0.273)	-0.54 (-1.14, 0.05)	1207,89	0,3	**-0.73 (-1.35, -0.11)***	1222,3	0,32	-0.19 (-0.55, 0.17)	1177,51	0,18
Inferior occipital gyrus														

Table 3.3 continued from previous page

Region (node)	Time (dpi)	Sex	Estimated Marginal Mean (95% CI)			TBI with persistent symptoms minus TBI without persistent symptoms			TBI with persistent symptoms minus OI			TBI without persistent symptoms minus OI		
			TBI with persistent symptoms	TBI without persistent symptoms	OI	Cohen's d	df	SE	Cohen's d	df	SE	Cohen's d	df	SE
	10	Female	0.233 (0.224, 0.243)	0.237 (0.231, 0.242)	0.240 (0.235, 0.245)	-0.14 (-0.60, 0.31)	864,59	0,23	-0.29 (-0.74, 0.17)	872,88	0,23	-0.15 (-0.46, 0.17)	844,72	0,16
		Male	0.229 (0.221, 0.238)	0.232 (0.228, 0.236)	0.234 (0.229, 0.238)	-0.11 (-0.51, 0.28)	833,98	0,2	-0.20 (-0.61, 0.21)	829,71	0,21	-0.09 (-0.34, 0.16)	839,31	0,13
	90	**Female**	0.212 (0.200, 0.223)	0.228 (0.221, 0.236)	0.233 (0.225, 0.240)	**-0.70 (-1.27, -0.13)***	1100,84	0,29	**-0.89 (-1.46, -0.31)***	1115,37	0,29	-0.18 (-0.63, 0.26)	1217,93	0,23
		Male	0.246 (0.234, 0.258)	0.229 (0.223, 0.235)	0.230 (0.224, 0.237)	**0.71 (0.15, 1.26)***	1243,97	0,28	**0.65 (0.07, 1.23)***	1232,9	0,29	-0.06 (-0.43, 0.31)	1273,52	0,19
	180	Female	0.235 (0.221, 0.250)	0.237 (0.229, 0.245)	0.229 (0.223, 0.236)	-0.08 (-0.78, 0.62)	1258,74	0,36	0.26 (-0.42, 0.94)	1239,38	0,35	0.34 (-0.09, 0.77)	1201,15	0,22
		Male	0.227 (0.215, 0.239)	0.232 (0.227, 0.237)	0.236 (0.230, 0.242)	-0.22 (-0.77, 0.33)	1220,22	0,28	-0.39 (-0.96, 0.19)	1232,89	0,29	-0.16 (-0.50, 0.17)	1199,12	0,17
Lingual gyrus														
	10	**Female**	0.274 (0.265, 0.284)	0.270 (0.265, 0.276)	0.278 (0.273, 0.283)	0.20 (-0.32, 0.72)	779,73	0,27	-0.17 (-0.69, 0.35)	787,94	0,26	**-0.37 (-0.73, -0.01)***	755,44	0,18
		Male	0.265 (0.256, 0.273)	0.269 (0.265, 0.273)	0.273 (0.268, 0.277)	-0.21 (-0.66, 0.25)	751,99	0,23	-0.39 (-0.86, 0.08)	747,69	0,24	-0.18 (-0.47, 0.10)	753,69	0,14
	90	**Female**	0.249 (0.238, 0.261)	0.265 (0.258, 0.272)	0.272 (0.265, 0.280)	**-0.75 (-1.39, -0.11)***	1069,49	0,33	**-1.10 (-1.74, -0.45)***	1092,14	0,33	-0.35 (-0.84, 0.14)	1215,78	0,25
		Male	0.273 (0.262, 0.285)	0.265 (0.259, 0.270)	0.267 (0.260, 0.273)	0.42 (-0.19, 1.03)	1235,89	0,31	0.30 (-0.33, 0.94)	1228,42	0,33	-0.12 (-0.52, 0.29)	1287,22	0,21
	180	Female	0.279 (0.265, 0.293)	0.272 (0.264, 0.280)	0.265 (0.258, 0.271)	0.34 (-0.44, 1.11)	1275,17	0,39	0.67 (-0.08, 1.42)	1250,08	0,38	0.34 (-0.14, 0.82)	1182,54	0,24
		Male	0.263 (0.251, 0.275)	0.267 (0.263, 0.272)	0.274 (0.268, 0.280)	-0.19 (-0.80, 0.41)	1201,53	0,31	-0.50 (-1.14, 0.14)	1216,22	0,32	-0.31 (-0.68, 0.06)	1169,32	0,19
Middle occipital gyrus														
	10	Female	0.263 (0.253, 0.273)	0.257 (0.251, 0.262)	0.263 (0.257, 0.268)	0.29 (-0.21, 0.80)	801,03	0,26	0.02 (-0.48, 0.52)	809,34	0,25	-0.28 (-0.62, 0.07)	777,28	0,18
		Male	0.254 (0.245, 0.263)	0.256 (0.252, 0.260)	0.256 (0.251, 0.261)	-0.08 (-0.52, 0.36)	772,27	0,22	-0.09 (-0.55, 0.36)	767,9	0,23	-0.02 (-0.29, 0.26)	774,77	0,14
	90	**Female**	0.233 (0.221, 0.245)	0.249 (0.242, 0.257)	0.252 (0.244, 0.259)	**-0.73 (-1.35, -0.11)***	1080,71	0,32	**-0.84 (-1.47, -0.22)***	1101,36	0,32	-0.11 (-0.59, 0.37)	1220,45	0,24
		Male	0.258 (0.246, 0.270)	0.247 (0.241, 0.253)	0.251 (0.245, 0.258)	0.48 (-0.11, 1.08)	1242,9	0,31	0.28 (-0.34, 0.91)	1234,57	0,32	-0.20 (-0.60, 0.20)	1288,26	0,2
	180	**Female**	0.258 (0.243, 0.272)	0.262 (0.254, 0.270)	0.246 (0.239, 0.253)	-0.22 (-0.97, 0.54)	1273,87	0,38	0.51 (-0.22, 1.24)	1250,15	0,37	**0.73 (0.26, 1.19)***	1190,84	0,24
		Male	0.255 (0.243, 0.267)	0.253 (0.248, 0.257)	0.257 (0.251, 0.264)	0.10 (-0.49, 0.69)	1210,39	0,3	-0.12 (-0.74, 0.50)	1224,65	0,32	-0.22 (-0.58, 0.14)	1180,89	0,18
Superior occipital gyrus														
	10	**Female**	0.283 (0.273, 0.293)	0.272 (0.267, 0.278)	0.281 (0.276, 0.287)	0.53 (-0.02, 1.09)	747,22	0,28	0.08 (-0.47, 0.64)	755,14	0,28	**-0.45 (-0.83, -0.06)***	722,85	0,2
		Male	0.273 (0.264, 0.282)	0.274 (0.270, 0.278)	0.279 (0.275, 0.284)	-0.02 (-0.50, 0.46)	721,43	0,25	-0.29 (-0.79, 0.21)	717,31	0,26	-0.27 (-0.57, 0.03)	722,04	0,15
	90	**Female**	0.251 (0.239, 0.263)	0.265 (0.257, 0.272)	0.272 (0.264, 0.279)	-0.66 (-1.33, 0.01)	1046,89	0,34	**-1.00 (-1.68, -0.33)***	1072,42	0,35	-0.34 (-0.86, 0.17)	1201,56	0,26
		Male	0.270 (0.258, 0.282)	0.269 (0.264, 0.275)	0.264 (0.257, 0.271)	0.04 (-0.60, 0.68)	1216,98	0,33	0.31 (-0.36, 0.98)	1210,74	0,34	0.27 (-0.15, 0.70)	1277,94	0,22
	180	Female	0.272 (0.258, 0.287)	0.275 (0.267, 0.283)	0.266 (0.260, 0.273)	-0.13 (-0.94, 0.68)	1271,94	0,41	0.29 (-0.49, 1.08)	1244,85	0,4	0.42 (-0.08, 0.92)	1163,5	0,26
		Male	0.273 (0.261, 0.285)	0.273 (0.269, 0.278)	0.277 (0.271, 0.284)	0.00 (-0.64, 0.63)	1180,98	0,32	-0.21 (-0.87, 0.46)	1196,15	0,34	-0.20 (-0.59, 0.18)	1144,82	0,2

3.4 Discussion

This is the largest functional connectome study in children with mild TBI to date, and the first to longitudinally assess the effect of time post-injury on functional network alterations in the pediatric population. Changes in functional network topology occurred across injury and symptom groups, however, the differences were moderated by time post-injury, age, and biological sex. The current findings provide evidence of functional network abnormalities that tend to peak at 3 months post-injury, occur more often in females than in males, and among children with post-concussive symptoms at 1 month post-injury than in those without post-concussive symptoms. Differences in global network topology (i.e., clustering coefficient), emerged at 3 months and normalized by 6 months post-injury. However, nodal alterations emerged post-acutely, amplified/expanded at 3 months, and reduced at 6 months post-injury. This is the first study to address the heterogeneity of mild TBI in the pediatric population and take into account the variability associated with time post-injury, the presence of persistent post-concussive symptoms, biological sex, and age at injury.

The effect of group on global network metrics was moderated by time post-injury, age, and the presence of post-concussive symptoms. Specifically, the results are indicative of less segregated network topology, suggesting a decrease in local interactions between brain regions (Bullmore and Sporns, 2009) across older children with mild TBI and females with postconcussive symptoms at 3 months post-injury. Due to the lack of longitudinal studies, especially in pediatric mild TBI, comparisons with the existing literature are difficult. However, the absence of a main effect of group for global metrics is somewhat consistent with some previous reports. For example, a recent report assessed the functional connectome in a pediatric sample and showed no differences in transitivity (a measure of segregation similar to the clustering coefficient) and global efficiency among children with mild TBI at an average of 2.8 years after the injury (Botchway et al., 2022). Another study in adults with mild TBI showed no functional changes in global parameters at 19.6 days post-injury (Kim et al., 2022),

and the presence of persistent symptoms was not associated with changes in clustering coefficient postacutely (Hou et al., 2019). However, the mentioned reports include small sample sizes and are more heterogeneous in terms of time post-injury or injury severity.

Local differences were demonstrated postacutely and were more prominent across females following mild TBI. Degree centrality of the superior occipital cortex was the only metric to show an effect across both, males and females, and nodal efficiency of the same brain region had an effect in females following mild TBI, probably due to changes in the inferior fronto-occipital fasciculus previously reported in other studies of mild TBI (Liu et al., 2022; Jia et al., 2021). These post-acute differences did not predict persistent symptoms status at one-month post-injury, limiting the prognostic utility of graph-derived measures, probably due to higher variability in the persistent symptom group post-acutely. This variability could originate in differences across symptom dimensions (i.e., somatic, cognitive), pointing to the possible existence of different subgroups among children with persistent symptoms. In addition, this variability may relate to the limitations of self-report measurements. Specifically, the parent-based report may be subject to a biased perception of premorbid symptoms, which was demonstrated to affect the accuracy of estimating postconcussive symptom severity at one month post-injury (Brooks et al., 2014).

Local metrics showed differences across time, suggesting that localized network alterations tend to emerge earlier than global network alterations, and persist by 6 months post-injury. Local alterations among females with persistent symptoms were more distributed at 3 months post-injury and included parietal, temporal, and occipital regions. The presence of a more distributed pattern of differences among injury groups may explain the changes in the global segregation that occurred at 3 months post-injury. In addition, the reduction in local alterations from 3 to 6 months post-injury may explain the absence of longitudinal global alterations. Specifically, the presence of a more distributed pattern of functional communication across individual nodes likely influenced the overall network topology.

A higher number of brain regions differed across females with persistent symptoms and were prominent in the occipital cortex. Regional homogeneity abnormalities were reported in post-acute and chronic mild TBI in adults (Vedaei et al., 2021; Brooks et al., 2014). These could be related to changes in visual attention reported in TBI across severity levels (see Alnawmasi, Mani, and Khuu, 2022 for a meta-analysis) and/or eye movement and visual acuity (see Armstrong, 2018 for a review). In addition, structural studies of the A-CAP sample indicate that differences in cortical thickness and structural nodal graph topology show similar abnormalities across females with persistent symptoms (Ware et al., 2022; Ware et al., 2022, under review).

The current study has some limitations. Participants were recruited from emergency departments and may not be representative of individuals who do not seek medical attention (Setnik & Bazarian, 2007). The current sample generally included children from families of high socioeconomic status, thus the results may not be generalizable to the broader population. Although children with orthopedic injuries having any head trauma or signs or symptoms of concussion were excluded from this group, the possibility of occult or sub-concussive brain injury cannot be entirely ruled out (Barber Foss et al., 2019; McAllister et al., 2014; Sollmann et al., 2018). The persistent symptom status was assessed at a single time point, which does not account for changes in symptom status across time. Further studies may consider assessing specific symptom profiles (e.g., cognitive versus somatic symptoms) over time. Weighted adjacency matrices were based on the AAL atlas, and used absolute correlation values following a proportional threshold. Other studies may assess whether different methodological choices influence group differences (Hallquist & Hillary, 2018). Lastly, no main effects of injury group or persistent symptoms status were demonstrated, however, multivariate analyses combining different graph theoretical features in the same model may be used to evaluate whether between-group differences emerge in a more distributed manner following concussion. Specifically, combining information across brain regions and graph metrics may uncover clinically

relevant information to distinguish the effect of injury type, for example by addressing the possibility that brain regions are affected differently in distinct participants from the same group.

Chapter 4

Mapping event-related fMRI time series into graphs

Identification of signal changes in time series is critical for decoding fMRI task-evoked brain activity. The applicability of task fMRI data analysis has often been limited to linear modeling, usually by applying a convolution with an HRF. However, this assumes the uniformity of the HRF shape across time, whereas the BOLD response demonstrates considerable variability. Visibility graphs are a method that converts time series to graphs and allows using tools of complex systems for time series analysis. This transformation remains immune to differences in signal amplitude and linear trends and was shown to conserve properties of time series. However, it is not clear whether the topology of the temporal networks incorporates stimulus-evoked changes in the BOLD signal. To address this issue, synthetic event-related fMRI time series with varying levels of noise were simulated. Following VG transformation, time points corresponding to task events were expected to demonstrate increased degree centrality, and improved task detection based on the VG degree sequence as compared with the time series prior to VG transformation. An accuracy measure for task activity identification was defined based on the

overlap between the highest degree nodes and the expected timing of the hemodynamic response peak. The same measure was derived based on the intensity of the untransformed time series. The visibility graph degree demonstrated increased task event detection accuracy compared to the raw fMRI signal intensity, lower noise correlations, and improved signal-to-noise ratio compared to the untransformed time series. The results were replicated using a slow, event-related picture presentation dataset, with extensive scanning of four participants. Specifically, the time series extracted from V1 showed increased task-detection accuracy and lower correlations with in-scanner motion. A living minus non-living stimulus contrast showed consistent event detection accuracy of the ventral visual pathway across the four participants. Visibility graph topology conserves BOLD changes associated with task events, supporting their applicability for non-linear analysis of fMRI time series. The possibility to detect events without the use of explicit basis functions has implications for the fMRI analysis and may provide a valuable resource for modeling brain activity.

4.1 Introduction

Functional Magnetic Resonance Imaging (fMRI) is a well-established non-invasive neuroimaging modality for measuring the variability of oxygen delivery and blood flow in the gray matter based on changes in blood oxygenation-level dependent (BOLD) signal (Ogawa et al., 1992; Glover, 2011; Huettel, 2012; K. J. Friston, Fletcher, et al., 1998; Dale, 1999; Huettel, 2012). Task-fMRI is a technique that can elicit localized BOLD signal changes in response to task events (Song et al., 2002; Lee et al., 2010; Bowman, 2014), which are interpreted as evidence of neural activity (Ogawa et al., 1992; Gauthier and A. P. Fan, 2019; Logothetis and Wandell, 2004; Hillman, 2014). Typically, task fMRI modeling relies on the parametric mapping of the time series following the occurrence of individual task events, known as the General Linear Model (GLM; Karl Friston et al.,1994;K. J. Friston, Holmes, et al.,1995;Worsley and K. J. Friston,1995). Task evoked BOLD signal intensity changes between 2-5 % (G. Chen et al., 2015; Bowman, 2014) tend to peak between 4-6 seconds after stimulus onset and are followed by a signal intensity drop (Handwerker, Ollinger, and D'Esposito, 2004; Henson et al., 2002). GLM relies on fitting a Hemodynamic Response Function (HRF) around the occurrence of each event by finding model parameters (β) that minimize the least square distance between the time-series and the expected basis function (Pernet, 2014; K. J. Friston, Fletcher, et al., 1998; Rosen, Buckner, and Dale, 1998).

The GLM framework makes strong assumptions about signal and noise variability in fMRI time series (M. M. Monti, 2011; C. J. Long et al., 2005). Task-correlated changes in the BOLD signal are modeled uniformly and invariably based on a data-independent basis function that follows the shape of the canonical HRF (Liao et al., 2002; Pedregosa et al., 2015). HRF variability can manifest in the latency, shape, width or magnitude of the signal and can originate in multiple sources, including inter-individual differences, brain areas, or scanning parameters (Cignetti et al., 2016; Duann et al., 2002; Handwerker, Ollinger, and D'Esposito, 2004; Pedregosa

et al., 2015; Steffener et al., 2010; Lin et al., 2018). The recognition of this problem led to increasingly complex modeling approaches, for example by applying a mixture of basis functions (i.e., a basis set) to the fMRI signal (Cignetti et al., 2016; Rosa, Figueiredo, and Silvestre, 2015; Steffener et al., 2010), although capturing the variability of HRF response remains challenging (Lindquist et al., 2009). GLM modeling shows poor test-retest reliability for task fMRI data analysis, which limits its applicability for accurate subject and group-level inferences (M. L. Elliott et al., 2020; M. M. Monti, 2011).

While linear models are typically used for fMRI time series analysis, non-linear techniques can help better capture more complex features that characterize temporal signal changes, which could overcome the variability in BOLD responses during task fMRI. Complex network approaches are promising for the analysis of dynamical systems based on time-series (Zou et al., 2019), because they are able to extract topological information from time series, by constructing temporal graphs (i.e., time points become nodes) based on the pattern of signal intensity changes over time. A temporal network can be mapped using the Visibility Graph algorithm (VG; (Lacasa, Luque, et al., 2008; Lacasa, Nicosia, and Latora, 2015)), where relationships between pairs of time points is established based on a geometric condition given by signal intensity. The topology of VG temporal networks constructed is insensitive to linear transformations and conserves properties of the original time series: periodic time series are converted in regular graphs, random series results in random graphs, and fractal series are converted in scale-free networks (Lacasa, Nicosia, and Latora, 2015).

VG transformation has recently found applications in time series analysis across fields of science, including functional neuroimaging (Silva et al., 2021; Zou et al., 2019). Some reports applied visibility graph transformation on signals derived from electroencephalography (EEG) and fMRI. EEG studies highlighted the utility of VG for mapping large-scale functional connectivity (Ahmadlou, Ahmadi, et al., 2013; Yu, Hillebrand, et al., 2017), machine learning-based detection of epileptic seizures (L. Wang

et al., 2017; Mohammadpoory, Nasrolahzadeh, and Haddadnia, 2017) or classification of sleep stages (G. Zhu, Y. Li, and Wen, 2014; Cai, An, and Gao, 2020) and Alzheimer's disease (Ahmadlou, H. Adeli, and A. Adeli, 2010). Two fMRI studies used the similarity between regional time series based on VG topology. Sannino et al. (2017) assessed the pairwise similarity in the modular structure of the visibility graphs across regional time series, demonstrating differences between patients suffering from psychiatric disorders and healthy controls across regions of the limbic system. Another study (Gao et al., 2022) successfully classified Alzheimer's disease using topological features derived from regional time series and found abnormal connectivity based on the similarity between pairwise VG degree sequences across patients. Hasson et al. (2018) further found that local dynamics of VG degree can identify regional differences between N2 sleep stage and wakefulness in fMRI time-series. Interestingly, they found the top and bottom degree distribution asymmetry, rather than the propensity of localized extreme events, was informative for differentiating sleep stages during resting-state. This suggests that both, high and low degree nodes (time points) could derive informative signal features from fMRI time series during rest.

However, no study has evaluated whether individual task events can be identified based on time series network topology following VG mapping. Testing if VG can recover task activity from fMRI time series can provide a basis for their application in functional neuroimaging and extend the possibilities for task fMRI data analysis. For example, the conversion of fMRI time series into visibility graphs can allow for the use of network science methods for characterizing functional brain responses and can generalize the use of more advanced methods for statistical learning based on graphs. In addition, the adoption of more naturalistic paradigms, including continuous stimulation tasks such as narrative listening or movie watching motivates the development of methods that can be applied in the absence of information about event onsets. Whereas differences in the VG degree distribution may recover relevant signal features for the modeling of resting-state fMRI time-series in sleep and wakefulness (Hasson et al.,

2018), local maxima could be informative for identifying event-related hemodynamic activity. Specifically, localized extreme events may occur in the VG sequence following task event onset, exhibiting higher degree centrality corresponding to hemodynamic signal peaks. To address this question, the current study aims at caracterizing the role of VG degree sequence using synthetically generated and real fMRI data collected during an picture presentation task.

4.2 Methods

4.2.1 Datasets

Two datasets have been used for the purposes of this study. The first dataset was generated synthetically to resemble task fMRI data with varying levels of noise. The second dataset contains comprehensive scanning of four participants during a picture presentation event-related task, allowing for the evaluation of the within-participant consistency of our results.

4.2.1.1 Synthetic event-related data

To test whether VG can identify task events in time series data, we first generated synthetic event-related data that resembles the repetitive occurrences of an HRF with varying degrees of normally distributed noise (see **Figure 4.1**, A). Specifically, 99 HRFs were generated over 4,000 time points using the gampdf function in Matlab 2018b. Each HRF peaks at 6 time points and gradually decreases over a duration of 20 time points, with another 20 time points break between each occurrence.

Normally distributed noise of 4,000 time points duration was generated using the randn function. The noise time series was multiplied with values between 0.1 and 1, with a step of 0.01, in order to obtain TS with different levels of ”spikiness”. Finally, the simulated BOLD fMRI signal

was calculated as the sum between the HRF TS and each noise TS. This resulted in 36 discrete time series containing varying levels of noise. The procedure for generating synthetic fMRI TS was repeated 1,000 times to increase the generality of the observations.

4.2.1.2 BOLD5000 dataset

An openly available event-related BOLD fMRI dataset was used in order to generalize the results to real data. The BOLD5000 dataset was collected during a slow event-related task consisting of the presentation of visual stimuli (https://bold5000.org; N. Chang et al., 2019) and included a high dimensional anatomical scanning session and 15 functional scanning sessions from 3 participants (CSI1 - male, age 27; CSI2 - female, age 26; CSI3 - female, age 24; all right-handed). An additional participant underwent one anatomical and 9 functional scanning sessions (CSI4 - female, age 25; right-handed).

Each functional session consisted of either 8 or 10 runs of 37 slow event-related image presentation trials. In total, the dataset contains 510 runs: 142 runs were collected for participants CSI1, CSI2, and CSI3, and 84 runs for participant CSI4 respectively. The stimuli were drawn from three image databases: the Common Objects in Context (COCO, n = 2,000 stimuli), ImageNet (n = 1,916 stimuli), and Scene UNderstanding (SUN, n = 1,000 stimuli). Each stimulus was presented for 1 second, followed by a 9 seconds fixation cross.

4.2.1.2.1 Data acquisition

Detailed information about data acquisition is available in the dataset description paper (N. Chang et al., 2019). Data were acquired using a 3T Siemens Verio MR scanner. Functional images were collected using a T2*-weighted gradient recalled echoplanar imaging multi-band pulse sequence with the following scanning parameters: 69 slices co-planar with the AC/PC; in-plane resolution=2×2mm; 106×106 matrix size; 2mm

slice thickness, no gap; interleaved acquisition; field of view=212mm; phase partial Fourier scheme of 6/8; TR=2000 ms; TE=30ms; flip angle=79 degrees; multi-band factor=3; phase encoding direction=PA. The T1 MPRAGE scan was collected using the following parameters: 176 sagittal slices; 1mm isovoxel resolution; field of view=256mm; TR=2300ms; TE=1.97ms; TI=900ms: flip angle=9 degrees; GRAPPA acceleration factor=2; bandwidth=240Hz/Px.

4.2.1.2.2 Data preprocessing

Data preprocessing was performed using fMRIPrep 1.1.428 https://github.com/poldracklab/fmriprep; Esteban et al.,2019). Each T1w (T1-weighted) volume was corrected for intensity non-uniformity (INU) using N4BiasField Correction v2.1.030 and skull-stripped using antsBrainExtraction.sh v2.1.0 (using the OASIS template). Spatial normalization to the ICBM 152 Nonlinear Asymmetrical template version 2009c (Fonov et al., 2009) was performed through nonlinear registration with the antsRegistration tool of ANTs v2.1.034, using brain-extracted versions of both T1w volume and template. Brain tissue segmentation of cerebrospinal fluid (CSF), white matter (WM), and gray matter (GM) were performed on the brain-extracted T1w using fast35 (FSL v5.0.9). Functional data were motion corrected using mcflirt (FSL v5.0.936) and distortion corrected using 3dQwarp (AFNI v16.2.0737). This was followed by co-registration to the corresponding T1w using boundary-based registration (Greve and Fischl, 2009) with 9 degrees of freedom, using bbregister (FreeSurfer v6.0.1). Transformations from the motion correction, the field distortion correction warp and BOLD-to-T1w were concatenated and applied in a single step using antsApplyTransforms (ANTs v2.1.0) and Lanczos interpolation.

4.2.1.2.3 Denoising

Noise regression included 6 motion parameters, their derivatives, and spike regression of frame-to-frame displacement > 0.25 was performed with AFNI's 3dTproject. Time series were extracted from each denoised

functional image in the subject space using a bilateral V1 mask derived from Juelich probabilistic atlas at a 75 % threshold. The V1 mask was intersected with the segmentation-based binary gray matter masks of each participant (generated by thresholding the probabilistic masks at ¿75 %) and with the functional masks from each run. This was done prior to data extraction to reduce the probability of including non-gray matter signals. The overlap between the masks and each participant's T1w was visually checked. Average time series from each run were further extracted from bilateral V1 masks and imported in Matlab for VG construction and statistical analyses.

4.2.2 Visibility graph construction

Natural visibility graphs were constructed on each synthetic time series as described in Lacasa et. al (2008), using the visibility MATLAB function available on Github (https://github.com/danielemarinazzo/Visibility_LA5C_data). The natural visibility graph algorithm establishes a connection between node (time-point) i and j depending on the "height" of node k that lies between them, which is given by the condition:

$$y_k < y_i + (y_j - y_i)\frac{k-i}{j-i}$$

Thus, a connection between time points i and j is established if the time-point k has lower intensity relative to its neighbors, allowing to draw an imaginary line between i and j without passing through k. If time point k has high intensity relative to i and j, the connection is not established, node k thus blocking the visibility between nodes i and j. The adjacency matrices generated by the natural visibility algorithm are binary and undirected (symmetric).

VG degree sequence has been obtained by building the graphs over each time series (i.e., scanning run). The node degree sequence of a time series describes the VG degree adjacent to each time point (see **Figure 4.1**, B).

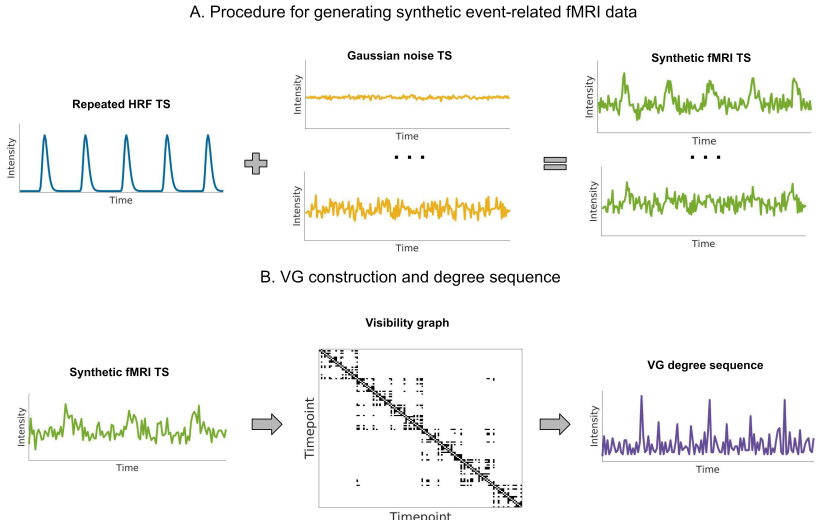

Figure 4.1: Procedure for generating synthetic fMRI signal (A) and Visibility Graph construction (B). The synthetic signal (A, right) was generated as the sum between a repeated HRF time series (A, left) and varying levels of noise (A, middle). The visibility graph algorithm was applied on each synthetic time series (B, left), resulting in a binary, symmetric, and fully connected network (B, middle). The Visibility Graph degree sequence is calculated as the degree of each node (time point) of the network (B, right). Please note that the degree sequence emphasizes the node peak, rather than a gradual HRF.

4.2.3 Data analysis

4.2.3.1 Accuracy estimation

4.2.3.1.1 Synthetic data

An accuracy measure was defined in order to establish the sensitivity of VG in identifying signal peaks following the onset of task events. We estimated the accuracy to define the extent to which high-intensity time points could be identified following stimulus presentation (and not somewhere else in the time series) by: (1) ordering the two time series

(VG degree sequence and fMRI time series) from the highest to the lowest (see **Figure 2, A**), and (2) calculating the percentage of cases in which the highest intensity time points (n = 99, with is given by the number of stimulus presentations) occurred at around 6 ± 3 time points after the corresponding stimulus onset, out of the total number of simulated stimulus presentations. The accuracy values indicate the proportion of high-degree nodes occurring within the windows search where signal peaks are expected to occur following stimulus presentation. Higher accuracy thus reflects a higher probability of spikes occurring around the expected HRF peaks, rather than somewhere else in the time series. This indicates that high signal intensities (in the raw fMRI time series) or high degree nodes (in the VG degree sequence) tend to appear following the occurrence of stimulus presentation. Accuracy values were obtained for each noise level (n=36) across 1,000 iterations of generating synthetic signal.

The significance of the differences between accuracy values corresponding to the two time series (VG degree sequence versus raw synthetic signal) was established using a permutation procedure. The 1,000 accuracy values obtained from the two time series (VG degree and the original signal) were permuted 10,000 times by shifting the label of the time series. The null distribution represents the shuffled accuracy levels (i.e., when the label of VG degree or raw synthetic time series are being permuted). We calculated the extent to which the real difference between accuracy values when using VG degree versus the original signal deviates from the non-parametric null distribution. This was done by counting the number of times a value of the null distribution is more extreme (i.e., either higher or lower) than the real difference in accuracy, out of the total number of permutations. This allows for a non-parametric definition of a p-value for each level of noise.

4.2.3.1.2 BOLD5000 dataset

After V1 time series extraction (described in the previous subsection),

the accuracy values were calculated similarly to the synthetic data, for each scanning run across sessions and across participants. Because the data was collected with a repetition time (TR) of 2 seconds, we calculated the expected HRF as the onset + 3 TR (6 seconds). As described for the synthetic data, we ordered the time points from the denoised signal before and after constructing VG and saved the indices of the 37 highest values (i.e, 37 is the number of known task onsets per run, which are expected to show high node degree). The number of times a high-intensity time-point was adjacent to the corresponding signal peak was counted by searching inside a 3 TR window, defined by the TR corresponding to the expected HRF peak +/- 1 TR. This procedure preserves a distance of 3 TR between windows. The comparison between VG transformation and original signals' accuracy was performed at the participant level.

4.2.3.2 Noise assessment

4.2.3.2.1 Synthetic data

We estimated the influence of noise based on the original signal and the VG degree sequence by computing the correlation between the noise alone (i.e., before combining it with the repeated HRF) and the synthetic fMRI time series before and after the VG transformation. The Kendall correlation between the synthetic fMRI signal and gaussian noise was used as a proxy for assessing the influence of noise versus signal (i.e., the repeated occurence of the HRF). Replicating this procedure for VG degree sequence allows to compare the influence of noise in the original synthetic fMRI time series versus following VG transformation. Here, we used Kendall correlation to (1) account for the differences in the two distributions via non-parametric testing and (2) obtain an estimate that is similar to the interpretation of accuracy, thus making it more comparable. Kendall correlation uses signal intensity directly, rather than the variance as is the case with other non-parametric alternatives such as Spearman correlation.

An estimate of signal-to-noise ratio (SNR) was obtained by calculating

the difference between accuracy and absolute noise correlations for each of the time series, across noise levels, and across the 1,000 iterations. This difference was obtained because, both the accuracy as well as the absolute correlation vary in a range of 0 to 1, therefore subtracting the two should provide information about how the influence of signal (i.e., accuracy) compares to the influence of noise (i.e., via noise correlation).

4.2.3.2.2 BOLD5000 dataset

Because real fMRI data do not provide complete control over signal and noise variability as is the case with the synthetic time series, we estimated the influence of noise by counting the number of significant correlations between each time series (original vs VG) and the corresponding FD across all sessions and runs. We used FD for the noise correlation analysis because it is a well-recognized and measurable source of bias in the fMRI data (Power, Barnes, Snyder, Schlaggar, Petersen, 2012; Power et al., 2014). A higher number of significant correlations between the two was considered an indication of more motion-related noise for the specific method (that is, the original signal or the VG degree sequence). Peristimulus maps were also calculated by averaging the signal within each run and session.

4.2.3.3 Voxelwise Analysis

Voxelwise analysis was run at the level of each participant to obtain statistical maps of a living minus non-living stimulus contrast. The classification of living (e.g., depictions of humans, living animals, plants; n = 2445) and non-living (e.g., images of tools, artifacts, buildings, food; n = 2471) stimuli was done by a trained analyst (author AO).

For the voxelwise analysis, an accuracy value was obtained from each functional image (i.e., run) as described above, by counting the correspondence between signal and expected peaks based on stimulus onsets from each stimulus category (living and nonliving). The voxelwise accuracy maps separately obtained for each stimulus category quantify the extent

to which the highest peaks of the visibility degree sequence and fMRI time series respond overlap to the onsets of each stimulus category. A living minus nonliving contrast was calculated by subtracting the two accuracy maps within each run. A one-sample permutation test was implemented using FSL randomise, based on the accuracy contrast maps to assess the significant differences between the two stimulus categories. FWR-corrected p values were obtained using Threshold Free Cluster Enhancement (TFCE) with 10,000 permutations. Voxels that passed the FWR-corrected threshold of 0.01 were considered significant.

4.3 Results

4.3.1 Synthetic event-related fMRI time series

The procedure for generating synthetic data is illustrated in **Figure 4.1**. An accuracy score was obtained by calculating the proportion of highest degree nodes (n = 99, see **Figure 4.1**, A) that corresponded to the expected HRF peaks following stimulus onset (located between 6 +/- 3 s). Unlike the synthetic fMRI time series, the VG degree sequence shows more abrupt changes around the expected HRF peaks, followed by a more sudden decrease in degree (**Figure 4.1**, B).

Average accuracy values over 1,000 iterations for each noise level are represented in **Figure 4.2**, C. Both, the VG degree sequence and fMRI time series showed a tendency to decreased accuracy with increasing noise level (**Fig 4.2, C**, r = -0.99, $p < 0.001$ for both, VG degree sequence and raw fMRI time series).

VG exhibited higher accuracy compared to the fMRI signal, but this effect is dependent on the level of noise. The average difference in accuracy between the VG and the original signal tends to gradually drop at increasing levels of gaussian noise. The effect size of the difference in accuracy between the two methods was large across noise levels between 0.1 and 0.5 [Cohen's D mean ± SD (range) = 3.26 ± 1.62 (0.92, 5.42)], where accu-

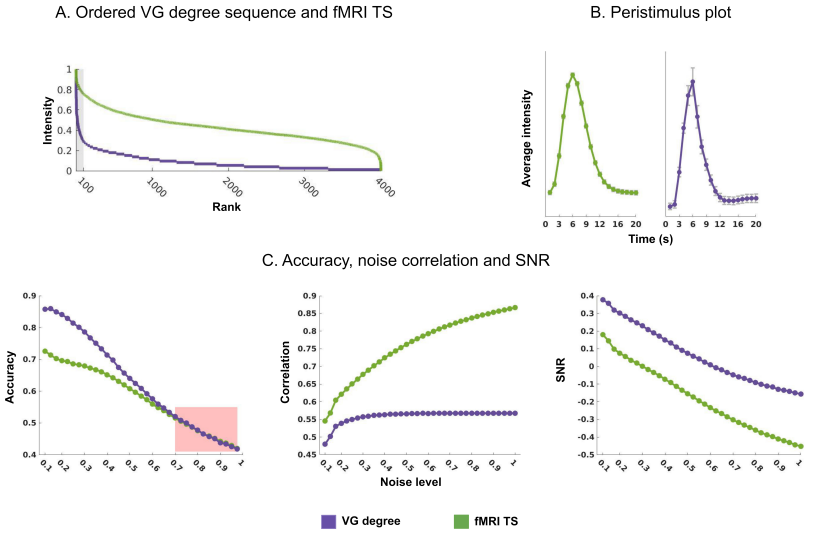

Figure 4.2: Synthetic fMRI analysis results. An accuracy score was calculated by first ordering the two time series according to their intensity (A), and then calculating the sum of time points that were adjacent to the expected HRF peak, divided by the number of events in the scan. The peristimulus plot tends to peak around 6 s post-stimulus presentation for both, the fMRI time series and VG degree sequence. C illustrates the accuracy (left), noise correlations (middle), and signal-to-noise ratio (right) of the two time series. The plot on the left side shows the average accuracy across 1000 iterations for the VG degree sequence (blue) versus synthetic signal (red) across different levels of noise. The VG degree sequence (purple) exhibits significantly higher accuracy across most noise levels. VG degree and fMRI accuracy tend to drop and converge with increasing noise until the difference between the two is no longer significant (light red shade). With increasing noise (C, middle), the fMRI time series (green) tends to exhibit higher noise correlations, whereas the VG degree time series (purple) tends to stabilize (around 0.55) as the noise level increases. Please note that VG degree sequence (purple) has consistently lower noise correlation values compared to the synthetic fMRI signal (green). The signal-to-noise ratio (C, right) was calculated as the mean accuracy value minus the mean noise-correlation value corresponding to each noise level, and VG (purple) exhibits improved SNR compared to the fMRI time series (green).

racy levels for the raw fMRI time series ranged between 0.607 and 0.726 (mean ± SD = 0.670 ± 0.033), and VG accuracy was between 0.639 and 0.859 (mean ± SD = 0.767 ± 0.07), all $p < 0.001$. Medium-to-small effect sizes were present across noise levels between 0.525 and 0.650 [Cohen's D mean ± SD (range) = 0.471 ± 0.2 (0.22, 0.735)], where the accuracy of the fMRI time series ranged between 0.539 and 0.596 (mean ± SD = 0.566 ± 0.022), and VG accuracy was between 0.547 and 0.624 (mean ± SD = 0.585 ± 0.029), all $p < 0.001$. However, the effect sizes across noise levels higher than 0.650 were very small [Cohen's D between 0.15 and 0.006; mean accuracy fMRI +/- SD (range) = 0.466 +/- 0.036 (0.415, 0.527); mean accuracy VG +/- SD (range) = 0.466 +/- 0.039 (0.411, 0.533)].

Correlations between either VG degree sequence or fMRI time series and noise showed a different pattern across the two methods (**Figure 4.2**, C). The fMRI time series showed higher noise correlations [mean ± SD (range) = 0.758 ± 0.090 (0.545, 0.866) compared to the VG degree sequence (mean ± SD (range) = 0.558 ± 0.019 (0.479, 0.567)]. Mean correlations tended to increase linearly to a greater extent as more noise was added to the raw fMRI time-series (r = 0.969, $p < 0.001$), compared to the VG degree sequence (r = 0.672, $p < 0.001$).

Signal-to-noise ratio (SNR) was calculated as the difference between accuracy and noise correlations and had a tendency to linearly decrease with increasing noise levels for both methods (both r = -0.99, $p < 0.001$). However, the signal-to-noise ratio was significantly higher when using VG compared to the raw fMRI time series across noise levels [d mean ± SD = 6.87 ± 0.51; mean SNR fMRI ± SD (range) = -0.184 ± 0.187 (0.45, 0.18); mean SNR VG ± SD (range) = 0.061 ± 0.163 (0.155, 0.378), all $p < 0.001$).

4.3.2 Task event detection on BOLD5000 dataset

V1 analysis of real event-related fMRI data from the BOLD5000 dataset was performed by calculating an accuracy score within a 3-TR window search centered on the expected HRF peak. Higher accuracy was observed for VG degree sequence compared to the original signal across

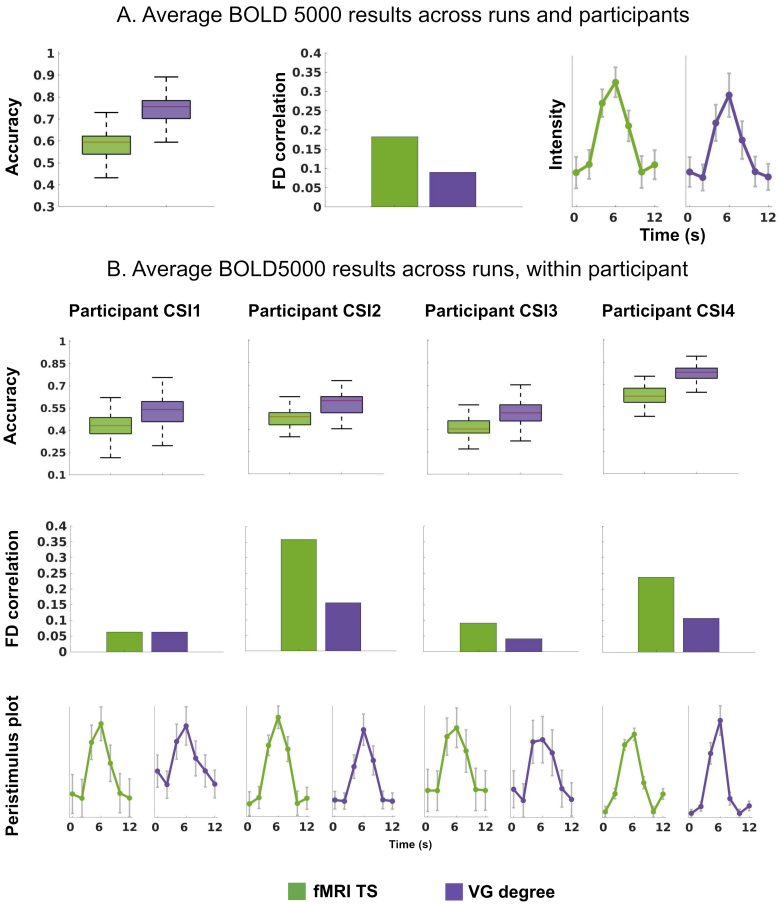

Figure 4.3: ROI analysis results based on the BOLD5000 dataset across all participants (A) and within-participant (B). VG mean accuracy (left) shows higher values across participants, compared to the fMRI time series. VG showed lower mean correlation values between each time series and the corresponding FD vector (middle) compared to the fMRI time series. Peristimulus plots (right) show that both time series tend to peak around 6 s posit-stimulus onset.

all participants [see **Figure 4.3**; CSI1 (d = 1.1, $p < 0.001$), CSI2 (d = 1.5, $p < 0.001$); CSI3 (d = 1.6, $p < 0.001$; CSI4 (d = 2.4, $p < 0.001$)]. Overall, the proportion of significant correlations (uncorrected $p < 0.05$) between signal and FD were higher in the original signal compared to the VG degree. This pattern was visible for all except one participant that had an equal number of significant FD correlations across the two methods (across 9 out of 139 runs for participant CSI1).

Peristimulus plots show significant variability of the HRFs across participants for both the original signal as well as the VG degree. On average, the peak of the HRF was consistently centered on 6 seconds post-stimulus presentation for both of the time series. This was true for all except one participant (i.e., participant CSI3), which exhibited more variability between 4 and 8 seconds post-stimulus onset.

Participant-level results using a one-sample t-test for the living minus non-living stimuli show consistently higher accuracy in bilateral occipital and occipital fusiform cortices, suggesting a similar pattern of brain activity across the four participants. **Figure 4.4** illustrates the FWR-corrected t statistical maps from the participant-level permutation text. Significant activation clusters that survived TFCE correction are presented in **Table 4.1**.

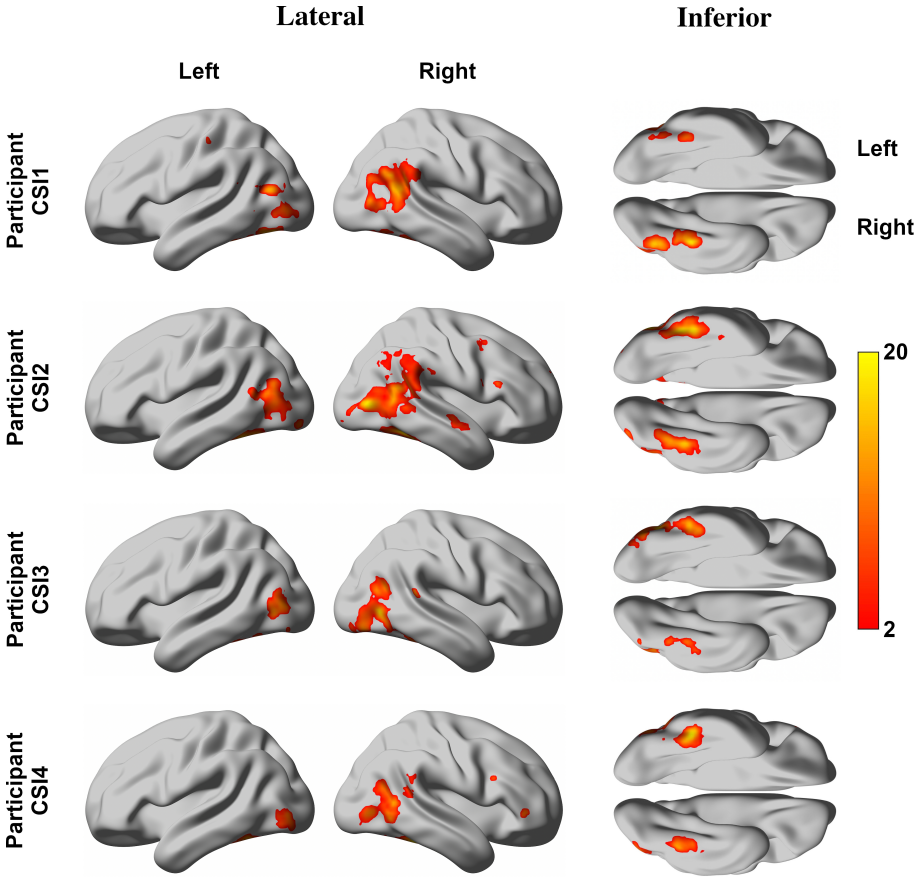

Figure 4.4: Voxelwise results for the living minus nonliving contrast from BOLD5000 dataset (one sample *t*-test at the level of each participant). The rows illustrate the FWE-corrected significant *t* values from each participant. On each column, the figure illustrates: right lateral view (column 1), left lateral view (column 2), and inferior view (column 3) of the right (upper images) and left cortices (lower images). The results indicate a consistent pattern of higher accuracy for living compared to non-living stimuli in bilateral occipital and occipital fusiform cortices.

Table 4.1: Clusters showing significant differences in accuracy for living minus non-living stimuli.

Region	Cluster size (voxels)	*t*-value	MNI152 coordinates (mm)					
			Max intensity			Center of gravity		
			x	y	z	x	y	z
Participant CSI1								
Angular gyrus (R) Lateral occipital cortex (I, S; R) Middle Temporal Gyrus (temporooccipital part; R)	2607	20.5	54	-72	2	51.8	-58.7	15.8
Lateral occipital cortex (I, S; L) Angular gyrus (L) Middle Temporal Gyrus (temporooccipital part; L)	1215	15.2	-38	-76	0	-44.7	-72.4	8.38
Temporal Occipital Fusiform Cortex (R) Lateral Occipital Cortex (I; R)	435	14.4	48	-64	-18	45.2	-56.3	-20.4
Occipital Fusiform Gyrus (L) Lateral Occipital Cortex (I; L)	377	18	-40	-70	-16	-41.6	-69	-17.1
Temporal Occipital Fusiform Cortex (L) Temporal Fusiform Cortex (L)	296	20.4	-38	-44	-22	-36.5	-46.5	-21.3
Inferior Frontal Gyrus (pars triangularis; R)	90	11.4	58	34	22	56.7	32.1	22.8
Inferior Frontal Gyrus (pars opercularis; R)	42	9.9	52	14	34	50.9	14.9	33.3
Middle Frontal Gyrus (R)	28	9	44	2	56	44.6	3.25	54.8
Precuneous Cortex (R)	18	7.34	6	-62	18	4.81	-62.6	18.9
Postcentral Gyrus (L)	12	9	-50	-24	52	-50.9	-24	52.6

Region	Cluster size (voxels)	*t*-value	MNI152 coordinates (mm)					
			Max intensity			Center of gravity		
			x	y	z	x	y	z
Participant CSI2								
Lateral occipital cortex (I, S; R) Middle Temporal Gyrus (temporooccipital part; R) Angular gyrus (R) Supramarginal Gyrus (P; R) Temporal Occipital Fusiform Cortex (R) Inferior Temporal Gyrus (temporooccipital part, R) Inferior Temporal Gyrus (P; R) Temporal Fusiform Cortex (P; R)	4753	20.9	50	-72	4	50.5	-56.7	5.1
Precuneous Cortex (B)	2586	8.82	22	-70	28	2.87	-62.5	39.1
Lateral Occipital Cortex (I, S; L) Angular Gyrus (L)	1724	19.7	-54	-76	8	-49.1	-71.3	9.51
Temporal Occipital Fusiform Cortex (L) Temporal Fusiform Cortex (P, L) Occipital Fusiform Gyrus (L)	785	16.7	-40	-48	-20	-41.2	-54.5	-21.5
Frontal pole (L, R) Paracingulate Gyrus (M)	422	7	8	62	24	4.45	60.1	23
Inferior Frontal Gyrus (pars opercularis, R)	168	9.13	52	18	22	55	15.7	23.8

Region	Cluster size (voxels)	*t*-value	MNI152 coordinates (mm)					
			Max intensity			Center of gravity		
			x	y	z	x	y	z
Superior Temporal Gyrus (A; R) Middle Temporal Gyrus (P; R)	127	7.28	56	-14	-6	55.7	-9.52	-10.6
Lateral Occipital Cortex (I; L)	102	10.6	-40	-90	-12	-34.9	-90.2	-10.6
Middle Frontal Gyrus (R)	38	5.7	42	10	50	43.1	8.59	50.5
Cingulate Gyrus (A, M), Paracingulate Gyrus (M)	23	5	0	26	30	0.407	32.4	28.3
Frontal Pole (R)	15	7.64	52	36	0	53.3	37.6	-1.18
Cingulate gyrus (A; M)	14	4.86	8	20	18	4.62	20.2	19.4
Lingual Gyrus (L)	9	5.46	-10	-66	-8	-8.89	-66.3	-6.49
Inferior Frontal Gyrus (pars opercularis, L)	5	9.02	-60	18	18	-59.2	18	17.6
Participant CSI3								
Lateral Occipital Cortex (I, S; R) Inferior Temporal Gyrus (temporooccipital part, R) Temporal Occipital Fusiform Cortex (R)	1880	18.9	48	-48	-24	47.3	-64.3	-2.12
Lateral Occipital Cortex (I, S; L)	794	13.6	-48	-78	6	-47.2	-76.1	7.5
Temporal Occipital Fusiform Cortex (L)	302	12.3	-38	-54	-24	-40.7	-49.7	-22.9
Supramarginal Gyrus (P; R), Angular Gyrus (R)	56	11.9	58	-40	14	61.3	-44.1	15
Lateral Occipital Cortex (S; R)	17	10.4	22	-82	48	22.3	-81.4	47.6
Lateral Occipital Cortex (I, S; L)	10	10.1	-40	-82	-14	-40.4	-82.6	-13.4

Region	Cluster size (voxels)	*t*-value	MNI152 coordinates (mm)					
			Max intensity			Center of gravity		
			x	y	z	x	y	z
Participant CSI4								
Lateral Occipital Corte (I, S; R), Middle Temporal Gyrus (temporooccipital part, R) Angular Gyrus (R)	1804	17.5	58	-62	-4	53.5	-65.7	4.6
Lateral Occipital Corte (I; L)	733	16	-56	-72	-4	-51	-76.8	-0.628
Temporal Occipital Fusiform Cortex (R)	443	20.6	42	-44	-22	42.4	-44.8	-22.9
Temporal Occipital Fusiform Cortex (L) Temporal Fusiform Cortex (P; L)	338	14.4	-42	-54	-20	-41.9	-51.2	-21.9
Inferior Frontal Gyrus (pars opercularis, R)	27	9.93	40	16	24	42.4	14.4	24.6
Frontal Pole (R)	21	9.63	48	38	0	48.2	37.8	0.282

4.4 Discussion

The current work evaluated if temporal networks derived using VG transformation preserves event related task-evoked hemodynamic activity of synthetic time series and real fMRI data. The VG degree sequence could successfully recover task activity because signal changes associated with task events were converted to high-degree nodes. Unlike the GLM approach, VG mapping is performed without using a basis function to define the HRF shape, which is promising for applications in fMRI time series analysis where linear modeling has limited utility, including the analysis of continuous task designs. The accuracy of identifying task events was consistently higher compared to the raw fMRI time series, supporting the hypothesis that VG topology contains signal changes associated with task events. The degree sequence of VG demonstrated robustness to gaussian noise added to synthetic data and motion-related noise based on framewise displacement in real fMRI data. Voxelwise results of a living minus non-living whole-brain contrast replicated previously reported activation maps using the GLM approach, showing consistent participant-level patterns across the ventral pathway, which suggests that VG transformation embodies similar signal features to those previously observed with GLM.

VG transformation emphasizes signal peaks associated with task events relative to the raw fMRI signals. In well-controlled, simulated data, the VG degree sequence of the fMRI time series may amplify the signal intensity of time points corresponding to HRF peaks. Task-evoked signal intensity changes result in temporal nodes with a high degree centrality, as evidenced by the correspondence between high-degree nodes and the timing of the expected HRF peaks. However, this effect depends on the level of noise added to the time series, indicating that VG mapping may provide improved task detection in time series with relatively lower noise levels. This result was successfully replicated using real event-related task fMRI time series extracted from V1 during the picture presentation task, suggesting that VG contains task event information under real conditions and task events accurately identified based on VG degree sequence com-

pared with the raw fMRI time series. This is the first evidence to show what task activity can be recovered based on the topology of the temporal graphs, and extends previous findings using resting-state fMRI and EEG. Specifically, previous studies focused on quantifying the similarity between pairs of region-wise temporal graphs to derive properties similar to functional connectivity, for example, based on the mutual information VG partitions or the correlation between VG degree sequences. However, it was not clear whether VG topology incorporates signal changes evoked during task. The pivotal advantage of VG transformation is that task-induced variations can be identified without relying on a basis function, by localizing highly connected nodes (time points) across the time series. Voxelwise results based on accuracy differences for the living minus non-living contrast exhibited consistent patterns across participants. These results are consistent with previous studies showing increased activation for this contrast based on GLM analysis, including the lateral occipital cortices, inferior frontal gyrus, fusiform gyrus, and posterior parts of the superior temporal gyrus (see Derderian, X. Zhou, and L. Chen, 2021 for a meta-analysis).

The influence of noise is an important issue for fMRI, and VG degree sequence demonstrated robustness to gaussian and, to some extent, to participant motion spikes. Despite a decrease in accuracy across higher levels of gaussian noise in the synthetic time series, the VG degree sequence showed lower noise correlations relative to the raw time series (see **Figure 4.2**, C). In addition, at relatively lower noise levels, both signals showed gradually increasing correlations with the gaussian noise, but VG degree tended to stabilize, and the raw time series continually increased, suggesting that VG might show better robustness to gaussian noise. The estimation of signal-to-noise ratio was calculated as the difference between task event identification accuracy and noise correlations and it decreased across both VG degree and raw synthetic time series as more noise was added. However, the VG degree sequence exhibited systematically higher signal-to-noise ratios compared to the raw time series across all noise levels. This suggests that VG transformation of the time

series could improve signal detection, although whether this effect can extend to real fMRI data may be more challenging to estimate provided the more complex noise structure specific to real fMRI data, which may not necessarily follow a gaussian distribution.

The proposed technique expands previous work addressing non-linear time-series processing for task fMRI. Several implications are worth mentioning. VG graph mapping can offer new possibilities for signal analysis using statistical learning techniques adapted for graphs, temporal community detection (Zheng et al., 2021), or network properties such as complexity or fractality (Bhaduri and Ghosh, 2015). Such approaches are becoming increasingly popular in the literature (Zou et al., 2019), and one interesting question future studies may address is whether VG topology can accurately differentiate between event-related signal intensity peaks and noise variability including motion spikes in fMRI time series, which could help separate signal and noise variability for task and resting-state acquisitions. The study of VG mapping in event-related fMRI can provide a promising basis to stimulate new applications for fMRI modeling, for example across experimental settings where information about event onsets is not available (Saarimäki, 2021). Continuous stimulation in tasks such as movie watching or story listening can be more challenging to model based on GLM in the absence of systematic control over stimulus onset and duration. Another promising future application may address signals from brain areas where task-related oscillations do not follow the shape of the canonical HRF. Recent evidence indicates that white matter areas can elicit BOLD responses following task events (M. Li et al., 2019), where the HRF manifests higher spatial and temporal variability compared to gray matter, making this type of response challenging to predict using pre-established basis functions.

The current work has several limitations. Due to the VG construction algorithm, frame-to-frame movement spikes may bias the degree distribution, artificially introducing extreme events that are not related to task events. To overcome this problem, additional variables of no interest need to be inserted in the model during noise regression (i.e., by dummy

coding each movement spike as a separate variable), which may further reduce signal variability by the loss of degrees of freedom associated with a given TS. Consequently, the proposed modeling technique may exhibit increased sensitivity to noise across scans suffering from severe movement, potentially limiting its applicability in children and patient populations. The current dataset contained scans collected from highly trained participants which demonstrated reduced in-scanner motion artifact, and future studies may test how VG topology is affected in time series with higher in-scanner participant motion. The current analysis tested VG in fMRI time series with known task event information (i.e., onset and duration) and further studies may focus on assessing how this information can be used to model fMRI time series in experiments with unknown task events onsets for example by using global parameters of node classification techniques. In addition, participant-level contrasts were derived in the current study, and future studies may address the applicability of VG for group-level analysis. In this analysis, VG degree and the original fMRI signal showed similar HRF shapes, suggesting that both time-series tend to peak at the same timing following stimulus onset, both in synthetic (see **Figure 4.2**) and real fMRI data (see **Figure 4.3**). However, future analyses may consider a more detailed evaluation of the relationship between original fMRI signal and the VG degree sequence, including the influence of temporal autocorrelation function of the fMRI signal in VG topological features. Lastly, the efficiency of VG was assessed using the degree sequence, however, testing the relevance of other local and global graph properties and how combining different features can contribute for different applications in fMRI data analysis may be of interest for future analyses.

Chapter 5

Conclusion

The current work addressed several issues relevant to the field of network neuroscience. The collection of large neuroimaging datasets can improve inference by increasing statistical power, however, flexibility in analytical workflows and how it may affect research results represent a growing concern in neuroimaging (e.g., Botvinik-Nezer et al., 2020). As multi-site data collection and the use of network science techniques become more prevalent in neuroimaging, evaluating the impact of harmonization procedures on the reliability of network metrics can aid in making better analytical decisions. The results presented in Chapter 2 show that differences in data harmonization workflows can affect structural network topology in a multi-site study of pediatric mild traumatic brain injury. The harmonization of network parameters was found to be more efficient than matrix harmonization in removing scanner effects and preserving the biological effects of age on network topology. The results extend the validity of using ComBat harmonization to network parameters derived using diffusion-weighted MRI and show that the harmonization of connectivity matrices can alter the original variability in network topology, resulting in variable performance across different metrics.

Rigorous data harmonization of network metrics derived using graph

theory can help address complex questions about the impact of mild TBI in functional network topology. The analysis of the largest study of pediatric mild TBI to date, the A-CAP study, expands the understanding of the heterogeneity specific to the pediatric population. In Chapter 3, functional abnormalities at both the global and local brain network levels were demonstrated in children following mTBI relative to OI. Those differences were moderated by time-post-injury, biological sex, age at injury, and symptom persistence at 1-month post-injury. Postacute abnormalities in functional network topology did not predict symptom persistence at 1-month post-injury, however, longitudinal topological changes were more prominent among children with persistent symptoms. Local alterations may affect females more than males and may occur more frequently at 3 months post-injury, with a tendency to reduce at 6 months. The results highlight that mild TBI is best contextualized within clinical subtypes by emphasizing the role of moderating variables on brain function.

Finally, linear methods for fMRI signal processing and connectome mapping provide a valuable contribution to the field of network neuroscience, however, incorporating data analytical models that capture non-linear features of hemodynamic variability is critical to accurately measure brain function. Applications of graph theory in neuroscience typically address networks where nodes represent brain regions, but temporal networks, where nodes represent time-points, are promising for time series analysis. Methodological approaches for time series analysis derived using functional neuroimaging remain a pivotal topic in cognitive and clinical neuroscience, and Chapter 4 addresses whether temporal networks constructed using VG transformation can preserve the event-related task-evoked hemodynamic activity. By analyzing synthetic and real fMRI data, we found that VG degree sequence successfully recovered task activity by converting signal changes associated with task events to high-degree nodes. The accuracy of identifying task events was consistently higher compared with the initial fMRI time series, supporting the hypothesis that VG topology contains signal changes associated with task events. The degree sequence of VG demonstrated robustness to noise added to

synthetic data and motion-related noise in real fMRI data. In addition, the voxelwise analysis of a living minus non-living stimulus contrast showed consistent participant-level statistical patterns across the ventral visual pathway, suggesting that VG transformation embodies similar signal features to those previously observed with GLM. The results raise new possibilities for fMRI data analysis beyond the typical approaches based on linear modeling.

Appendix A

Supplementary information for Chapter 2

Table A.1: Information about AAL atlas.

Label	Region	Hemisphere	MNI coordinates (mm)			Voxel count	Anatomical classification
			x	y	z		
1	Precental gyrus	Left	-38,65	-5,68	50,94	1028	Frontal
2	Precental gyrus	Right	41,37	-8,21	52,09	1002	Frontal
3	Superior frontal gyrus, dorsolateral	Left	-18,45	34,81	42,20	1076	Prefontal
4	Superior frontal gyrus, dorsolateral	Right	21,90	31,12	43,82	1159	Prefontal
5	Superior frontal gyrus, orbital part	Left	-16,56	47,32	-13,31	292	Prefontal
6	Superior frontal gyrus, orbital part	Right	18,49	48,10	-14,02	311	Prefontal
7	Middle frontal gyrus	Left	-33,43	32,73	35,46	1448	Prefontal
8	Middle frontal gyrus	Right	37,59	33,06	34,04	1510	Prefontal
9	Middle frontal gyrus, orbital part	Left	-30,65	50,43	-9,62	270	Prefontal
10	Middle frontal gyrus, orbital part	Right	33,18	52,59	-10,73	294	Prefontal
11	Inferior frontal gyrus, opercular part	Left	-48,43	12,73	19,02	326	Prefontal
12	Inferior frontal gyrus, opercular part	Right	50,20	14,98	21,41	421	Prefontal
13	Inferior frontal gyrus, triangular part	Left	-45,58	29,91	13,99	726	Prefontal
14	Inferior frontal gyrus, triangular part	Right	50,33	30,16	14,17	629	Prefontal
15	Inferior frontal gyrus, orbital part	Left	-35,98	30,71	-12,11	503	Prefontal
16	Inferior frontal gyrus, orbital part	Right	41,22	32,23	-11,91	505	Prefontal
17	Rolandic operculum	Left	-47,16	-8,48	13,95	302	Frontal
18	Rolandic operculum	Right	52,65	-6,25	14,63	399	Frontal
19	Supplementary motor area	Left	-5,32	4,85	61,38	656	Frontal
20	Supplementary motor area	Right	8,62	0,17	61,85	666	Frontal
21	Olfactory cortex	Left	-8,06	15,05	-11,46	87	Prefontal
22	Olfactory cortex	Right	10,43	15,91	-11,26	81	Prefontal
23	Superior frontal gyrus, medial	Left	-4,80	49,17	30,89	846	Prefontal
24	Superior frontal gyrus, medial	Right	9,10	50,84	30,22	641	Prefontal
25	Superior frontal gyrus, medial orbital	Left	-5,17	54,06	-7,40	225	Prefontal

Table A.1 continued from previous page

Label	Region	Hemisphere	MNI coordinates (mm)			Voxel count	Anatomical classification
			x	y	z		
26	Superior frontal gyrus, medial orbital	Right	8,16	51,67	-7,13	262	Prefontal
27	Gyrus rectus	Left	-5,08	37,07	-18,14	261	Prefontal
28	Gyrus rectus	Right	8,35	35,64	-18,04	218	Prefontal
29	Insula	Left	-35,13	6,65	3,44	566	Subcortical
30	Insula	Right	39,02	6,25	2,08	539	Subcortical
31	Anterior cingulate and paracingulate gyri	Left	-4,04	35,40	13,95	426	Prefontal
32	Anterior cingulate and paracingulate gyri	Right	8,46	37,01	15,84	397	Prefontal
33	Median cingulate and paracingulate gyri	Left	-5,48	-14,92	41,57	619	Frontal
34	Median cingulate and paracingulate gyri	Right	8,02	-8,83	39,79	605	Frontal
35	Posterior cingulate gyrus	Left	-4,85	-42,92	24,67	137	Parietal
36	Posterior cingulate gyrus	Right	7,44	-41,81	21,87	87	Parietal
37	Hippocampus	Left	-25,03	-20,74	-10,13	273	Temporal
38	Hippocampus	Right	29,23	-19,78	-10,33	288	Temporal
39	Parahippocampal gyrus	Left	-21,17	-15,95	-20,70	286	Temporal
40	Parahippocampal gyrus	Right	25,38	-15,15	-20,47	316	Temporal
41	Amygdala	Left	-23,27	-0,67	-17,14	62	Temporal
42	Amygdala	Right	27,32	0,64	-17,50	70	Temporal
43	Calcarine fissure and surrounding cortex	Left	-7,14	-78,67	6,44	648	Occipital
44	Calcarine fissure and surrounding cortex	Right	15,99	-73,15	9,40	542	Occipital
45	Cuneus	Left	-5,93	-80,13	27,22	449	Occipital
46	Cuneus	Right	13,51	-79,36	28,23	434	Occipital
47	Lingual gyrus	Left	-14,62	-67,56	-4,63	660	Occipital
48	Lingual gyrus	Right	16,29	-66,93	-3,87	678	Occipital
49	Superior occipital gyrus	Left	-16,54	-84,26	28,17	396	Occipital
50	Superior occipital gyrus	Right	24,29	-80,85	30,59	428	Occipital
51	Middle occipital gyrus	Left	-32,39	-80,73	16,11	959	Occipital

Table A.1 continued from previous page

Label	Region	Hemisphere	MNI coordinates (mm)			Voxel count	Anatomical classification
			x	y	z		
52	Middle occipital gyrus	Right	37,39	-79,70	19,42	595	Occipital
53	Inferior occipital gyrus	Left	-36,36	-78,29	-7,84	268	Occipital
54	Inferior occipital gyrus	Right	38,16	-81,99	-7,61	314	Occipital
55	Fusiform gyrus	Left	-31,16	-40,30	-20,23	687	Temporal
56	Fusiform gyrus	Right	33,97	-39,10	-20,18	760	Temporal
57	Postcentral gyrus	Left	-42,46	-22,63	48,92	1159	Parietal
58	Postcentral gyrus	Right	41,43	-25,49	52,55	1138	Parietal
59	Superior parietal gyrus	Left	-23,45	-59,56	58,96	631	Parietal
60	Superior parietal gyrus	Right	26,11	-59,18	62,06	647	Parietal
61	Inferior parietal	Left	-42,80	-45,82	46,74	696	Parietal
62	Inferior parietal	Right	46,46	-46,29	49,54	419	Parietal
63	Supramarginal gyrus	Left	-55,79	-33,64	30,45	354	Parietal
64	Supramarginal gyrus	Right	57,61	-31,50	34,48	550	Parietal
65	Angular gyrus	Left	-44,14	-60,82	35,59	342	Parietal
66	Angular gyrus	Right	45,51	-59,98	38,63	496	Parietal
67	Precuneus	Left	-7,24	-56,07	48,01	1079	Parietal
68	Precuneus	Right	9,98	-56,05	43,77	935	Parietal
69	Paracentral lobule	Left	-7,63	-25,36	70,07	422	Parietal
70	Paracentral lobule	Right	7,48	-31,59	68,09	227	Parietal
71	Caudate nucleus	Left	-11,46	11,00	9,24	278	Subcortical
72	Caudate nucleus	Right	14,84	12,07	9,42	284	Subcortical
73	Lenticular nucleus, putamen	Left	-23,91	3,86	2,40	306	Subcortical
74	Lenticular nucleus, putamen	Right	27,78	4,91	2,46	322	Subcortical
75	Lenticular nucleus, pallidum	Left	-17,75	-0,03	0,21	81	Subcortical
76	Lenticular nucleus, pallidum	Right	21,20	0,18	0,23	76	Subcortical
77	Thalamus	Left	-10,85	-17,56	7,98	313	Subcortical

Table A.1 continued from previous page

Label	Region	Hemisphere	MNI coordinates (mm)			Voxel count	Anatomical classification
			x	y	z		
78	Thalamus	Right	13,00	-17,55	8,09	307	Subcortical
79	Heschl gyrus	Left	-41,99	-18,88	9,98	72	Temporal
80	Heschl gyrus	Right	45,86	-17,15	10,41	73	Temporal
81	Superior temporal gyrus	Left	-53,16	-20,68	7,13	672	Temporal
82	Superior temporal gyrus	Right	58,15	-21,78	6,80	963	Temporal
83	Temporal pole: superior temporal gyrus	Left	-39,88	15,14	-20,18	382	Temporal
84	Temporal pole: superior temporal gyrus	Right	48,25	14,75	-16,86	400	Temporal
85	Middle temporal gyrus	Left	-55,52	-33,80	-2,20	1439	Temporal
86	Middle temporal gyrus	Right	57,47	-37,23	-1,47	1356	Temporal
87	Temporal pole: middle temporal gyrus	Left	-36,32	14,59	-34,08	222	Temporal
88	Temporal pole: middle temporal gyrus	Right	44,22	14,55	-32,23	349	Temporal
89	Inferior temporal gyrus	Left	-49,77	-28,05	-23,17	941	Temporal
90	Inferior temporal gyrus	Right	53,69	-31,07	-22,32	1072	Temporal

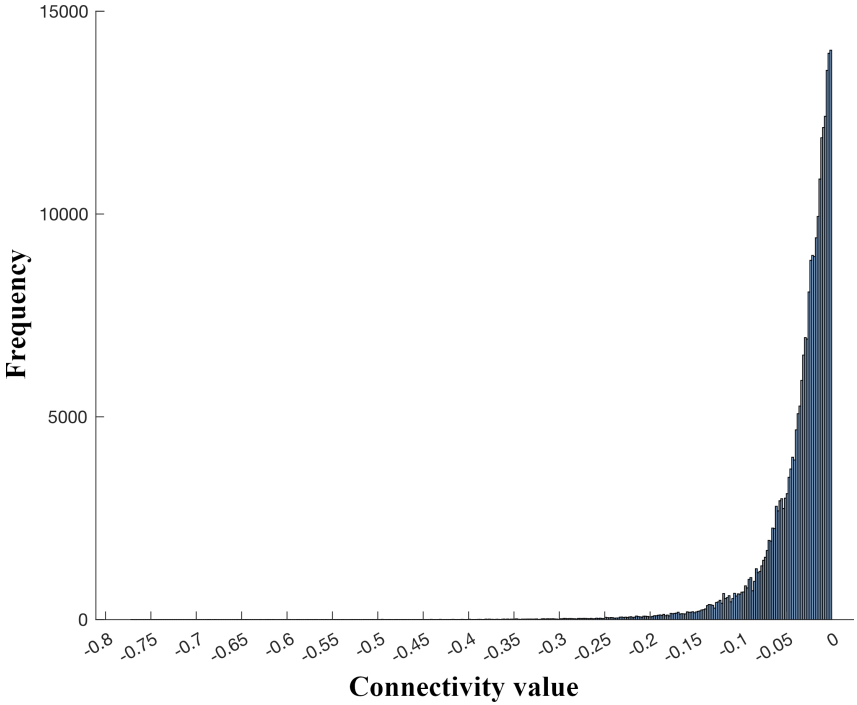

Figure A.1: Distribution of negative connection weights following matrix harmonization.

Appendix B

Supplementary information for Chapter 3

	Concussion	OI
Inclusion	A blunt head trauma with at least one of the following injury characteristics: • Lowest GCS score of 13-14 (out of 15) • Observed LOC • At least one reported symptom (e.g., PTA, focal neurological deficits, skull fracture, post-traumatic seizure, vomiting, headache, dizziness, other mental status change) noted by ED medical personnel around the time of injury	• An orthopaedic (i.e., non-head) injury to the thorax, upper extremity and/or lower extremity with Abbreviated Injury Scale Score of 4 or less • Injury related to blunt force/physical trauma
	Both Groups • Presentation to the ED within 48 hours of injury	
Exclusion	• A more severe TBI with the following characteristics: o A GCS score of ≤ 13; o LOC ≥ 30 minutes; or o PTA ≥ 24 hours o Neurosurgical intervention • Associated OI with AIS score > 4	• Any injury requiring surgical intervention or procedural sedation (not excluded for use of analgesic/pain management medication) • Head trauma or symptoms of concussion
	Both Groups • Hypoxia, hypotension, or shock during or following injury (if known) • Non-English-speaking child or parents (non-English and non-French speaking in Quebec and Ottawa) • Previous TBI requiring overnight hospitalization, by parent report • Previous concussion within the past 3 months, by parent report • Previous neurological or neurodevelopmental disorder (e.g., epilepsy, intellectual disability, autism spectrum disorder), by parent report • Hospitalization in the previous year for psychiatric disorder, by parent report • Administration of sedative medication (e.g., Propofol, ketamine, nutrouus oxide, midazolam, benzodiazepines) prior to ED data collection (pain management medications not an exclusion) • Obvious drug or alcohol ingestion associated with injury • Injury-related abuse or assault • Legal guardian not present or child in foster care • Excluded from MRI if child has orthodontic (e.g., braces) or medical contraindications to MRI	

Table A.1. Inclusion and exclusion criteria for the A-CAP study. ED – Emergency Department, OI – Orthopedic Injury, GCS – Glasgow Coma Scale, LOC – Loss of Consciousness, PTA – Post-Traumatic Amnesia

Table B.1: Demographic information of participants by scanning session across sites

Site	Participants		Sex n (%) male	Age M (SD) years	DPI M (SD)
	N (%)	n (%) mTBI			
Post-acute					
All sites	**502**	**329**	**300**	**12.5 (2,3)**	**11,4 (5,4)**
Calgary	107 (21,3%)	75 (14,9%)	67 (13,3%)	13,2 (2,1)	8,8 (3,6)
Edmonton	108 (21,5%)	72 (14,3%)	63 (12,5%)	12,8 (2,3)	9,0 (4,9)
Montreal 1	23 (4,6%)	19 (3,8%)	14 (2,8%)	12,0 (2,0)	9,9 (4,0)
Montreal 2	20 (4,0%)	13 (2,6%)	10 (2,0%)	12,9 (2,3)	12,6 (4,7)
Ottawa	108 (21,5%)	81 (16,1%)	61 (12,2%)	11,9 (2,4)	16,0 (5,0)
Vancouver	136 (27,1%)	69 (13,7%)	85 (16,9%)	12,2 (2,4)	11,8 (5,2)
3 months					
All sites	**197**	**133**	**112**	**12.3 (2,4)**	**96,6 (8,7)**
Calgary	46 (23,4%)	32 (16,2%)	31 (15,7%)	13,1 (2,4)	95,2 (8,1)
Edmonton	36 (18,3%)	26 (13,2%)	17 (8,6%)	12,7 (2,3)	100,2 (10,3)
Montreal 1	9 (4,6%)	8 (4,1%)	5 (2,5%)	12,0 (1,3)	95,7 (12,1)
Montreal 2	11 (5,6%)	7 (3,6%)	5 (2,5%)	12,6 (2,7)	99,6 (11,7)
Ottawa	40 (20,3%)	29 (14,7%)	20 (10,2%)	11,6 (2,3)	96,5 (7,5)
Vancouver	55 (27,9%)	31 (15,7%)	34 (17,3%)	12,0 (2,5)	94,9 (7,1)
6 months					
All sites	**219**	**141**	**136**	**12.5 (2,4)**	**186,0 (11.0)**
Calgary	51 (23,3%)	38 (17,4%)	32 (14,6%)	12,8 (2,1)	187,8 (8,3)
Edmonton	55 (25,1%)	33 (15,1%)	34 (15,5%)	12,9 (2,4)	188,8 (14,5)
Montreal 1	4 (1,8%)	3 (1,4%)	2 (0,9%)	11,0 (0,6)	200,8 (9,4)
Montreal 2	7 (3,2%)	4 (1,8%)	4 (1,8%)	13,3 (1,8)	198,2 (5,8)
Ottawa	44 (20,1%)	30 (13,7%)	22 (10,0%)	12,0 (2,6)	178,7 (7,1)
Vancouver	58 (26,5%)	33 (15,1%)	42 (19,2%)	12,2 (2,4)	184,8 (8,7)

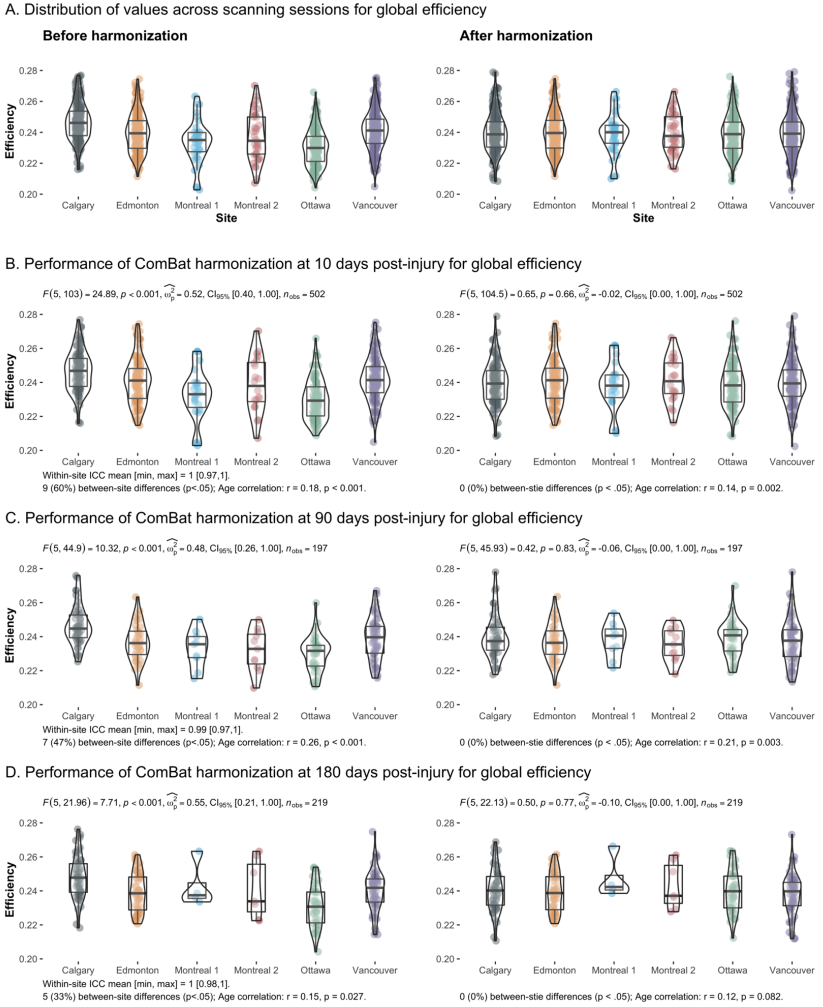

Figure B.1: Results summarising the assessment of ComBat harmonization for efficiency.

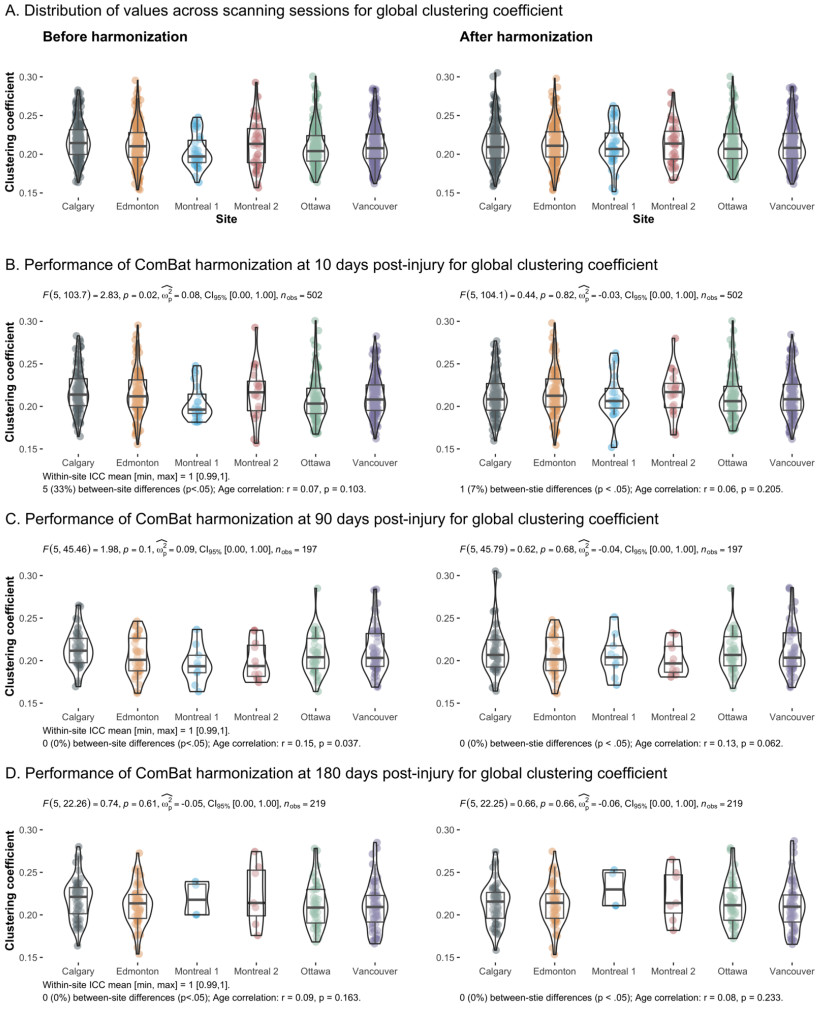

Figure B.2: Results summarising the assessment of ComBat harmonization for clustering coefficient.

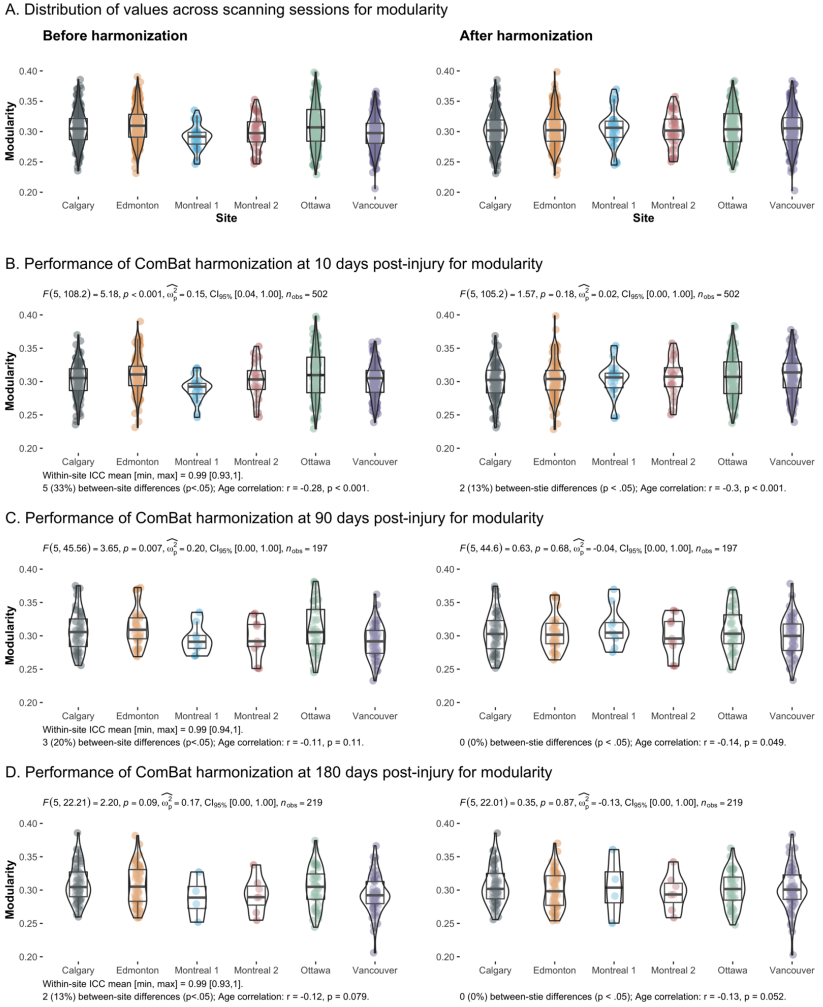

Figure B.3: Results summarising the assessment of ComBat harmonization for modularity.

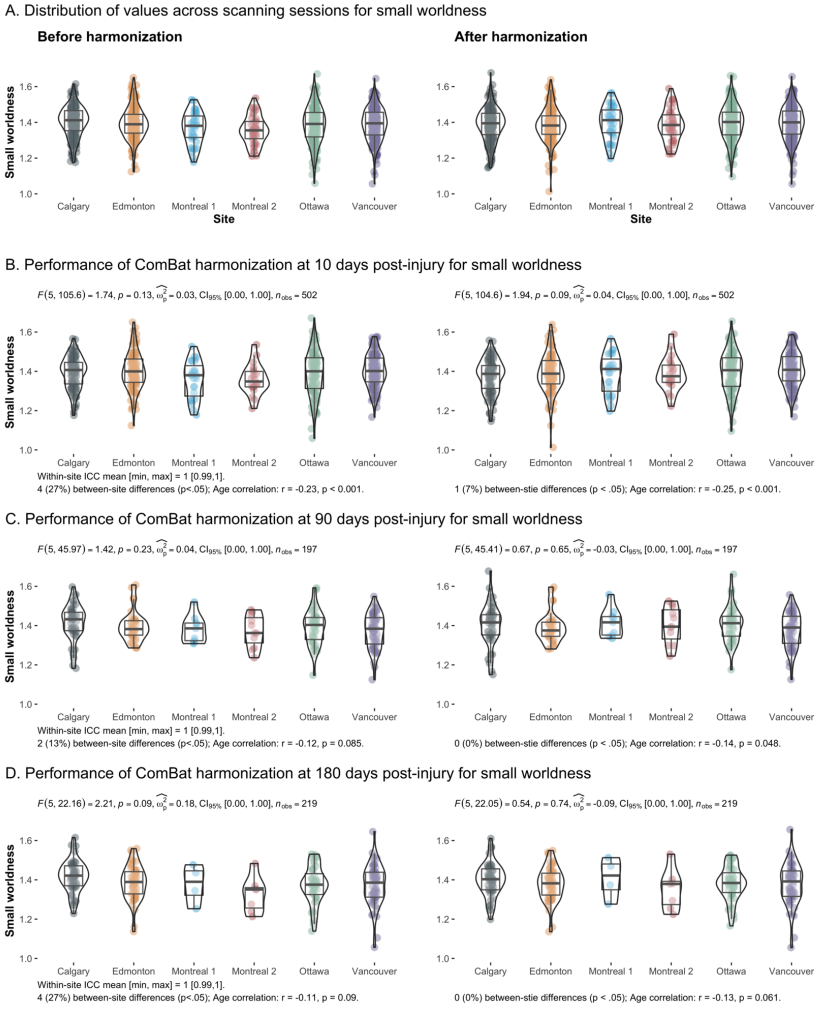

Figure B.4: Results summarising the assessment of ComBat harmonization for small worldness.

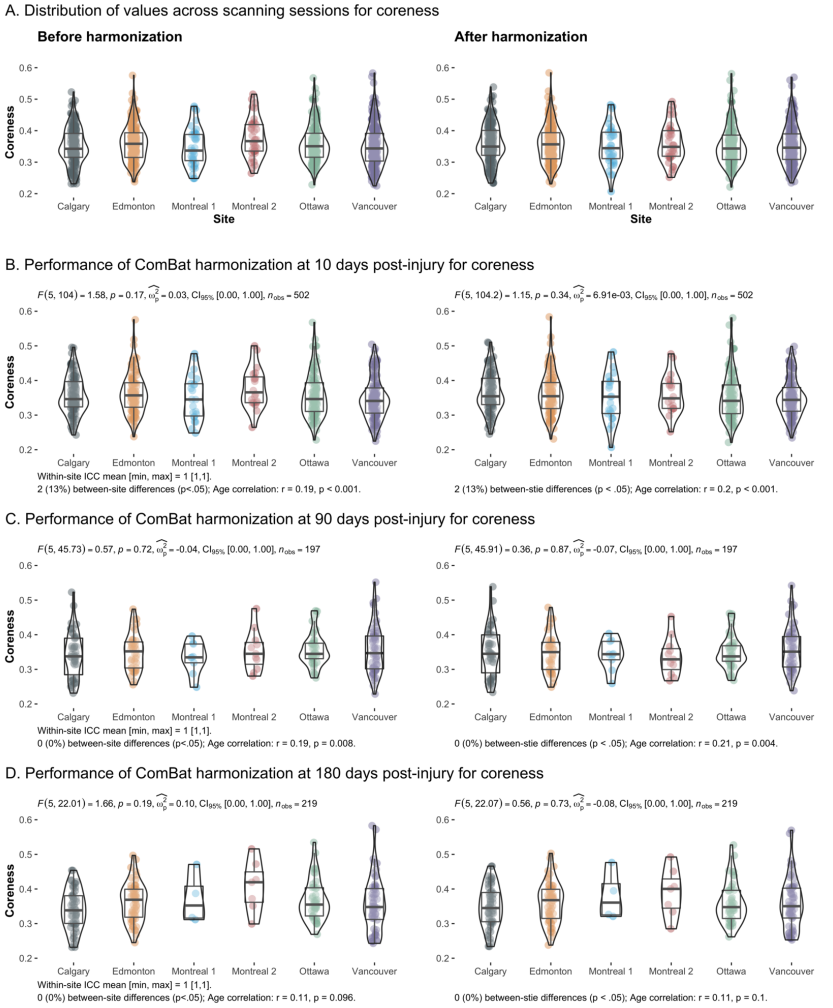

Figure B.5: Results summarising the assessment of ComBat harmonization for core-periphery organization.

Bibliography

Achard, Sophie and Ed Bullmore (Feb. 2007). "Efficiency and Cost of Economical Brain Functional Networks". In: *PLoS Computational Biology* 3.2. [Online; accessed 2022-06-30], e17.

Adelson, P David et al. (2012). "Common data elements for pediatric traumatic brain injury: recommendations from the working group on demographics and clinical assessment". In: *Journal of neurotrauma* 29.4, pp. 639–653.

Aerts, Hannelore et al. (Dec. 2016). "Brain networks under attack: robustness properties and the impact of lesions". In: *Brain* 139.Pt, p. 12. ISSN: 1460-2156. DOI: 10.1093/brain/aww194. eprint: 27497487.

Ahmadlou, Mehran, Hojjat Adeli, and Anahita Adeli (Sept. 2010). "New diagnostic EEG markers of the Alzheimer's disease using visibility graph". In: *J. Neural Transm.* 117.9, pp. 1099–1109. ISSN: 1435-1463. DOI: 10.1007/s00702-010-0450-3.

Ahmadlou, Mehran, Khodabakhsh Ahmadi, et al. (2013). "Global organization of functional brain connectivity in methamphetamine abusers". In: *Clinical neurophysiology* 124.6, pp. 1122–1131.

Alexander, Andrew L. et al. (July 2007). "Diffusion tensor imaging of the brain". In: *Neurotherapeutics* 4.3, p. 316. DOI: 10.1016/j.nurt.2007.05.011.

Alnawmasi, Mohammed M, Revathy Mani, and Sieu K Khuu (2022). "Changes in the components of visual attention following traumatic brain injury: A systematic review and meta-analysis". In: *Plos one* 17.6, e0268951.

Alstott, Jeffrey et al. (2009). "Modeling the impact of lesions in the human brain". In: *PLoS computational biology* 5.6, e1000408.

Armstrong, Richard A (2018). "Visual problems associated with traumatic brain injury". In: *Clinical and Experimental Optometry* 101.6, pp. 716–726.

Avants, B. B. et al. (Feb. 1, 2008). "Symmetric Diffeomorphic Image Registration with Cross-Correlation: Evaluating Automated Labeling of Elderly and Neurodegenerative Brain". In: *Medical Image Analysis*. Special Issue on The Third International Workshop on Biomedical Image Registration – WBIR 2006 12.1, pp. 26–41. ISSN: 1361-8415. DOI: 10.1016/j.media.2007.06.004. URL: https://www.sciencedirect.com/science/article/pii/S1361841507000606 (visited on 05/29/2022).

Avena-Koenigsberger, Andrea, Bratislav Misic, and Olaf Sporns (2018). "Communication dynamics in complex brain networks". In: *Nature Reviews Neuroscience* 19.1, p. 17.

Ayr, Lauren K et al. (2009). "Dimensions of postconcussive symptoms in children with mild traumatic brain injuries". In: *Journal of the International Neuropsychological Society* 15.1, pp. 19–30.

Babl, Franz E. et al. (June 2017). "Accuracy of PECARN, CATCH, and CHALICE head injury decision rules in children: a prospective cohort study". In: *Lancet* 389.10087, pp. 2393–2402. ISSN: 1474-547X. DOI: 10.1016/S0140-6736(17)30555-X. eprint: 28410792.

Barkovich, Matthew J et al. (2019). "Challenges in pediatric neuroimaging". In: *Neuroimage* 185, pp. 793–801.

Bassett, Danielle S and Olaf Sporns (2017). "Network neuroscience". In: *Nature neuroscience* 20.3, pp. 353–364.

Beer, Joanne C et al. (2020). "Longitudinal combat: A method for harmonizing longitudinal multi-scanner imaging data". In: *Neuroimage* 220, p. 117129.

Belanger, Heather G. et al. (May 2005). "Factors moderating neuropsychological outcomes following mild traumatic brain injury: A meta-analysis". In: *J. Int. Neuropsychol. Soc.* 11.3, pp. 215–227. ISSN: 1469-7661. DOI: 10.1017/S1355617705050277.

Bhaduri, Susmita and Dipak Ghosh (July 2015). "Electroencephalographic Data Analysis With Visibility Graph Technique for Quantitative Assessment of Brain Dysfunction". In: *Clin. EEG Neurosci.* 46.3, pp. 218–223. ISSN: 1550-0594. DOI: 10.1177/1550059414526186. eprint: 24781371.

Bialy, Liza et al. (2018). "Pediatric emergency research Canada: origins and evolution". In: *Pediatric emergency care* 34.2, pp. 138–144.

Bittencourt-Villalpando, M et al. (2021). “Disentangling the effects of age and mild traumatic brain injury on brain network connectivity: A resting state fMRI study”. In: *Neuroimage: clinical* 29, p. 102534.

Blennow, Kaj et al. (2016). “Traumatic brain injuries”. In: *Nature reviews Disease primers* 2, p. 16084.

Bonilha, Leonardo et al. (2015). “Reproducibility of the structural brain connectome derived from diffusion tensor imaging”. In: *PloS one* 10.9, e0135247.

Bordier, Cécile, Carlo Nicolini, and Angelo Bifone (2017). “Graph Analysis and Modularity of Brain Functional Connectivity Networks: Searching for the Optimal Threshold”. In: *Frontiers in Neuroscience* 11. [Online; accessed 2022-06-30].

Borgatti, Stephen P and Martin G Everett (2000). “Models of core/periphery structures”. In: *Social networks* 21.4, pp. 375–395.

Botchway, Edith et al. (2022). “Resting-State Network Organisation in Children with Traumatic Brain Injury”. In: *Cortex*.

Botvinik-Nezer, Rotem et al. (June 2020). “Variability in the analysis of a single neuroimaging dataset by many teams”. In: *Nature* 582.7810, pp. 84–88. ISSN: 1476-4687. DOI: 10.1038/s41586-020-2314-9.

Bowman, F DuBois (2014). “Brain imaging analysis”. In: *Annual review of statistics and its application* 1, pp. 61–85.

Bressler, Steven L (1995). “Large-scale cortical networks and cognition”. In: *Brain Research Reviews* 20.3, pp. 288–304.

Brooks, Brian L. et al. (Mar. 2014). “Perception of Recovery After Pediatric Mild Traumatic Brain Injury Is Influenced by the “Good Old Days” Bias: Tangible Implications for Clinical Practice and Outcomes Research”. In: *Arch. Clin. Neuropsychol.* 29.2, pp. 186–193. ISSN: 0887-6177. DOI: 10.1093/arclin/act083.

Bullmore, Ed and Olaf Sporns (2012). “The economy of brain network organization”. In: *Nature Reviews Neuroscience* 13.5, p. 336.

Bullmore, Edward T and Danielle S Bassett (2011). “Brain graphs: graphical models of the human brain connectome”. In: *Annual review of clinical psychology* 7, pp. 113–140.

Bullmore and Olaf Sporns (2009). “Complex brain networks: graph theoretical analysis of structural and functional systems”. In: *Nature reviews neuroscience* 10.3, pp. 186–198.

Buracas, Giedrius T., Ione Fine, and Geoffrey M. Boynton (Mar. 2005). “The Relationship between Task Performance and Functional Magnetic Resonance Imaging Response”. In: *J. Neurosci.* 25.12, p. 3023. DOI: 10.1523/JNEUROSCI.4476-04.2005.

Button, Katherine S et al. (2013). "Power failure: why small sample size undermines the reliability of neuroscience". In: *Nature reviews neuroscience* 14.5, pp. 365–376.

Caeyenberghs, Karen et al. (2017). "Mapping the functional connectome in traumatic brain injury: What can graph metrics tell us?" In: *Neuroimage* 160, pp. 113–123.

Cai, Qing, Jianpeng An, and Zhongke Gao (Dec. 2020). "A multiplex visibility graph motif-based convolutional neural network for characterizing sleep stages using EEG signals". In: *Brain Sci. Adv.* 6.4, pp. 355–363. ISSN: 2096-5958. DOI: 10.26599/BSA.2020.9050016.

Carrig, Madeline M, Gregory G Kolden, and Timothy J Strauman (2009). "Using functional magnetic resonance imaging in psychotherapy research: A brief introduction to concepts, methods, and task selection". In: *Psychotherapy Research* 19.4-5, pp. 409–417.

Cassidy, J David et al. (2004). "Incidence, risk factors and prevention of mild traumatic brain injury: results of the WHO Collaborating Centre Task Force on Mild Traumatic Brain Injury". In: *Journal of rehabilitation medicine* 36.0, pp. 28–60.

Centers for Disease Control and Prevention [CDC] (2015). "Report to congress on traumatic brain injury in the United States: epidemiology and rehabilitation". In: *National Center for Injury Prevention and Control* 2, pp. 1–72.

Chang, Nadine et al. (2019). "BOLD5000, a public fMRI dataset while viewing 5000 visual images". In: *Scientific data* 6.1, pp. 1–18.

Chen, Gang et al. (2015). "Detecting the subtle shape differences in hemodynamic responses at the group level". In: *Frontiers in Neuroscience* 9, p. 375.

Chen, Zhang et al. (2013). "Graph theoretical analysis of developmental patterns of the white matter network". In: *Frontiers in human neuroscience* 7, p. 716.

Churchill, N. W. et al. (Mar. 2021). "Long-term changes in the small-world organization of brain networks after concussion". In: *Sci. Rep.* 11.6862, pp. 1–14. ISSN: 2045-2322. DOI: 10.1038/s41598-021-85811-4.

Cignetti, Fabien et al. (2016). "Pros and cons of using the informed basis set to account for hemodynamic response variability with developmental data". In: *Frontiers in neuroscience* 10, p. 322.

Ciric, Rastko et al. (July 1, 2017a). "Benchmarking of Participant-Level Confound Regression Strategies for the Control of Motion Artifact in Studies of Functional Connectivity". In: *NeuroImage* 154, pp. 174–187. ISSN: 1053-8119. DOI: 10.1016/j.neuroimage.2017.03.020.

— (July 2017b). “Benchmarking of participant-level confound regression strategies for the control of motion artifact in studies of functional connectivity”. In: *NeuroImage*. Cleaning up the fMRI time series: Mitigating noise with advanced acquisition and correction strategies 154. [Online; accessed 2022-05-29], pp. 174–187.

Cox, Robert W. and James S. Hyde (1997). “Software Tools for Analysis and Visualization of fMRI Data”. In: *NMR in Biomedicine* 10.4-5, pp. 171–178. ISSN: 1099-1492. DOI: 10.1002/(SICI)1099-1492(199706/08)10:4/5<171::AID-NBM453>3.0.CO;2-L. URL: https://onlinelibrary.wiley.com/doi/abs/10.1002/%28SICI%291099-1492%28199706/08%2910%3A4/5%3C171%3A%3AAID-NBM453%3E3.0.CO%3B2-L (visited on 05/29/2022).

Csermely, Peter et al. (2013). “Structure and dynamics of core/periphery networks”. In: *Journal of Complex Networks* 1.2, pp. 93–123.

Dale, Anders M (1999). “Optimal experimental design for event-related fMRI”. In: *Human brain mapping* 8.2-3, pp. 109–114.

Dennis, Emily L et al. (2017). “Diverging volumetric trajectories following pediatric traumatic brain injury”. In: *Neuroimage: clinical* 15, pp. 125–135.

Derderian, Kimberly D., Xiaojue Zhou, and Lang Chen (Oct. 2021). “Category-specific activations depend on imaging mode, task demand, and stimuli modality: An ALE meta-analysis”. In: *Neuropsychologia* 161, p. 108002. ISSN: 0028-3932. DOI: 10.1016/j.neuropsychologia.2021.108002.

Diamond, Adele (2013). “Executive Functions”. In: *Annu. Rev. Psychol.* 64, p. 135. DOI: 10.1146/annurev-psych-113011-143750.

Diedenhofen, Birk and Jochen Musch (2015). “cocor: A comprehensive solution for the statistical comparison of correlations”. In: *PloS one* 10.4, e0121945.

Drobyshevsky, Alexander, Stephen B. Baumann, and Walter Schneider (June 2006). “A rapid fMRI task battery for mapping of visual, motor, cognitive, and emotional function”. In: *Neuroimage* 31.2, pp. 732–744. ISSN: 1053-8119. DOI: 10.1016/j.neuroimage.2005.12.016.

Duann, Jeng-Ren et al. (2002). “Single-trial variability in event-related BOLD signals”. In: *Neuroimage* 15.4, pp. 823–835.

Dziemian, Sabine, Zofia Barańczuk-Turska, and Nicolas Langer (Oct. 2022). “Association between attention-deficit/hyperactivity disorder symptom severity and white matter integrity moderated by in-scanner head motion”. In: *Transl. Psychiatry* 12.434, pp. 1–10. ISSN: 2158-3188. DOI: 10.1038/s41398-022-02117-3.

Elliott, Maxwell L et al. (2020). “What is the test-retest reliability of common task-functional MRI measures? New empirical evidence and a meta-analysis”. In: *Psychological Science* 31.7, pp. 792–806.
Esteban, Oscar et al. (2019). “fMRIPrep: a robust preprocessing pipeline for functional MRI”. In: *Nature methods* 16.1, pp. 111–116.
Fonov, Vladimir S et al. (2009). “Unbiased nonlinear average age-appropriate brain templates from birth to adulthood”. In: *NeuroImage* 47, S102.
Fornito, Alex, Andrew Zalesky, and Edward Bullmore (2016). *Fundamentals of brain network analysis*. Academic Press.
Fortin, Jean-Philippe, Nicholas Cullen, et al. (2018). “Harmonization of cortical thickness measurements across scanners and sites”. In: *Neuroimage* 167, pp. 104–120.
Fortin, Jean-Philippe, Drew Parker, et al. (2017). “Harmonization of multi-site diffusion tensor imaging data”. In: *Neuroimage* 161, pp. 149–170.
Fortin, Jean-Philippe, Elizabeth M Sweeney, et al. (2016). “Removing inter-subject technical variability in magnetic resonance imaging studies”. In: *NeuroImage* 132, pp. 198–212.
Friston, K (2002). “Beyond phrenology: what can neuroimaging tell us about distributed circuitry?” In: *Annual review of neuroscience* 25.1, pp. 221–250.
Friston, Karl et al. (1994). “Statistical parametric maps in functional imaging: a general linear approach”. In: *Human brain mapping* 2.4, pp. 189–210.
Friston, Karl J, P Fletcher, et al. (1998). “Event-related fMRI: characterizing differential responses”. In: *Neuroimage* 7.1, pp. 30–40.
Friston, Karl J, Andrew P Holmes, et al. (1995). “Analysis of fMRI time-series revisited”. In: *Neuroimage* 2.1, pp. 45–53.
Friston, Karl J, Oliver Josephs, et al. (1998). “Nonlinear event-related responses in fMRI”. In: *Magnetic resonance in medicine* 39.1, pp. 41–52.
Gao, Zhongke et al. (Nov. 2022). *Disrupted Time-Dependent and Functional Connectivity Brain Network in Alzheimer’s Disease: A Resting-State fMRI Study Based on Visibility Graph*. [Online; accessed 14. Nov. 2022]. URL: `http://www.eurekaselect.com/article/104460`.
Garrison, Kathleen A. et al. (Sept. 2015). “The (in)stability of functional brain network measures across thresholds”. In: *NeuroImage* 118, pp. 651–661.
Gauthier, Claudine and Audrey P Fan (2019). “BOLD signal physiology: models and applications”. In: *Neuroimage* 187, pp. 116–127.
Glover, Gary H (2011). “Overview of functional magnetic resonance imaging”. In: *Neurosurgery Clinics* 22.2, pp. 133–139.

Gong, Gaolang, Yong He, Luis Concha, Catherine Lebel, Donald W Gross, et al. (2009a). "Mapping anatomical connectivity patterns of human cerebral cortex using in vivo diffusion tensor imaging tractography". In: *Cerebral cortex* 19.3, pp. 524–536.

— (Mar. 2009b). "Mapping Anatomical Connectivity Patterns of Human Cerebral Cortex Using In Vivo Diffusion Tensor Imaging Tractography". In: *Cerebral Cortex (New York, NY)* 19.3, p. 524. DOI: 10.1093/cercor/bhn102.

Grabowski, Patrick et al. (Jan. 2017). "Multimodal impairment-based physical therapy for the treatment of patients with post-concussion syndrome: A retrospective analysis on safety and feasibility". In: *Physical Therapy in Sport* 23, pp. 22–30. ISSN: 1466-853X. DOI: 10.1016/j.ptsp.2016.06.001.

Grady, Cheryl L et al. (2021). "Influence of sample size and analytic approach on stability and interpretation of brain-behavior correlations in task-related fMRI data". In: *Human Brain Mapping* 42.1, pp. 204–219.

Greve, Douglas N and Bruce Fischl (2009). "Accurate and robust brain image alignment using boundary-based registration". In: *Neuroimage* 48.1, pp. 63–72.

Han, Kihwan et al. (2014). "Disrupted modular organization of resting-state cortical functional connectivity in US military personnel following concussive 'mild'blast-related traumatic brain injury". In: *Neuroimage* 84, pp. 76–96.

Handwerker, Daniel A, John M Ollinger, and Mark D'Esposito (2004). "Variation of BOLD hemodynamic responses across subjects and brain regions and their effects on statistical analyses". In: *Neuroimage* 21.4, pp. 1639–1651.

Hasson, Uri et al. (Feb. 2018). "A combinatorial framework to quantify peak/pit asymmetries in complex dynamics". In: *Sci. Rep.* 8.3557, pp. 1–17. ISSN: 2045-2322. DOI: 10.1038/s41598-018-21785-0.

Henson, Rik NA et al. (2002). "Detecting latency differences in event-related BOLD responses: application to words versus nonwords and initial versus repeated face presentations". In: *Neuroimage* 15.1, pp. 83–97.

Hillman, Elizabeth MC (2014). "Coupling mechanism and significance of the BOLD signal: a status report". In: *Annual review of neuroscience* 37, pp. 161–181.

Hittner, James B, Kim May, and N Clayton Silver (2003). "A Monte Carlo evaluation of tests for comparing dependent correlations". In: *The Journal of general psychology* 130.2, pp. 149–168.

Horn, Harm J. van der et al. (Jan. 2017). "Graph Analysis of Functional Brain Networks in Patients with Mild Traumatic Brain Injury". In: *PLoS One* 12.1, e0171031. ISSN: 1932-6203. DOI: 10.1371/journal.pone.0171031.

Hou, Wenshuai et al. (July 2019). "Dynamic Functional Network Analysis in Mild Traumatic Brain Injury". In: *Brain Connect.* 9.6, p. 475. DOI: 10.1089/brain.2018.0629.

Huettel, Scott A (2012). "Event-related fMRI in cognition". In: *Neuroimage* 62.2, pp. 1152–1156.

Imms, Phoebe et al. (2019). "The structural connectome in traumatic brain injury: A meta-analysis of graph metrics". In: *Neuroscience & Biobehavioral Reviews* 99, pp. 128–137.

Iñiguez, Gerardo, Federico Battiston, and Márton Karsai (2020). "Bridging the gap between graphs and networks". In: *Communications Physics* 3.1, pp. 1–5.

Iturria-Medina, Yasser, Erick Jorge Canales-Rodrıéguez, et al. (2007). "Characterizing brain anatomical connections using diffusion weighted MRI and graph theory". In: *Neuroimage* 36.3, pp. 645–660.

Iturria-Medina, Yasser, Roberto C Sotero, et al. (2008). "Studying the human brain anatomical network via diffusion-weighted MRI and Graph Theory". In: *Neuroimage* 40.3, pp. 1064–1076.

Jenkinson, Mark et al. (Oct. 1, 2002). "Improved Optimization for the Robust and Accurate Linear Registration and Motion Correction of Brain Images". In: *NeuroImage* 17.2, pp. 825–841. ISSN: 1053-8119. DOI: 10.1006/nimg.2002.1132. URL: https://www.sciencedirect.com/science/article/pii/S1053811902911328 (visited on 05/29/2022).

Jia, Xiaoyan et al. (Oct. 2021). "A Longitudinal Study of White Matter Functional Network in Mild Traumatic Brain Injury". In: *J. Neurotrauma* 38.19, pp. 2686–2697. ISSN: 1557-9042. DOI: 10.1089/neu.2021.0017. eprint: 33906419.

Johnson, W Evan, Cheng Li, and Ariel Rabinovic (2007). "Adjusting batch effects in microarray expression data using empirical Bayes methods". In: *Biostatistics* 8.1, pp. 118–127.

Kim, Eunkyung et al. (Sept. 2022). "An exploratory study on functional connectivity after mild traumatic brain injury: Preserved global but altered local organization". In: *Brain Behav.* 12.9, e2735. ISSN: 2162-3279. DOI: 10.1002/brb3.2735.

Koenis, Marinka MG et al. (2015). "Development of the brain's structural network efficiency in early adolescence: a longitudinal DTI twin study". In: *Human Brain Mapping* 36.12, pp. 4938–4953.

Koo, Terry K and Mae Y Li (2016). "A guideline of selecting and reporting intraclass correlation coefficients for reliability research". In: *Journal of chiropractic medicine* 15.2, pp. 155–163.

Kurokawa, Ryo et al. (2021). "Cross-scanner reproducibility and harmonization of a diffusion MRI structural brain network: A traveling subject study of multi-b acquisition". In: *NeuroImage*, p. 118675.

Lacasa, Lucas, Bartolo Luque, et al. (2008). "From time series to complex networks: The visibility graph". In: *Proceedings of the National Academy of Sciences* 105.13, pp. 4972–4975.

Lacasa, Lucas, Vincenzo Nicosia, and Vito Latora (2015). "Network structure of multivariate time series". In: *Scientific reports* 5.1, pp. 1–9.

Lanczos, C. (Jan. 1964). "Evaluation of Noisy Data". In: *Journal of the Society for Industrial and Applied Mathematics Series B Numerical Analysis* 1.1, pp. 76–85. ISSN: 0887-459X. DOI: 10.1137/0701007. URL: https://epubs.siam.org/doi/10.1137/0701007 (visited on 05/29/2022).

Lange, Rael T. et al. (Feb. 2015). "Diffusion Tensor Imaging Findings and Postconcussion Symptom Reporting Six Weeks Following Mild Traumatic Brain Injury". In: *Arch. Clin. Neuropsychol.* 30.1, pp. 7–25. ISSN: 0887-6177. DOI: 10.1093/arclin/acu060.

Langlois, Jean A, Wesley Rutland-Brown, and Marlena M Wald (2006). "The epidemiology and impact of traumatic brain injury: a brief overview". In: *The Journal of head trauma rehabilitation* 21.5, pp. 375–378.

Latora, Vito and Massimo Marchiori (2001). "Efficient behavior of small-world networks". In: *Physical review letters* 87.19, p. 198701.

Ledoux, Andrée-Anne et al. (2019). "Natural progression of symptom change and recovery from concussion in a pediatric population". In: *JAMA pediatrics* 173.1, e183820–e183820.

Lee, Jin Hyung et al. (2010). "Global and local fMRI signals driven by neurons defined optogenetically by type and wiring". In: *Nature* 465.7299, pp. 788–792.

Leek, Jeffrey T et al. (2012). "The sva package for removing batch effects and other unwanted variation in high-throughput experiments". In: *Bioinformatics* 28.6, pp. 882–883.

Leemans, AJBSJJDK et al. (2009). "ExploreDTI: a graphical toolbox for processing, analyzing, and visualizing diffusion MR data". In: *Proc Intl Soc Mag Reson Med*. Vol. 17. 1.

Leemans, Alexander and Derek K Jones (2009). "The B-matrix must be rotated when correcting for subject motion in DTI data". In: *Magnetic Resonance in Medicine: An Official Journal of the International Society for Magnetic Resonance in Medicine* 61.6, pp. 1336–1349.

Lerch, Jason P et al. (2017). "Studying neuroanatomy using MRI". In: *Nature neuroscience* 20.3, pp. 314–326.

Li, Muwei et al. (Mar. 2019). "Characterization of the hemodynamic response function in white matter tracts for event-related fMRI". In: *Nat. Commun.* 10.1140, pp. 1–11. ISSN: 2041-1723. DOI: 10.1038/s41467-019-09076-2.

Liao, Chien Heng et al. (2002). "Estimating the delay of the fMRI response". In: *NeuroImage* 16.3, pp. 593–606.

Lim, Sol et al. (2015). "Preferential detachment during human brain development: age-and sex-specific structural connectivity in diffusion tensor imaging (DTI) data". In: *Cerebral Cortex* 25.6, pp. 1477–1489.

Lin, Fa-Hsuan et al. (2018). "Relative latency and temporal variability of hemodynamic responses at the human primary visual cortex". In: *Neuroimage* 164, pp. 194–201.

Lindquist, Martin A et al. (2009). "Modeling the hemodynamic response function in fMRI: efficiency, bias and mis-modeling". In: *Neuroimage* 45.1, S187–S198.

Lindsey, Hannah M et al. (2021). "Diffusion-Weighted Imaging in Mild Traumatic Brain Injury: A Systematic Review of the Literature". In: *Neuropsychology Review*, pp. 1–80.

Liu, Yin et al. (June 2022). "Neuropathological Mechanisms of Mild Traumatic Brain Injury: A Perspective From Multimodal Magnetic Resonance Imaging". In: *Front. Neurosci.* 16. ISSN: 1662-453X. DOI: 10.3389/fnins.2022.923662.

Logothetis, Nikos K and Brian A Wandell (2004). "Interpreting the BOLD signal". In: *Annu. Rev. Physiol.* 66, pp. 735–769.

Long, Christopher J et al. (2005). "Nonstationary noise estimation in functional MRI". In: *NeuroImage* 28.4, pp. 890–903.

Louridas, Panos (2018). "Review of Network Science by Albert-Làaszlò Barabàasi". In: *ACM SIGACT News* 49.2, pp. 10–13.

Maas, Andrew IR et al. (2017a). "Traumatic brain injury: integrated approaches to improve prevention, clinical care, and research". In: *The Lancet Neurology* 16.12, pp. 987–1048.

— (2017b). "Traumatic brain injury: integrated approaches to improve prevention, clinical care, and research". In: *The Lancet Neurology* 16.12, pp. 987–1048.

Madhavan, Radhika et al. (Mar. 2019). "Longitudinal Resting State Functional Connectivity Predicts Clinical Outcome in Mild Traumatic Brain Injury". In: *J. Neurotrauma* 36.5, pp. 650–660. ISSN: 1557-9042. DOI: 10.1089/neu.2018.5739. eprint: 30024343.

Martinez, Briana I and Sarah E Stabenfeldt (2019). "Current trends in biomarker discovery and analysis tools for traumatic brain injury". In: *Journal of biological engineering* 13.1, p. 16.

Mayer, Andrew R, Mayank Kaushal, et al. (2018). "Advanced biomarkers of pediatric mild traumatic brain injury: Progress and perils". In: *Neuroscience & Biobehavioral Reviews* 94, pp. 149–165.

Mayer, Andrew R, David D Stephenson, et al. (2020). "Comparison of methods for classifying persistent post-concussive symptoms in children". In: *Journal of neurotrauma* 37.13, pp. 1504–1511.

McCauley, Stephen R et al. (2012). "Recommendations for the use of common outcome measures in pediatric traumatic brain injury research". In: *Journal of neurotrauma* 29.4, pp. 678–705.

McIntosh, Anthony Randal (2000). "Towards a network theory of cognition". In: *Neural networks* 13.8-9, pp. 861–870.

Menon, David K. et al. (Nov. 2010). "Position Statement: Definition of Traumatic Brain Injury". In: *Arch. Phys. Med. Rehabil.* 91.11, pp. 1637–1640. ISSN: 0003-9993. DOI: 10.1016/j.apmr.2010.05.017.

Messé, Arnaud et al. (2013). "Specific and evolving resting-state network alterations in post-concussion syndrome following mild traumatic brain injury". In: *PloS one* 8.6, e65470.

Mohammadpoory, Zeynab, Mahda Nasrolahzadeh, and Javad Haddadnia (2017). "Epileptic seizure detection in EEGs signals based on the weighted visibility graph entropy". In: *Seizure* 50, pp. 202–208.

Monti, Martin M (2011). "Statistical analysis of fMRI time-series: a critical review of the GLM approach". In: *Frontiers in human neuroscience* 5, p. 28.

Morelli, Nathan et al. (Sept. 2021). "Resting state functional connectivity responses post-mild traumatic brain injury: a systematic review". In: *Brain Inj.* 35.11, pp. 1326–1337. ISSN: 0269-9052. DOI: 10.1080/02699052.2021.1972339.

Mortaheb, Sepehr et al. (Sept. 2021). "Neurophysiological Biomarkers of Persistent Post-concussive Symptoms: A Scoping Review". In: *Front. Neurol.* 12, p. 687197. ISSN: 1664-2295. DOI: 10.3389/fneur.2021.687197. eprint: 34566837.

MTBI, C (2004). "Methodological issues and research recommendations for mild traumatic brain injury: the WHO Collaborating Centre Task Force on Mild Traumatic Brain Injury". In: *J Rehabil Med* 43, pp. 113–25.

Mumford, Jeanette A. and Thomas E. Nichols (Jan. 2008). "Power calculation for group fMRI studies accounting for arbitrary design and temporal autocorrelation". In: *Neuroimage* 39.1, pp. 261–268. ISSN: 1053-8119. DOI: 10.1016/j.neuroimage.2007.07.061.

Newman, M. E. J. (June 2004). "Fast algorithm for detecting community structure in networks". In: *Phys. Rev. E* 69 (6), p. 066133. DOI: 10.1103/PhysRevE.69.066133. URL: https://link.aps.org/doi/10.1103/PhysRevE.69.066133.

Nicolini, Carlo et al. (May 2020). "Scale-resolved analysis of brain functional connectivity networks with spectral entropy". In: *NeuroImage* 211. [Online; accessed 2022-06-30], p. 116603.

Noble, Stephanie, Dustin Scheinost, and R Todd Constable (2020). "Cluster failure or power failure? Evaluating sensitivity in cluster-level inference". In: *Neuroimage* 209, p. 116468.

O'Brien, Heidi et al. (2021). "Normative and psychometric characteristics of the health and behavior inventory among children with mild orthopedic injury presenting to the emergency department: Implications for assessing postconcussive symptoms using the Child Sport Concussion Assessment Tool 5th Edition (Child SCAT5)". In: *Clinical Journal of Sport Medicine* 31.5, e221–e228.

Ogawa, S. et al. (July 1992). "Intrinsic signal changes accompanying sensory stimulation: functional brain mapping with magnetic resonance imaging." In: *Proc. Natl. Acad. Sci. U.S.A.* 89.13, pp. 5951–5955. DOI: 10.1073/pnas.89.13.5951.

Onicas, Adrian I. et al. (2022). "Multisite Harmonization of Structural DTI Networks in Children: An A-CAP Study". In: *Front. Neurol.* 0. ISSN: 1664-2295. DOI: 10.3389/fneur.2022.850642.

Palacios, Eva M. et al. (Apr. 2017). "Resting-State Functional Connectivity Alterations Associated with Six-Month Outcomes in Mild Traumatic Brain Injury". In: *J. Neurotrauma* 34.8, pp. 1546–1557. ISSN: 1557-9042. DOI: 10.1089/neu.2016.4752. eprint: 28085565.

Palla, Gergely et al. (2005). "Uncovering the overlapping community structure of complex networks in nature and society". In: *nature* 435.7043, p. 814.

Pandit, Anand S. et al. (May 2013). "Traumatic brain injury impairs small-world topology". In: *Neurology* 80.20, pp. 1826–1833. ISSN: 1526-632X. DOI: 10.1212/WNL.0b013e3182929f38. eprint: 23596068.

Pedregosa, Fabian et al. (2015). “Data-driven HRF estimation for encoding and decoding models”. In: *NeuroImage* 104, pp. 209–220.
Peixoto, Tiago P and Stefan Bornholdt (2012). “Evolution of robust network topologies: Emergence of central backbones”. In: *Physical review letters* 109.11, p. 118703.
Pernet, Cyril R (2014). “Misconceptions in the use of the General Linear Model applied to functional MRI: a tutorial for junior neuro-imagers”. In: *Frontiers in neuroscience* 8, p. 1.
Pinto, Maıéra Siqueira et al. (2020). “Harmonization of brain diffusion MRI: Concepts and methods”. In: *Frontiers in Neuroscience* 14, p. 396.
Poldrack, Russell A et al. (2017). “Scanning the horizon: towards transparent and reproducible neuroimaging research”. In: *Nature reviews neuroscience* 18.2, pp. 115–126.
Pomponio, Raymond et al. (2020). “Harmonization of large MRI datasets for the analysis of brain imaging patterns throughout the lifespan”. In: *NeuroImage* 208, p. 116450.
Power, Jonathan D., Anish Mitra, et al. (Jan. 2014). “Methods to detect, characterize, and remove motion artifact in resting state fMRI”. In: *Neuroimage* 84, pp. 320–341. ISSN: 1053-8119. DOI: 10.1016/j.neuroimage.2013.08.048.
Power, Jonathan D., Mark Plitt, et al. (Feb. 1, 2017). “Sources and Implications of Whole-Brain fMRI Signals in Humans”. In: *NeuroImage* 146, pp. 609–625. ISSN: 1053-8119. DOI: 10.1016/j.neuroimage.2016.09.038. URL: https://www.sciencedirect.com/science/article/pii/S1053811916305158 (visited on 06/30/2022).
Rombach, M Puck et al. (2014). “Core-periphery structure in networks”. In: *SIAM Journal on Applied mathematics* 74.1, pp. 167–190.
Rosa, Paulo N, Patricia Figueiredo, and Carlos J Silvestre (2015). “On the distinguishability of HRF models in fMRI”. In: *Frontiers in computational neuroscience* 9, p. 54.
Rosen, Bruce R, Randy L Buckner, and Anders M Dale (1998). “Event-related functional MRI: past, present, and future”. In: *Proceedings of the National Academy of Sciences* 95.3, pp. 773–780.
Rubinov, M et al. (2015). “Wiring cost and topological participation of the mouse brain connectome”. In: *Proceedings of the National Academy of Sciences* 112.32, pp. 10032–10037.
Rubinov, Mikail and Olaf Sporns (2010). “Complex network measures of brain connectivity: uses and interpretations”. In: *Neuroimage* 52.3, pp. 1059–1069.

Saarimäki, Heini (2021). "Naturalistic Stimuli in Affective Neuroimaging: A Review". In: *Front. Hum. Neurosci.* 15. DOI: 10.3389/fnhum.2021.675068.

Sannino, Speranza et al. (2017). "Visibility graphs for fMRI data: Multiplex temporal graphs and their modulations across resting-state networks". In: *Network Neuroscience* 1.3, pp. 208–221.

Satterthwaite, Theodore D. et al. (Jan. 1, 2013). "An Improved Framework for Confound Regression and Filtering for Control of Motion Artifact in the Preprocessing of Resting-State Functional Connectivity Data". In: *NeuroImage* 64, pp. 240–256. ISSN: 1095-9572. DOI: 10.1016/j.neuroimage.2012.08.052. pmid: 22926292.

Schmidt, Julia et al. (2018). "Imaging in pediatric concussion: a systematic review". In: *Pediatrics* 141.5.

Setnik, Lon and Jeffrey J Bazarian (2007). "The characteristics of patients who do not seek medical treatment for traumatic brain injury". In: *Brain injury* 21.1, pp. 1–9.

Sharp, David J, Gregory Scott, and Robert Leech (2014). "Network dysfunction after traumatic brain injury". In: *Nature Reviews Neurology* 10.3, pp. 156–166.

Shin, Samuel S et al. (2017). "Structural imaging of mild traumatic brain injury may not be enough: overview of functional and metabolic imaging of mild traumatic brain injury". In: *Brain imaging and behavior* 11.2, pp. 591–610.

Shukla, Ayushi et al. (2021). "Examining brain white matter after pediatric mild traumatic brain injury using neurite orientation dispersion and density imaging: An A-CAP study". In: *NeuroImage: Clinical*, p. 102887.

Shumskaya, Elena et al. (July 2012). "Abnormal whole-brain functional networks in homogeneous acute mild traumatic brain injury". In: *Neurology* 79.2, pp. 175–182. ISSN: 0028-3878. DOI: 10.1212/WNL.0b013e31825f04fb.

Si, Bing et al. (July 2018). "Sub-classifying patients with mild traumatic brain injury: A clustering approach based on baseline clinical characteristics and 90-day and 180-day outcomes". In: *PLoS One* 13.7, e0198741. ISSN: 1932-6203. DOI: 10.1371/journal.pone.0198741. eprint: 29995912.

Silva, Vanessa Freitas et al. (2021). "Time series analysis via network science: Concepts and algorithms". In: *Wiley Interdisciplinary Reviews: Data Mining and Knowledge Discovery* 11.3, e1404.

Smith, Stephen M and Thomas E Nichols (2018). "Statistical challenges in "big data" human neuroimaging". In: *Neuron* 97.2, pp. 263–268.

Smith, Stephen M. et al. (Dec. 2013). "Functional connectomics from resting-state fMRI". In: *Trends in Cognitive Sciences* 17.12, pp. 666–682. ISSN: 1364-6613. DOI: 10.1016/j.tics.2013.09.016.

Song, Allen W et al. (2002). "Enhanced spatial localization of neuronal activation using simultaneous apparent-diffusion-coefficient and blood-oxygenation functional magnetic resonance imaging". In: *Neuroimage* 17.2, pp. 742–750.

Sporns, Olaf, Giulio Tononi, and Rolf Kötter (2005). "The human connectome: a structural description of the human brain". In: *PLoS computational biology* 1.4, e42.

Stam, C.J. (2014). "Modern network science of neurological disorders". In: *Nature Reviews Neuroscience* 15.10, pp. 683–695.

Steffener, Jason et al. (2010). "Investigating hemodynamic response variability at the group level using basis functions". In: *Neuroimage* 49.3, pp. 2113–2122.

Telesford, Qawi K. et al. (2010). "Reproducibility of Graph Metrics in fMRI Networks". In: *Front. Neuroinf.* 4. DOI: 10.3389/fninf.2010.00117.

Thurman, David J (2016). "The epidemiology of traumatic brain injury in children and youths: a review of research since 1990". In: *Journal of child neurology* 31.1, pp. 20–27.

Tsai, Shang-Yueh (Aug. 2018). "Reproducibility of structural brain connectivity and network metrics using probabilistic diffusion tractography". In: *Sci. Rep.* 8.11562, pp. 1–12. ISSN: 2045-2322. DOI: 10.1038/s41598-018-29943-0.

Turner, Benjamin O et al. (2018). "Small sample sizes reduce the replicability of task-based fMRI studies". In: *Communications Biology* 1.1, pp. 1–10.

Tustison, Nicholas J. et al. (June 2010). "N4ITK: Improved N3 Bias Correction". In: *IEEE transactions on medical imaging* 29.6, pp. 1310–1320. ISSN: 0278-0062. DOI: 10.1109/TMI.2010.2046908. pmid: 20378467. URL: https://www.ncbi.nlm.nih.gov/pmc/articles/PMC3071855/ (visited on 05/29/2022).

Tzourio-Mazoyer, Nathalie et al. (2002). "Automated anatomical labeling of activations in SPM using a macroscopic anatomical parcellation of the MNI MRI single-subject brain". In: *Neuroimage* 15.1, pp. 273–289.

Vedaei, Faezeh et al. (2021). "Resting-State Functional MRI Metrics in Patients With Chronic Mild Traumatic Brain Injury and Their Association With Clinical Cognitive Performance". In: *Front. Hum. Neurosci.* 0. ISSN: 1662-5161. DOI: 10.3389/fnhum.2021.768485.

Veraart, Jelle et al. (2013). "Weighted linear least squares estimation of diffusion MRI parameters: strengths, limitations, and pitfalls". In: *Neuroimage* 81, pp. 335–346.

Verhelst, Helena et al. (2018). "Impaired rich club and increased local connectivity in children with traumatic brain injury: Local support for the rich?" In: *Human brain mapping* 39.7, pp. 2800–2811.

Vespignani, Alessandro (2018). *Twenty years of network science*.

Vos, Sjoerd B et al. (2017). "The importance of correcting for signal drift in diffusion MRI". In: *Magnetic resonance in medicine* 77.1, pp. 285–299.

Wang, Jinhui et al. (2015). "GRETNA: a graph theoretical network analysis toolbox for imaging connectomics". In: *Frontiers in human neuroscience* 9, p. 386.

Wang, Lei et al. (2017). "EEG analysis of seizure patterns using visibility graphs for detection of generalized seizures". In: *Journal of neuroscience methods* 290, pp. 85–94.

Ware, Ashley L, Ayushi Shukla, et al. (2020). "Post-acute white matter microstructure predicts post-acute and chronic post-concussive symptom severity following mild traumatic brain injury in children". In: *NeuroImage: Clinical* 25, p. 102106.

Ware, Ashley L, Keith Owen Yeates, et al. (2022). "Longitudinal white matter microstructural changes in pediatric mild traumatic brain injury: An A-CAP study". In: *Human Brain Mapping*.

Ware, A Shukla, et al. (2022). "Participant factors that contribute to magnetic resonance imaging motion artifacts in children with mild traumatic brain injury or orthopedic injury". In: *Brain Imaging and Behavior* 16.3, pp. 991–1002.

Ware, Yeates, et al. (2021). "Structural connectome differences in pediatric mild traumatic brain and orthopedic injury". In: *Human Brain Mapping*.

Watson, Christopher G, Dana DeMaster, and Linda Ewing-Cobbs (2019). "Graph theory analysis of DTI tractography in children with traumatic injury". In: *NeuroImage: Clinical* 21, p. 101673.

Watts, Duncan J and Steven H Strogatz (1998). "Collective dynamics of 'small-world'networks". In: *nature* 393.6684, p. 440.

Whiteneck, Gale G. et al. (Jan. 2016). "Risk of Negative Outcomes After Traumatic Brain Injury: A Statewide Population-Based Survey". In: *J. Head Trauma Rehabil.* 31.1, pp. 43–54. ISSN: 1550-509X. DOI: 10.1097/HTR.0000000000000141. eprint: 25931188.

Wijk, Bernadette C. M. van, Cornelis J. Stam, and Andreas Daffertshofer (Oct. 2010). "Comparing Brain Networks of Different Size and Con-

nectivity Density Using Graph Theory". In: *PLoS ONE* 5.10. Ed. by Olaf Sporns. [Online; accessed 2022-06-30], e13701.
Wilde, Elisabeth A et al. (2019). "Orthopedic injured versus uninjured comparison groups for neuroimaging research in mild traumatic brain injury". In: *Journal of neurotrauma* 36.2, pp. 239–249.
Worsley, Keith J and Karl J Friston (1995). "Analysis of fMRI time-series revisited—again". In: *Neuroimage* 2.3, pp. 173–181.
Yan, Yan et al. (2017). "Correlation between standardized assessment of concussion scores and small-world brain network in mild traumatic brain injury". In: *Journal of Clinical Neuroscience* 44, pp. 114–121.
Yeates, Keith Owen (2010). "Traumatic brain injury." In.
Yeates, Keith Owen et al. (2017). "Advancing concussion assessment in pediatrics (A-CAP): a prospective, concurrent cohort, longitudinal study of mild traumatic brain injury in children: study protocol". In: *BMJ open* 7.7, e017012.
Yeates, Taylor M. et al. (Jan. 2022). "Sex Differences in the Outcomes of Mild Traumatic Brain Injury in Children Presenting to the Emergency Department". In: *J. Neurotrauma* 39.1-2, pp. 93–101. ISSN: 0897-7151. DOI: 10.1089/neu.2020.7470.
Yu, Meichen, Arjan Hillebrand, et al. (2017). "Horizontal visibility graph transfer entropy (HVG-TE): A novel metric to characterize directed connectivity in large-scale brain networks". In: *NeuroImage* 156, pp. 249–264.
Yu, Meichen, Kristin A Linn, et al. (2018). "Statistical harmonization corrects site effects in functional connectivity measurements from multi-site fMRI data". In: *Human brain mapping* 39.11, pp. 4213–4227.
Zavaliangos-Petropulu, Artemis et al. (2019). "Diffusion MRI indices and their relation to cognitive impairment in brain aging: the updated multi-protocol approach in ADNI3". In: *Frontiers in Neuroinformatics* 13, p. 2.
Zemek, Roger, Martin H Osmond, and Nick Barrowman (2013). "Predicting and preventing postconcussive problems in paediatrics (5P) study: protocol for a prospective multicentre clinical prediction rule derivation study in children with concussion". In: *BMJ open* 3.8, e003550.
Zheng, Minzhang et al. (Mar. 2021). "Visibility graph based temporal community detection with applications in biological time series". In: *Sci. Rep.* 11.5623, pp. 1–12. ISSN: 2045-2322. DOI: 10.1038/s41598-021-84838-x.

Zhou, Yongxia (Aug. 2017). "Small world properties changes in mild traumatic brain injury". In: *J. Magn. Reson. Imaging* 46.2, pp. 518–527. ISSN: 1522-2586. DOI: 10.1002/jmri.25548. eprint: 27902865.

Zhou, Yongxia and Yvonne W Lui (2013). *Changes in brain organization after TBI: evidence from functional MRI findings*.

Zhu, Alyssa H et al. (2019). "Challenges and opportunities in dMRI data harmonization". In: *International Conference on Medical Image Computing and Computer-Assisted Intervention*. Springer, pp. 157–172.

Zhu, Guohun, Yan Li, and Peng Paul Wen (2014). "Analysis and classification of sleep stages based on difference visibility graphs from a single-channel EEG signal". In: *IEEE journal of biomedical and health informatics* 18.6, pp. 1813–1821.

Zhu, Tong et al. (2011). "Quantification of accuracy and precision of multi-center DTI measurements: a diffusion phantom and human brain study". In: *Neuroimage* 56.3, pp. 1398–1411.

Zou, Yong et al. (2019). "Complex network approaches to nonlinear time series analysis". In: *Physics Reports* 787, pp. 1–97.